OCS Study
MMS 2003-074

Modeling and Data Analyses of Circulation Processes in the Gulf of Mexico

Final Report

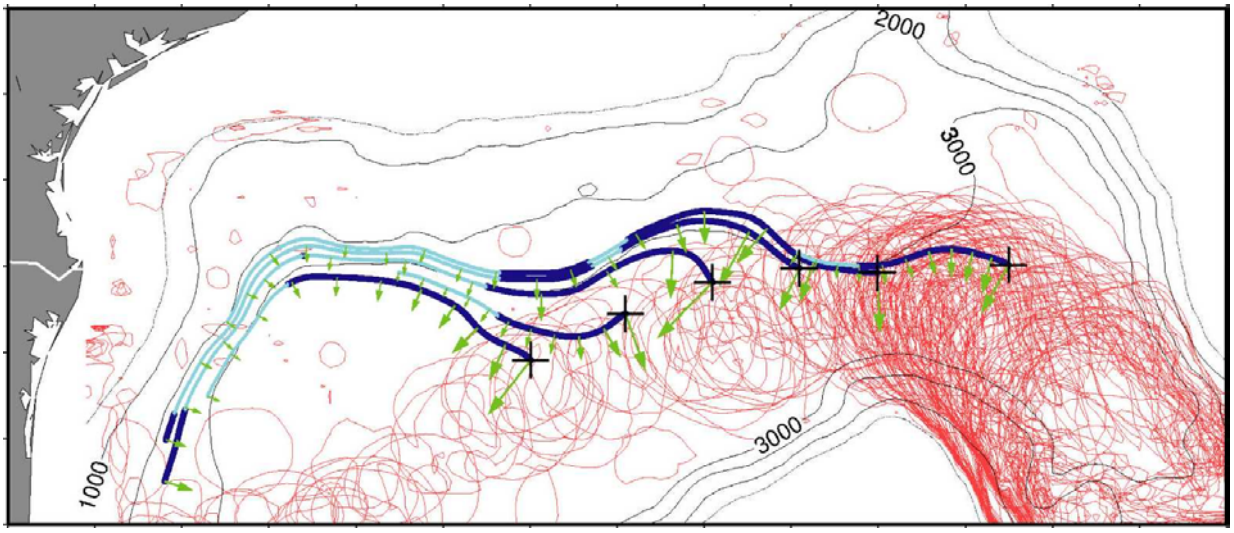

MMS U.S. Department of the Interior
Minerals Management Service
Gulf of Mexico OCS Region

OCS Study
MMS 2003-074

Modeling and Data Analyses of Circulation Processes in the Gulf of Mexico

Final Report

Authors

L.-Y. Oey
Princeton University

P. Hamilton
Science Applications International Corporation

H.-C. Lee
Princeton University

Prepared under MMS Contract
1435-01-99-CT-31028
by
Science Applications International Corporation
615 Oberlin Rd., Suite 100
Raleigh, North Carolina 27605

Published by

U.S. Department of the Interior
Minerals Management Service
Gulf of Mexico OCS Region

New Orleans
February 2004

DISCLAIMER

This report was prepared under contract between the Minerals Management Service (MMS) and Science Applications International Corporation. This report has been technically reviewed by the MMS, and it has been approved for publication. Approval does not signify that the contents necessarily reflect the views and policies of the MMS, nor does mention of trade names or commercial products constitute endorsement or recommendation for use. It is, however, exempt from review and compliance with the MMS editorial standards.

REPORT AVAILABILITY

Extra copies of the report may be obtained from the Public Information Office (Mail Stop 5034) at the following address:

U.S. Department of the Interior
Minerals Management Service
Gulf of Mexico OCS Region
Public Information Office (MS 5034)
1201 Elmwood Park Boulevard
New Orleans, Louisiana 70123-2394

Telephone Number: 1-800-200-GULF or
504-736-2519

CITATION

Suggested citation:

Oey, L.-Y., P. Hamilton, and H.-C. Lee. 2004. Modeling and data analyses of circulation processes in the Gulf of Mexico: Final report. U.S. Dept. of the Interior, Minerals Management Service, Gulf of Mexico OCS Region, New Orleans, LA. OCS Study MMS 2003-074. 140 pp.

ABOUT THE COVER

Wave rays (in blue; light blue for wavelength < 30 cm) traced using the topographic Rossby wave dispersion relation showing the deep energy paths in the northern Gulf of Mexico for waves originating under the Loop Current (LC) and Loop Current eddies (LCE). The 10-year assemblage of the outer boundary of the LC and LCE are shown by the thinner red lines.

TABLE OF CONTENTS

LIST OF FIGURES

LIST OF FIGURES (continued)

LIST OF FIGURES (continued)

LIST OF FIGURES (continued)

LIST OF FIGURES (continued)

LIST OF TABLES

ABSTRACT

The objective of this study is to describe and understand circulation processes in the Gulf of Mexico through modeling and data analysis. The main focus is on two topics, topographic Rossby waves (TRW's) and slope eddies, which are contained in Chapters 3 and 4 of this report. Another section (Chapter 5) reports briefly on other research funded in part by this contract through cooperation with other MMS studies. This study has resulted in four published papers: Oey and Lee (2002); Oey et al. (2003a); Ezer et al. (2003); Wang et al. (2003); and two manuscripts: Oey and Zhang (2003) and Fan et al. (2003).

The TRW work extends Hamilton (1990) and Oey (1996). Based on the results of a high-resolution model, the analysis concentrates more precisely on regions in the Gulf where TRW's are likely to occur, their possible generation site(s) and mechanism(s), and also propagation paths. It is found that TRW's in the 20~100 day periods are excited by small-scale peripheral eddies or meanders around the LC or propagating Loop Current Eddies (LCE's). The TRW's propagate westward and the energy is predominantly confined seaward of the 3,000-m isobath in the central and western Gulf. It is also concluded that the deep Gulf circulation is cyclonic, and that the deep (horizontal) shear in part accounts (together with sloping topography) for the seaward confinement of the TRW rays. These findings are contained in Oey and Lee (2002).

The slope-eddy study focuses on the following scientific problem. Given an observed slope eddy field (spatial scales ≈ 50~150 km) over the north-central Gulf, can a model generate its temporal and spatial evolution, hence deduce its properties (e.g. eddy energy, stability etc), and check the 'prediction' against observations? Two surveys are taken from LATEX-C and GulfCet-I measurements (Hamilton et al., 2002) for the observed eddy fields: (A) Dec/03-14/1993 and (B) Dec/16-23/1993. Data from Period A is used to initialize the model, while that from Period-B is used to check model's prediction. To initialize the model, the larger-scale circulations of LC and LCE's are generated by assimilating satellite altimeter and SST data using an optimal interpolation scheme over the whole model domain. The observed temperature and salinity measurements from Period A are 'injected' by nudging them into the heat/salt equations. The model 'predicts' growth of the eddy energy of this initial field. The growth agrees with the observed increase of the kinetic energy of the geostrophic flow from Period-A to Period-B. Stability analysis indicates that the growth is caused by mixed barotropic and baroclinic instabilities. The success of this use of hydrographic surveys in a model assimilation scheme is a first step along the path that will allow the incorporation of in-situ, ocean observing systems into real-time model predictions.

One of the cooperative studies compares modeled and observed surface currents in the Desoto Canyon for the period April 1997 through April 1999. The model used here is an earlier version, with coarser grid spacing, than was used for the TRW and eddy work. The model shows good agreements with observations in terms of the means and variance ellipses. An SVD (Single Value Decomposition) analysis shows that the model can capture the more dominant mode 1 observations, but misses the mode 2. The latter failure is most likely due to the coarse resolution used in this early model, which may not simulate well the small-scale cyclone-anticyclone pair that exists in mode 2. This study is summarized in Wang et al. (2003).

A drifter comparison study examines the possibility of assimilating observed drifters into the model. The 1998 NEGOM drifters were used to test the scheme. It is shown that a combination of both satellite data and drifter assimilations yields the least RMS errors in drifter positions. The two assimilations are complementary: satellite gives Gulf-wide coverage of large-scale LC and LCE's, while drifters enable more realistic simulations of localized (small-scale) eddy field. By comparing the modeled and in-situ currents over the west Florida shelf, it is also shown that the anomalously intense southward shelf currents in the summer of 1998 were driven by LC forcing as the latter 'brushed' against the shelfbreak in the Florida Straits. This study is reported in a manuscript by Fan et al. (2003).

One of the most outstanding problems in Gulf circulation studies is the cause of the observation that the LC sheds eddies at irregular intervals from 3~17 months. It is shown that wind-induced transport fluctuations through the Greater Antilles passages can cause shedding at shorter intervals (≈ 3~7 months). Anticyclonic Caribbean eddies cause shedding at longer periods (≈ 14~16 months) through potential vorticity conservation, which indicates that Caribbean eddies tend to deter northward extension of the LC into the Gulf. This leads to longer periods between eddy shedding. Fluctuating inflow at the Yucatan Channel that is associated with winds and/or Caribbean eddies can cause a LC eddy to temporarily (~ 1 month) detach from, and then reattach back to the LC, a phenomenon often observed. Model results also suggest that southwest of Hispaniola, warm eddies are spun up by the local wind stress curl. This type of eddy drifts southwestward, then westward after merging with the Caribbean Current, and then northward as it progresses towards the Yucatan Channel. These eddies significantly affect the shedding behavior of warm-core rings. The time scale for spin-up and drift from Hispaniola is about 100 days. Satellite data indicate the existence of these eddies in the real ocean. These findings are reported in Oey et al. (2003a).

1. Introduction

The circulation of the Gulf of Mexico is dominated by processes related to the periodic extension of the Loop Current (LC) and the shedding of large (~300 to 400 km diameter) anticyclonic eddies. These warm LC eddies translate westward or southwestward, at speeds of ~3 to 6 km day^{-1}, across the deep water of the central and western Gulf until they collide with the western Mexican slope. During this passage across the Gulf, LC eddies may generate subsidiary cyclones or frontal eddies, and interact with existing cyclones and anticyclones. On the western Mexican slope, LC eddies undergo complex interactions with topography and the existing eddy field. Dissipation of LC eddies in the west is a very complex process that may involve the generation of smaller scale cyclones and anticyclones. A consequence of the complexity of eddy generation processes is that observations of upper-layer circulation show complex fields of both warm and cold eddies of varying scales ranging from ~ 40 to 50 km up to LC eddy diameters over most regions of the deep Gulf, including the northern and western continental slopes.

Observations of vertical current and density structures have shown that the deep waters of the Gulf are essentially a two layer system with the upper layer dominated by the LC and eddies of varying scales. Below the transition at about 800 to 1,200 m, limited current measurements have shown the flows to be almost depth independent with some bottom intensification. Current fluctuations have periods of between ~10 and 100 days and are usually decoupled from the upper-layer eddy flows. These types of lower-layer fluctuations have been characterized as topographic Rossby waves (TRW) with wavelengths of ~ 100 to 200 km and propagations speeds of ~ 10 to 20 km day^{-1}. It has been speculated, in analogy with studies of the deep Gulf Stream region of the Northwest Atlantic, that the LC fluctuations, and eddy interactions with other eddies and topography are responsible for deep TRW currents. Model studies have also shown lower-layer eddy-like flows that are associated with the translation of a large LC eddy across the Gulf. At the present time, the limited observational database in deep water has not confirmed the existence of these lower-layer eddy flows.

Over the last two decades, the Gulf of Mexico has been one of the principal laboratories for the development of meso-scale, ocean circulation, hydrodynamic models. Studies began with the LC eddy shedding problem, using two-layer models, and have progressed to investigations of boundary conditions affecting the LC, including interaction of the Gulf of Mexico with the Caribbean Sea and the wider western Atlantic, and the assimilation of observations (principally satellite altimetry maps of sea-surface height (SSH) anomalies, and sea-surface temperatures (SST)) to model eddy fields that correspond with the real world. Modern ocean models use three-dimensional high-resolution grids in both the horizontal and vertical. Because of the complexity of circulations in the Gulf of Mexico, numerical models are essential tools for the understanding of the dynamics of the, necessarily limited, observed flows. One of the aims of this study is to examine specific processes, known to be important for energetic sub-surface currents, through analysis of model simulations and observed data, so that an understanding of model dynamics is achieved. This in turn will be a basis for improving the ability of models to simulate Gulf of Mexico circulation processes, which will lead to more accurate hindcasts and forecasts that are important for industry and public uses of this sea.

1.1 Background

When this study was initiated, 3-D numerical models had been applied successfully to the Gulf. Open boundaries were placed at a variety of positions (e.g. the Yucatan, the mid-Atlantic ridge, etc.) and a variety of forcing mechanisms were applied at the sea-surface and open boundaries. These modeling studies all reproduced the basic LC extension and eddy-shedding cycle. Observational studies had shown that the upper-layer over the northern slope and in the deep basin contained a rich field of eddies, with a range of scales and including cyclones as well as anticyclones, not just the dominant LC rings. The higher resolution models also showed eddies at varying scales, but little attempt was made to compare simulations of the eddy fields with the limited findings of the observational studies. It was realized that in order to make quantitative comparisons with observations, models would need to assimilate observational data. A model with forcing applied at the boundaries could only be expected to attempt to reproduce the statistics of eddies because of the stochastic nature of the flows. Assimilation schemes primarily used satellite observations of SSH anomaly and SST because these data types were readily available on regular schedules. SSH is a dynamic quantity and studies had shown that mapping methods could be used to resolve mesoscale circulations in the upper layer at spatial and time scales of about 100 km and 10 days, respectively. SSH is used to infer density anomalies deeper in the water column and thus, constrain the models' subsurface flow fields. Therefore, advances in modeling Gulf of Mexico eddy fields were expected to come from assimilation schemes for various data types and more detailed comparisons with observations. The latter investigations would be expected to show whether the dynamics of the models were reasonable, and whether the scales and eddy interactions were realistic or not. Model improvements would be expected to follow. In turn, the model could provide information on the genesis, evolution and decay of the eddy fields that is not readily available from experimental studies.

Below 1,000 m in water depths greater than ~ 2,000 m, observations have shown the flows to be dominated by propagating planetary waves (TRW's) that have quite different characteristics to the upper-layer eddies. These TRW's are quite energetic with amplitudes greater than 10 cm/s, periods between ~ 7 and 50 days, and wavelengths of ~ 100 km. They have been observed in all regions of the deep Gulf where current measurements have been made. It is important that models are able to simulate these deep currents and thus, the generation and propagation of these waves. Again, if the models were able to reproduce the general characteristics of observed TRW's, the simulations would be expected to provide information on the dynamics of the transfer of energy from upper-layer eddies to the lower-layer. With the exception of Oey (1996), the ability of Gulf models to generate and propagate deep TRW's has not been investigated. Below 1,000 m, assimilation of direct observations is not practicable at present, and SSH has little influence. Since TRW currents at any given position will have propagated from remote source regions, the future ability models to hindcast such events will depend crucially on simulating the processes responsible for generation of the wave trains. It is expected that this will also depend on correctly simulating the dynamics of the upper-layer eddy field and the mechanisms of energy transfer to the lower layer.

1.2 Objectives

Based on the above discussion, the basic objectives of this study are to improve the ability of numerical models to simulate the dynamics of the Gulf by investigating two important phenomena. They are the generation and propagation of TRW's in the deep basin, and evolution of eddy fields through the alteration of vorticity through eddy frontal instabilities, eddy-eddy, and eddy-topography interactions. These processes are investigated by a combination of modeling and high-level analyses of both data and model output. Process-oriented modeling uses increasingly realistic simulations of the Gulf, along with model experiments, to evaluate the dynamics of TRW's and eddies. The model processes are investigated relative to the dynamics revealed by the data analyses.

1.3 Outline of the Report

Chapter 2 contains descriptions of the models used for this study, and specific analysis tools used for the model and observational data. The observational database is also given. Chapters 3 and 4 concentrate on the analysis and simulation of topographic Rossby waves and slope eddies, respectively. Since this study was one of four modeling investigations, funded by the Minerals Management Service (MMS), there was a good-deal of interaction between this and other projects. Chapter 5 briefly summarizes contributions of this study to other projects that involved model-data comparisons and analysis of circulation processes. Finally, Chapter 6 summarizes the report and makes recommendations on future strategies for advancing modeling of the Gulf of Mexico.

2. Methods

2.1 Basic Model Description

Past experiences (Oey, 1996) indicate that, in order to unambiguously study the Gulf's circulation, it is necessary to allow a free dynamical interaction between the Gulf of Mexico and the Caribbean Sea. Oey's (1996) model of the Gulf, for example, includes the northwestern portion of the Caribbean Sea. In the present work, Oey's model domain is further enlarged to include a portion of the North Atlantic Ocean west of 55^{o}W and from 6 to 50^{o}N, shown in Figure 2.1-1. In some calculations, a nest is placed over the Gulf of Mexico to effect double resolution. The model is based on the primitive-equation Princeton Ocean Model as described in more detail in Oey and Lee (2002). Time-independent total transports are specified at 55^{o}W according to Schmitz (1996). Except in experiments in which we assimilate sea-surface height anomaly from the satellite, the steady transports effectively filter out propagating signals from the region east of 55^{o}W. These transports determine the two-dimensional depth-integrated velocities at the open boundary and are meant to account for the large-scale transports, caused by the wind-stress curl and thermohaline forcing, through 55^{o}W. The open-boundary conditions are a combination of these transport specifications along with radiation and advection as detailed in Oey and Chen (1992). For example, the temperature and salinity fields are advected using a one-sided difference scheme when flows are eastward (that is, outflow), and are prescribed from either the annual or monthly-mean temperatures and salinities from the Generalized Digital Environmental Model (GDEM) climatology (Teague et al., 1990) when flows are westward. These open-boundary specifications also set the baroclinic structure, which in the present case is largely geostrophic through the thermal-wind balance. All fluxes are zero across closed boundaries. At the sea-surface, climatological heat and salt fluxes are specified, and momentum flux (wind-stress) is specified from the six-hourly ECMWF data.

The variable model grid spacing ranges from $\Delta \approx 10$ km in the northwestern Caribbean/Yucatan Channel, to $\Delta \approx 5$ km in the eastern and northern Gulf of Mexico. There are 25 vertical sigma levels with finer resolution over the upper and lower 500-1,000 m of the water column (Oey and Lee, 2002). For all experiments, the Smagorinsky's (1963) mixing coefficient is set to 0.1, and the ratio of (horizontal) diffusivity to viscosity is 0.1.

The sigma-level pressure gradient error (Haney, 1991) in the model is not large when compared with the physically meaningful modeled currents. The error is reduced by removing the basin-averaged density profile (i.e. $<\rho>$ is a function of z only) from the time-dependent density field before evaluating the pressure gradient terms (Mellor et al. 1998). A one-year test calculation using an initially level density field with perturbations (see Mellor et al., 1998) and zero forcing was conducted. Figure 2.1-2 shows that the maximum error asymptotes to ≈ 0.15 cm/s, which is relatively small in comparison to, say, the Loop Current speeds ≈ 1 m/s. Moreover, this maximum occurs off Cape Hatteras, under the Gulf Stream, and thus removed from the region of particular interest to this study.

The model has been described in a number of publications: Oey and Lee (2002), Oey et al. (2003a), Wang et al. (2003) and Ezer et al. (2003). Oey et al. (2003b) in particular address the sigma-level pressure gradient error, satellite data and assimilation scheme, and also model

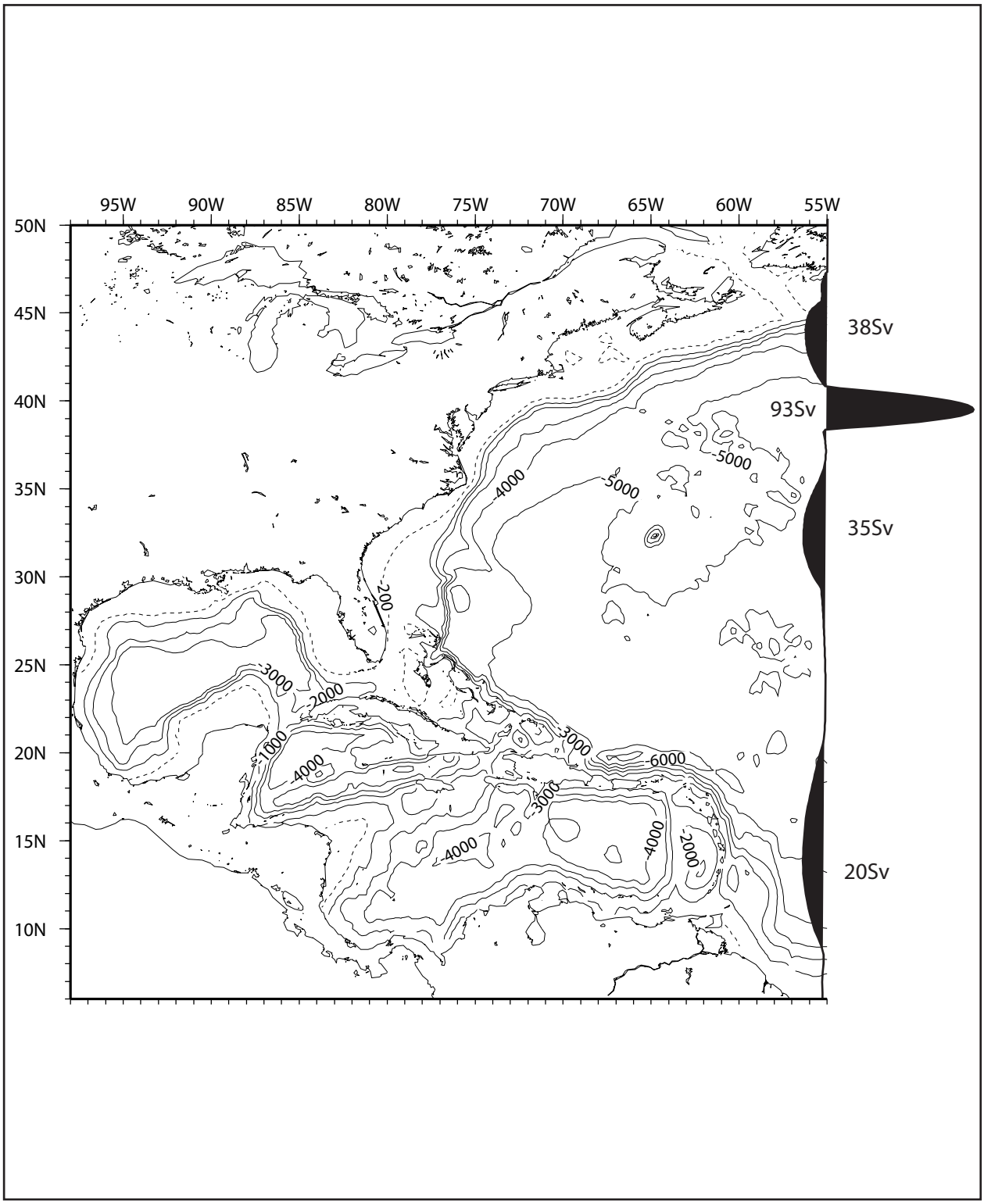

Figure 2.1-1a The model orthogonal curvilinear grids encompass the Gulf of Mexico, the Caribbean Sea, and a portion of the Atlantic Ocean. Time-independant inflow and outflow that account for the large scale transports (Sverdrup + themohaline) are specified across the open boundary at 55 W as a function of latitude.

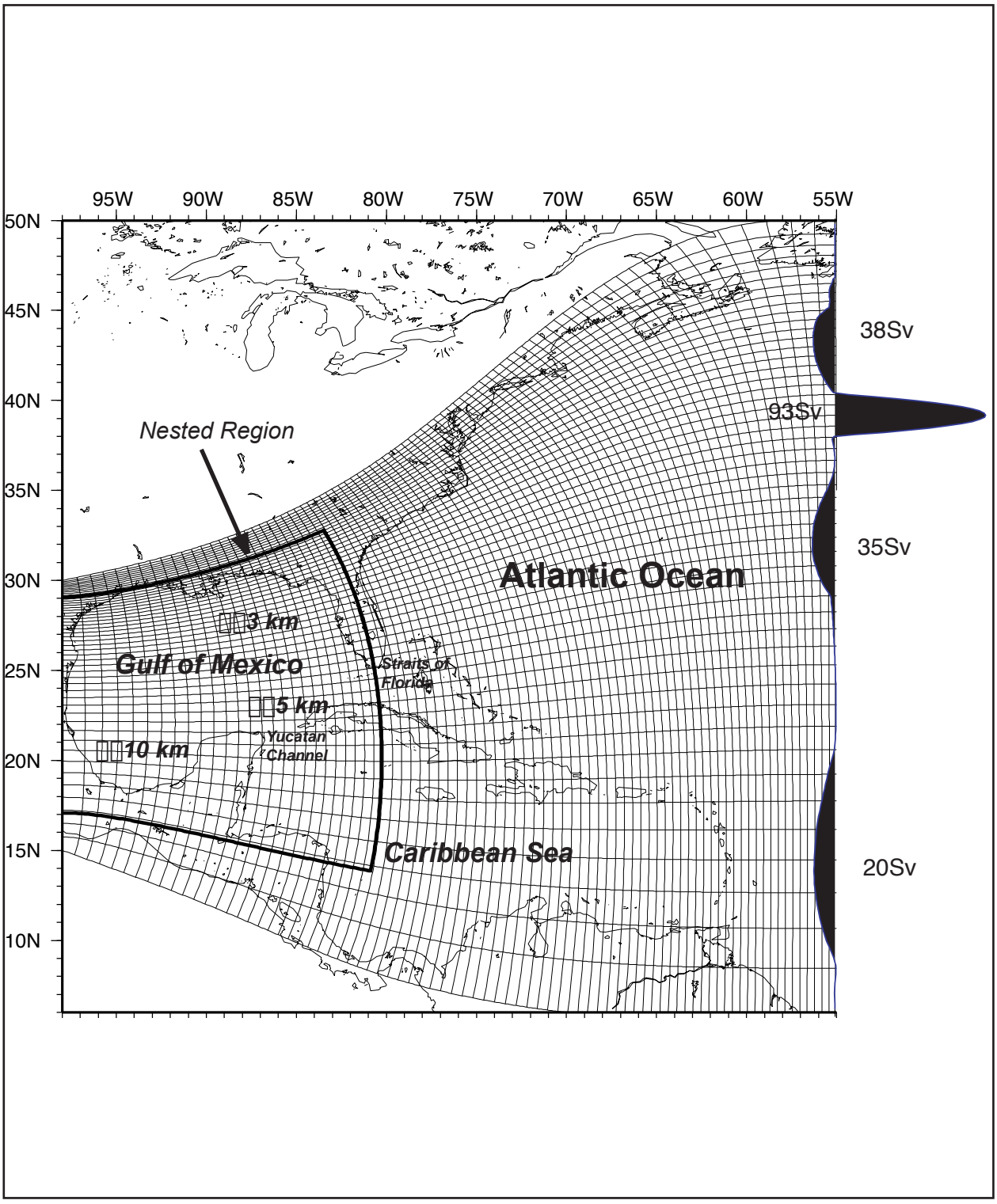

Figure 2.1-1b Oey and Lee's (2002) northwest Atlantic Ocean model domain and the nested doubled-resolution Gulf of Mexico region where calculations described in this report are conducted. The "parent" grid lines are shown at every seventh grid point, and the approximate distribution of doubled resolution grid sizes is indicated

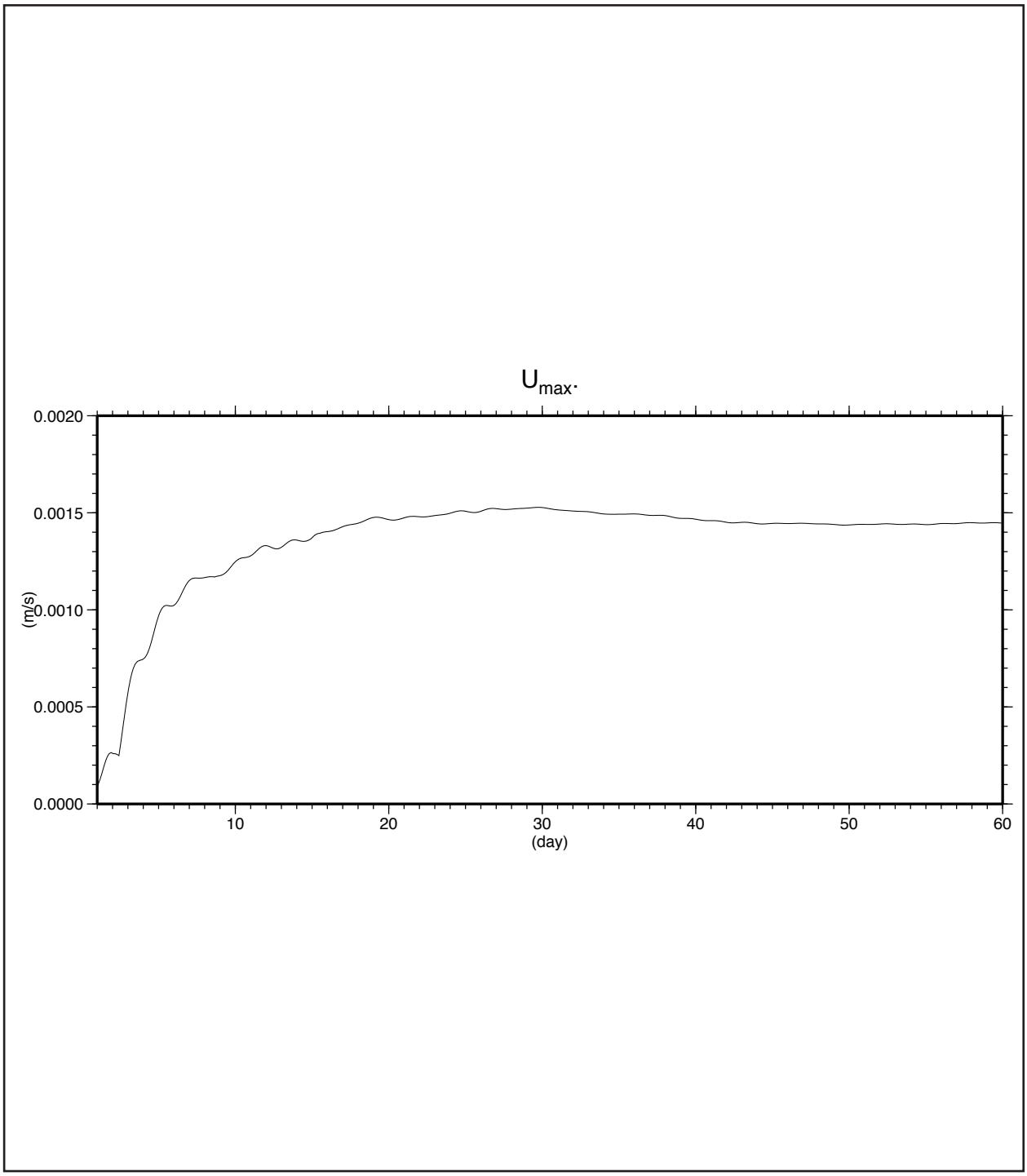

Figure 2.1-2. The maximum speed that results from a one-year test calculation using initially level density field with perturbation: $\rho(z) = \rho_r + \rho'$, where ρ_r = area-averaged and annual-mean climatological density, and $\rho' = -0.1$ kg/m^3 • exp (z/1000 m) and zero forcing (see Mellor et al., 1998). For this perturbation, the maximum speed asymptotes to 1.45×10^{-3} m s^{-1} in about 60 days. Only the first 60 days is shown in the plot. The error is approximately proportional to the amplitude of perturbation.

sensitivity to grid resolution. Satellite data assimilation is the basic method for hindcasting Gulf of Mexico circulations and is discussed below. Assimilation of hydrography is discussed in Chapter 4.

2.1.1 Satellite Data Assimilation

The satellite data are assimilated into the model following the methodology given in Mellor and Ezer (1990). The model is integrated without assimilation for 8 years, forced by 6-hourly European Centre for Medium-Range Weather Forecast (ECMWF) winds, and surface heat and salt fluxes. The correlations between SSH anomaly $\delta\eta$ and subsurface temperature and salinity (T/S) are calculated from the model results. Given the satellite SSH anomaly, $\delta\eta_{sa}$, the model subsurface temperature anomaly δT is calculated as:

$$\delta T(x,y,z,t) = F_T(x,y,z)\, \delta\eta_{sa}(x,y,t) \qquad (2.1\text{-}1)$$

where the correlation factor is

$$F_T = <\delta T\, \delta\eta>/<\delta\eta^2>, \qquad (2.1\text{-}2a)$$

and the corresponding correlation coefficient is

$$C_T = <\delta T\, \delta\eta>/[<\delta T^2><\delta\eta^2>]^{1/2}. \qquad (2.1\text{-}2b)$$

After each assimilation time step Δt_A (= 1 day), the model temperature T is replaced by the assimilated temperature T_A:

$$T_A = T + [2\, R_A C_T^2/(1 + 2\, R_A C_T^2 - C_T^2)]\, (T_O - T) \qquad (2.1\text{-}3)$$

where R_A is the ratio of Δt_A to the de-correlation time scale Δt_E of the model eddy field ($\approx$ 30 days), and T_O is the 'observed' temperature inferred from satellite SSH anomaly, which from (2.1-1) is:

$$T_O = <T> + F_T\, \delta\eta_{sa}. \qquad (2.1\text{-}4)$$

In (2.1-4), $<T> = T_C$, the climatological mean temperature. The assimilation effect is such that $T_A \approx T_O$ in regions where the correlation is high, but $T_A \approx T$, where the correlation is small. Also, to minimize potential satellite errors near the coast, the assimilation is restricted to regions where water depths are > 500 m, thus excluding the shelves.

Satellite altimeter data, AVISO (Archiving, Validation, and Interpretation of Satellites Oceanographic), are obtained from the French Space Agency. The data product was created by merging TOPEX/Poseidon (T/P) and ERS-1 & -2 altimeter measurements (Ducet et al., 2000). The combined, inter-calibrated altimeter data are interpolated in time and space using a global objective analysis. The length scale of the interpolation varies with latitudes, and is about 200 km at mid-latitudes. The e-folding time scale is set at 10 days in the tropics and 15 days elsewhere. The resulting satellite product has a spatial resolution of 0.25^o x 0.25^o and is

provided at 10-day intervals. The merged T/P + ERS-1&2 SSH anomaly maps provide reduced and more homogeneous mapping errors than either individual data set, and thus, more realistic statistics. Fratantoni (2001) compared AVISO- and drifter-derived kinetic energy and found reasonable agreements. Wang et al. (2003) checked the AVISO data against two-year direct current measurements in the DeSoto Canyon, and found that their first two SVD (Single Value Decomposition; Bretherton et al. 1992) modes agreed. Oey et al. (2003) found that in the Gulf the AVISO data agreed well with those obtained from the Colorado Center for Astrodynamics Research (Leben et al. 2002). In this work, the AVISO data from 1992/October through 1999 are used. Figure 2.1-3 shows an example of the assimilated result.

2.1.2 Data Assimilation in the Princeton Ocean Model

POM has a number of options for different data assimilations. The various forms are all based on standard optimal interpolation (or Multivariate OI or MVOI; e.g. Daley, 1991). They differ only in the details in which the various data are utilized and how the error covariance matrix is defined. The data (at present) consist of satellite sea-surface height anomaly (SSH), sea-surface temperature (SST), (described in the previous section), moored temperatures and currents, hydrography, and drifters. One can in principle also incorporate other data (e.g. CODAR, SOFAR etc). Given the observed (anomaly) vector $w_\beta{}^o$, the model 'forecasts' (or first-guess) $w_i{}^f$ at N grid points, 'i', that is corrected to obtain an analyzed vector $w_i{}^a$ according to:

$$w_i{}^a = w_i{}^f + \sum_{\beta=1}^{M} K_{i\beta}[w_\beta{}^o - \sum_{i=1}^{N}(H_{\beta i} w_i{}^f)]. \qquad (2.1\text{-}5)$$

Greek subscripts denote the M observational locations, $K_{i\beta}$ is the Gain matrix (or weights), and H_β interpolates modeled values onto the observational point. $K_{i\beta}$ is obtained by minimizing the square of the analysis error $E_i{}^a = <(w_i^a - w_i)^2>$, where w_i is the 'truth' and the angle brackets denote (time or ensemble) averaging. Thus,

$$\sum_{\beta=1}^{M} K_{i\beta}(HP^f H^T + P^o)_{\beta\alpha} = (P^f H)_{i\alpha}, \qquad (2.1\text{-}6a)$$

where

$$P^f_{\alpha\beta} = <(w^f_\alpha - w_\alpha)(w^f_\beta - w_\beta)> \qquad (2.1\text{-}6b)$$

$$P^o_{\alpha\beta} = <(w^o_\alpha - w_\alpha)(w^o_\beta - w_\beta)> \qquad (2.1\text{-}6c)$$

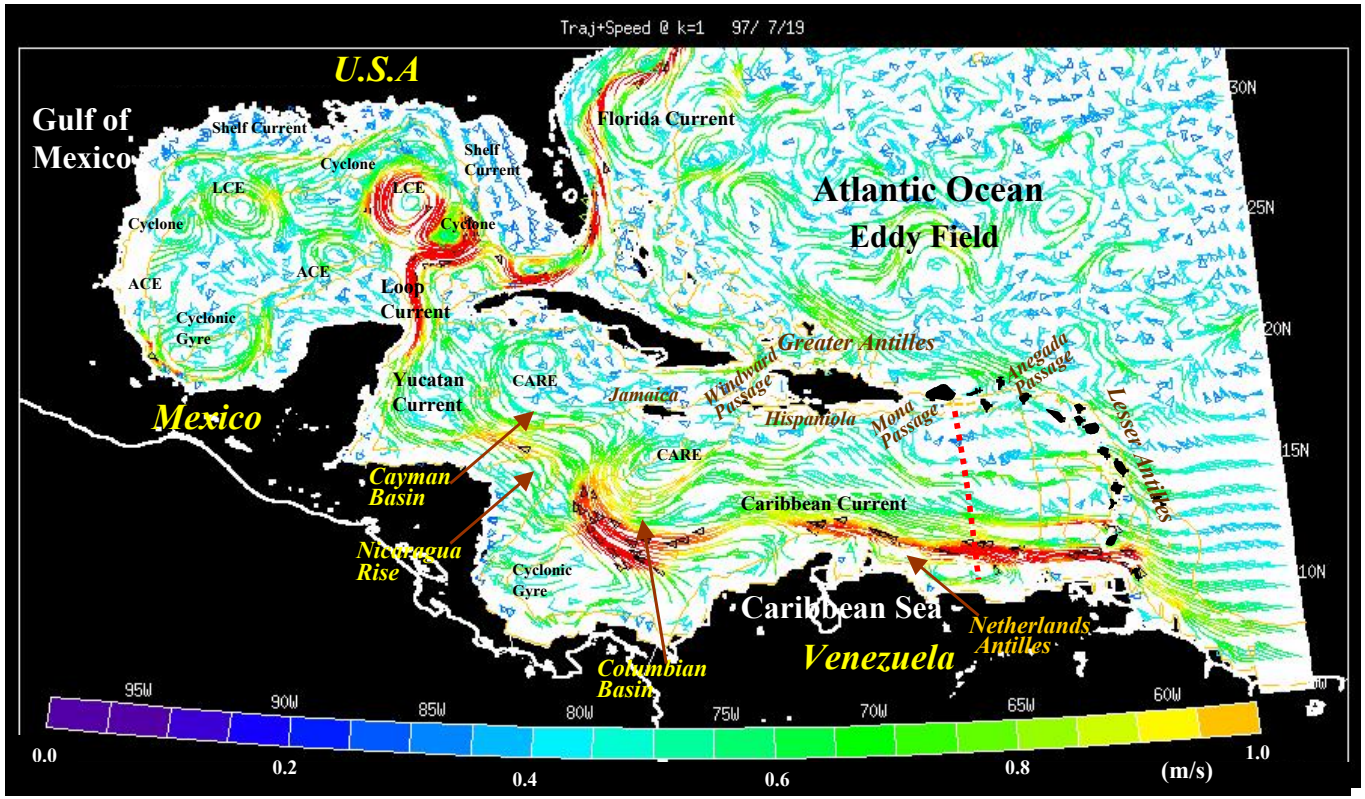

YC: Yucatan Current
LC: Loop Current
LCE: Loop Current Eddy

CARE: Caribbean Eddy
ACE: (Smaller) Anticyclone

Figure 2.1-3. An example of the regional, near-surface circulation obtained from the data-assimilated run (from Oey, et al., 2003a). Plotted are ten-day Eulerian trajectories $\mathbf{x} = \mathbf{x}_o + \int \mathbf{u}\, dt$, where $\mathbf{x}$ and $\mathbf{u}$ are position and velocity vectors respectively, and the integration is over ten days. The trajectories are launched from July 19 through July 28, 1997, and from every 8th grid point at the first sigma level (i.e. surface). Colors indicate speeds such that greenish blue is ≈ 0.5 m s^{-1} and red is ≥ 1 m s^{-1}.

are the space-time correlations of the 'forecast' error and observational error, respectively. Since w_α is usually not known, various levels of approximation must be made for $P^f_{\alpha\beta}$ and $P^o_{\alpha\beta}$, hence $K_{i\beta}$.

Level 1:

Here the $K_{i\beta}$ is analytically specified (and in general not "optimum"), and

$$K_{i\beta} = \Gamma_{ij}\Lambda_{j\beta} \text{ and } \Lambda_{i\beta}H_{\beta j} = I_{ij}, \tag{2.1-7a}$$

where

$$\Gamma_{ij} = \frac{2\Delta t}{t_a}\exp(-\frac{t-t_{0i}}{t_d})\delta_{ij}(\sum_{\beta=1}^{M}\lambda_{i\beta})/M, \tag{2.1-7b}$$

$$\Lambda_{i\beta} = \frac{\lambda_{i\beta}}{\sum_{\beta=1}^{M}\lambda_{i\beta}} \tag{2.1-7c}$$

$$\lambda_{i\beta} = \exp(-\frac{x_{i\beta}^{\ 2}}{R_x^{\ 2}} - \frac{y_{i\beta}^{\ 2}}{R_y^{\ 2}} - \frac{z_{i\beta}^{\ 2}}{R_z^{\ 2}}), \tag{2.1-7d}$$

I_{ij} is the unit matrix, δ_{ij} is the Kronecker delta function, Δt is the assimilation time step, t_a is the assimilation time scale (shorter for stronger assimilation), t_{0i} is the most recent time when observation is available at point 'i,' t_d is the time influence of the observational data, $(x,y,z)_{i\beta}$ is the distance between the model and observational grid points, and $R_{x,y,z}$ are (x, y, z) scales, respectively, that measure the radius of influence of observation and M is the number of observational locations. Typically $(t_a, t_d) \approx$ *hours to days*, and $(R_x, R_y, R_z) \approx$ (*10's km*, *10's km*, *10's m*), taken to be independent of grid point 'i.'. To put in more 'physical flavor,' it can be shown that if Δt = model time step (using a '*leap-frog*' scheme), (2.1-5) and (2.1-7) lead to:

$$\frac{\partial w_i^f}{\partial t} = (physics) + \sum_{j=1}^{N}\Gamma_{ij}(\tilde{w}_j^o - w_j^f) \tag{2.1-8a}$$

$$\tilde{w}_i^o = (\sum_{\beta=1}^{M}\lambda_{i\beta}w_\beta^o)/(\sum_{\beta=1}^{M}\lambda_{i\beta}), \tag{2.1-8b}$$

which is the nudging method. Fan et al. (2003) used this scheme to assimilate observed drifters (see Chapter 5).

Level 2 ("Standard OI"):

Here, $P^o_{\alpha\beta}$ is diagonal and $P^f_{\alpha\beta}$ is Gaussian:

$$P^o_{\alpha\beta} = \sigma^2 \delta_{\alpha\beta} \tag{2.1-9a}$$

$$P^f_{\alpha\beta} = < \delta w^2_\alpha > \exp(-\frac{x^2_{\alpha\beta}}{R^2_x} - \frac{y^2_{\alpha\beta}}{R^2_y} - \frac{z^2_{\alpha\beta}}{R^2_z} - \frac{t^2_{\alpha\beta}}{R^2_t}) , \tag{2.1-9b}$$

where σ is the standard deviation of observational error (assumed constant), $< \delta w^2_\alpha >$ is the (model) variance, and as before $x_{\alpha\beta} = x_\alpha - x_\beta$ etc., and R_x etc. are scales. This (equations 2.1-9, 2.1-2 and 2.1-1) is the scheme used in POM for assimilating the satellite SSH and SST (Mellor and Ezer, 1991; Wang et al., 2003; Oey et al., 2003a).

Level 3a:

Here, $P^o_{\alpha\beta}$ is given by (2.1-9a) but $P^f_{\alpha\beta}$ is computed from (2.1-2b) by assuming the model and observed climatologies are the same and 'truths.' Then $P^f_{\alpha\beta}$ is just the model covariance.

Level 3b:

Here, the observed are assumed to be 'truths.' Thus $P^o_{\alpha\beta} = 0$ and $P^f_{\alpha\beta}$ is computed from (2.1-2b) with $w_\alpha = w^o_\alpha$.

Level 3c:

Here, a complete hindcast is first made with the *Level-1* scheme. This is then used in *Level-3b* to pre-compute $P^f_{\alpha\beta}$. This hindcast is then repeated but at each time step, the pre-computed $P^f_{\alpha\beta}$, hence $K_{i\beta}$ from (2.1-2), are used to correct the first-guess $w_i{}^f$. Dong and Oey (2003; unpublished work) found this scheme to give good 'prediction' at points where no data were assimilated.

2.2 Observational Database

The observational database used for analysis and comparison with model simulations consists mainly of time series of currents and temperatures from moored instruments in deep water, and hydrographic data from surveys of northern slope waters and LC eddies. The moored data is from a number MMS programs beginning in 1983, and the hydrographic data is primarily from the GulfCet I and LATEX C surveys, from the early 1990's, of the northern slope. In Chapter 5, near-surface Lagrangian drifter data, deployed in the region of the DeSoto Canyon as part of the MMS studies in the Northeast Gulf (Hamilton et al., 2000; Jochens et al., 2002), were used for

model assimilation studies. These drifter data are described in Chapter 5.2, as they were not part of the main study. The current and hydrography databases are described in the next two sections.

2.2.1 Currents

The positions of moorings, in deep water, with deployments longer than 6 months are given in Figure 2.2-1. This is not the complete inventory of deepwater moorings, but only the ones that were used for this study. The depths and time periods of the current data are given in Table 2.2-1. All these data were available from the SAIC database management system and therefore, had been processed so that deployments had been concatenated, and time series had been quality-assured and filtered with 3 and 40-hour low-pass Lanczos kernels, with decimations to 1 and 6-hour time steps, respectively. In some cases a 7-day low pass filter, with decimation to 1-day intervals, was also used for analysis of longer-period fluctuations.

Table 2.2-1 Deep Current Meter Moorings

Mooring ID (Reference)	Deployment Period	Water Depth (m)	Current Meter Depth (m)	Instrument Type
MMS Gulf of Mexico Physical Oceanography Program: Years 1, 2 and 4				
A (SAIC, 1987)	Jan 1983-Feb 1986	1,700	172	NWCM
			400	"
			738	"
			1,100	"
			1,600	"
G (SAIC, 1987)	Jan 1984-Jan 1986	3,200	177	NWCM
			397	"
			703	"
			1,565	"
			2,365	"
			3,174	"
MMS Gulf of Mexico Physical Oceanography Program: Year 3				
P (SAIC, 1988)	Jun 1985-May 1986	2,000	30	RCM
			300	"
			1,000	"
			1,500	"
Q (SAIC, 1988)	Jun 1985-May 1986	3,000	100	RCM
			300	"
			1,000	"
			1,500	"
R (SAIC, 1988)	Jun 1985-May 1986	3500	100	RCM
			300	"
			1,000	"
			1,500	"
			3,000	"

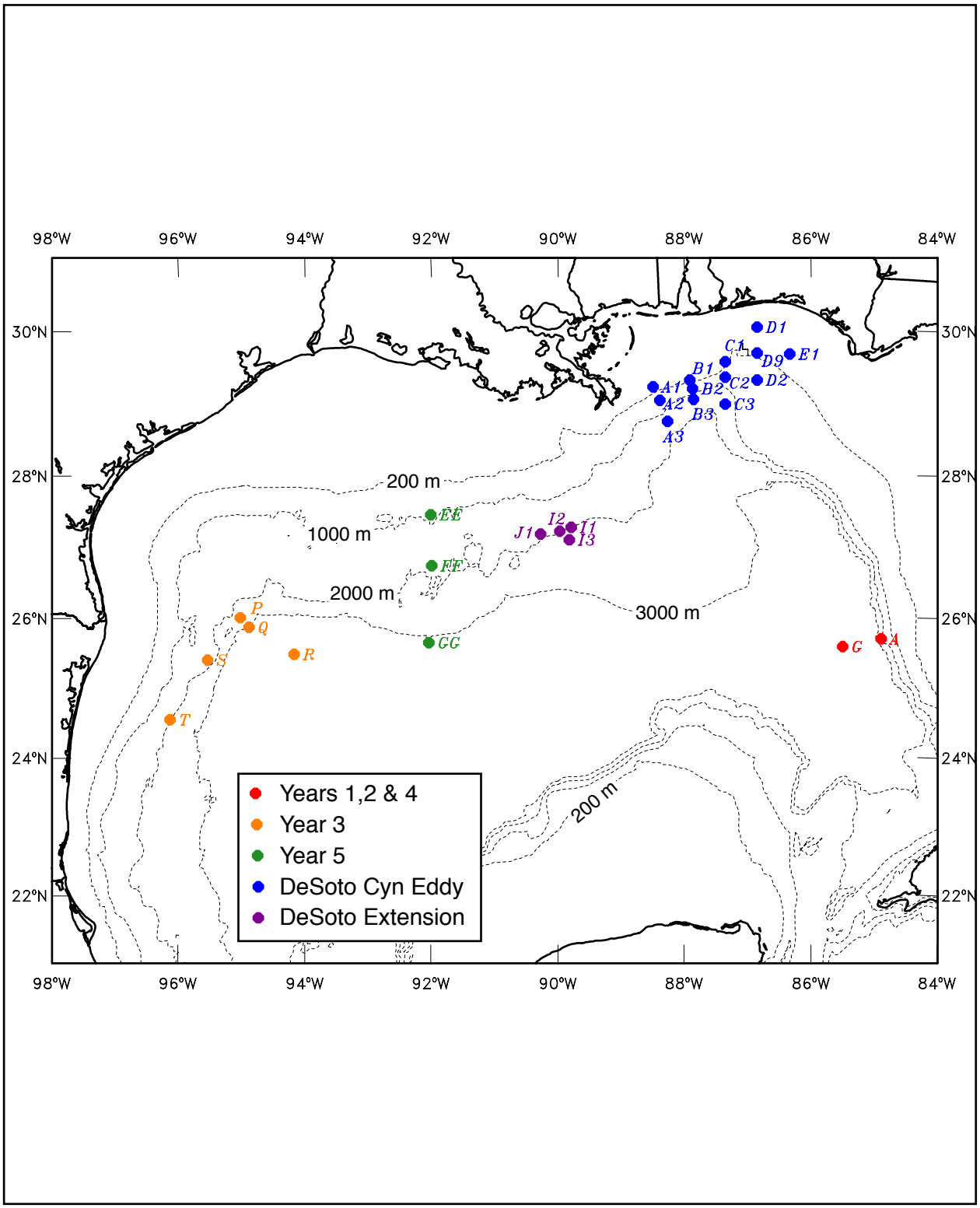

Figure 2.2-1. Locations of deepwater moorings used in this study. Moorings are color coded by program. "Years" refer to data collection years of the Gulf of Mexico Physical Oceanography Program.

Table 2.2-1 (continued)

Mooring ID (Reference)	Deployment Period	Water Depth (m)	Current Meter Depth (m)	Instrument Type
S (SAIC, 1988)	Jun 1985-May 1986	1,500	100 300 1,000	RCM “ “
T (SAIC, 1988)	Jun 1985-May 1986	2200	100 300 1,000	RCM “ “
MMS Gulf of Mexico Physical Oceanography Program: Year5				
EE (SAIC, 1989)	Apr 1987-Nov1988	845	100 300 725	NWCM “ “
FF (SAIC, 1989)	Apr 1987-Nov1988	1750	100 300 725 1,650	NWCM “ “ “
GG (SAIC, 1989)	Apr 1987-Nov1988	3,000	100 300 725 1,650 2,500	NWCM “ “ “ “
DeSoto Canyon Eddy Intrusion Study				
A1 (Hamilton et al., 2000)	Mar 1997-Apr 1999	100	12-72 95	ADCP (4 m cells) S4
A2 (Hamilton et al., 2000)	Mar 1997-Apr 1999	500	12-72 200 300 490	ADCP (4 m cells) RCM “ S4
A3 (Hamilton et al., 2000)	Mar 1997-Apr 1999	1300	12-68 500 1290	ADCP (4 m cells) RCM NWCM
B1 (Hamilton et al., 2000)	Mar 1997-Apr 1999	100	12-72 95	ADCP (4 m cells) S4
B2 (Hamilton et al., 2000)	Mar 1997-Apr 1999	500	12-72 200 300 490	ADCP (4 m cells) RCM “ NWCM

Table 2.2-1 (continued)

Mooring ID (Reference)	Deployment Period	Water Depth (m)	Current Meter Depth (m)	Instrument Type
B3 (Hamilton et al., 2000)	Mar 1997-Apr 1999	1300	12-68 500 1290	ADCP (4 m cells) RCM NWCM
C1 (Hamilton et al., 2000)	Mar 1997-Apr 1999	100	12-72 95	ADCP (4 m cells) S4
C2 (Hamilton et al., 2000)	Mar 1997-Apr 1999	500	12-72 200 300 490	ADCP (4 m cells) RCM “ S4
C3 (Hamilton et al., 2000)	Mar 1997-Apr 1999	1300	12-68 500 1,290	ADCP (4 m cells) RCM NWCM
D1 (Hamilton et al., 2000)	Mar 1997-Apr 1999	100	12-68 95	ADCP (4 m cells) S4
D2 (Hamilton et al., 2000)	Mar 1997-Apr 1999	500	12-72 200 300 490	ADCP (4 m cells) RCM “ S4
D9 (Hamilton et al., 2000)	Mar 1997-Apr 1999	200	21-152	ADCP (9 m cells)
E1 (Hamilton et al., 2000)	Mar 1997-Apr 1999	100	12-72 95	ADCP (4 m cells) S4

Table 2.2-1 (continued)

Mooring ID (Reference)	Deployment Period	Water Depth (m)	Current Meter Depth (m)	Instrument Type
DeSoto Canyon Eddy Intrusion Extension				
I1 (Hamilton et al., 2003)	Sep 1999-Sep 2001	2,000	12-68	ADCP (4m)
			122-250	"
			256-368	"
			372-588	ADCP (8m)
			658-1,202	"
			800	RCM
			1,000	"
			1,200	"
			1,400	"
			1,600	"
			1,800	"
			1,989	NWCM
I2 (Hamilton et al., 2003)	Sep 1999-Sep 2001	1998	1,600	RCM
			1,800	"
			1,989	NWCM
I3 (Hamilton et al., 2003)	Sep 1999-Sep 2001	2175	1,775	RCM
			1,975	"
			2,164	NWCM
I4 (Hamilton et al., 2003)	Feb 2001-Sep 2001	1957	1,557	NWCM
			1,757	RCM
J1 (Hamilton et al., 2003)	Sep 1999-Aug 2000	1373	972	RCM
			1,172	"
			1,361	NWCM

ADCP – RDI Acoustic Doppler Current Profiler (Narrow & Broad Bands, LongRanger)
RCM - Aanderra Current Meter (versions 4,5,7,8 & 9)
NWCM – General Oceanics Niskin Winged Current Meter (Mks I, II & III)
S4 – Inter Ocean S4 Current Meter

2.2.2 Hydrography

The slope aircraft surveys of LATEX C (Berger et al. 1996; Hamilton et al., 2002), and the ship-based surveys of GulfCet I (DiMarco, Personal Communication), are the primary data sources. The former used AXBT's and the latter XBT's and CTD's. All the (A)XBT data were converted to CTD's as discussed by Hamilton et al. (2002). The (A)XBT's are corrected for depth offsets, relative to a CTD, using the formulae given by Singer (1990), then salinities are estimated from nearby CTD stations that were taken within one month of the XBT data. In some cases the CTD data was from different years than the (A)XBT data. This is a reliable procedure because of the tight T-S relation in the Gulf for temperatures less than about 16°C. The scatter in the T-S in the surface layers leads to errors in the surface dynamic height, relative to 780dbar (the deepest depth of the stretched XBT profiles), of ~ 2 and 5 dynamic cm if the CTD data used are from the same or different years, respectively. Details are given in Hamilton et al. (2002).

The dynamic height calculations for the slope region employ the method given by Csanady (1979) for integrating the bottom density profile across the isobaths. Only stations with bottom depths less than 780 m on the upper slope require the integration of bottom densities from south to north along the cross-slope transects. The method is considered accurate if the bottom σ_t isolines are approximately parallel to the isobaths, so that integration along a transect is independent of position. This assumption is usually reasonable on the upper slope. The assumed level of no motion at 780 dbar, though dictated by the XBT profiles, is also reasonable, given that the region of minimum energy in the current profile is between 800 and 1,200 m (Hamilton et al., 2000). Dynamic height and derived σ_t profiles are the basis of the higher order analyses given in the next section.

A total of 21 AXBT flights and 7 GulfCet cruises were processed and the resulting fields mapped to grids. The station positions for two AXBT and one GulfCet surveys are shown in Figure 2.2-2. Stations from more than one survey are often combined to increase the area of coverage if they were taken within about a week of each other. The surveys in Figure 2.2-2 are extensively used in Chapter 4. Some of the aircraft surveys deployed AXCP's, which provide velocity shear profiles. AXCP velocity data was treated as in Hamilton et al. (2002), by smoothing with least-square splines with a length scale of 50 m, and removing a barotropic offset. The latter was estimated from regions near the bottom of the velocity profiles that exhibit no shear, as in Sandford et al. (1987).

The processed salinity, temperature and σ_t profiles were mapped to horizontal grids using the statistical interpolation method given by Pedder (1993), which is an iterative method similar to the Barnes (1964) two-pass scheme and its successors. The length scale used by the Gaussian influence function is estimated as the mean separation of the station positions over the grid. This is about 40 and 50 km for the AXBT and GulfCet surveys, respectively. The method is iterated to convergence so that the differences between interpolated and observed fields at the station positions are minimized. However, for noisy calculations that difference the gridded fields (e.g. relative vorticity), some smoothing is often useful and this is achieved by limiting the number of iterations (Pedder, 1993). The interpolation method to a regular horizontal grid can employ either a equally spaced or the model's curvilinear grid (see section 2.1). The former is used for analyses, and the latter for the assimilation of observations into the model runs.

2.3 Analysis Tools

2.3.1 Topographic Rossby Waves and Ray Tracing

The fluctuations of observed lower-layer currents have a wave-like nature consisting of the nearly barotropic flows in the lower 1,000 m of the water column. Rhines (1970) first gave the theory of topographic Rossby waves using quasi-geostrophic (QG) dynamics (Pedlosky 1979). Important features of TRW theory are:

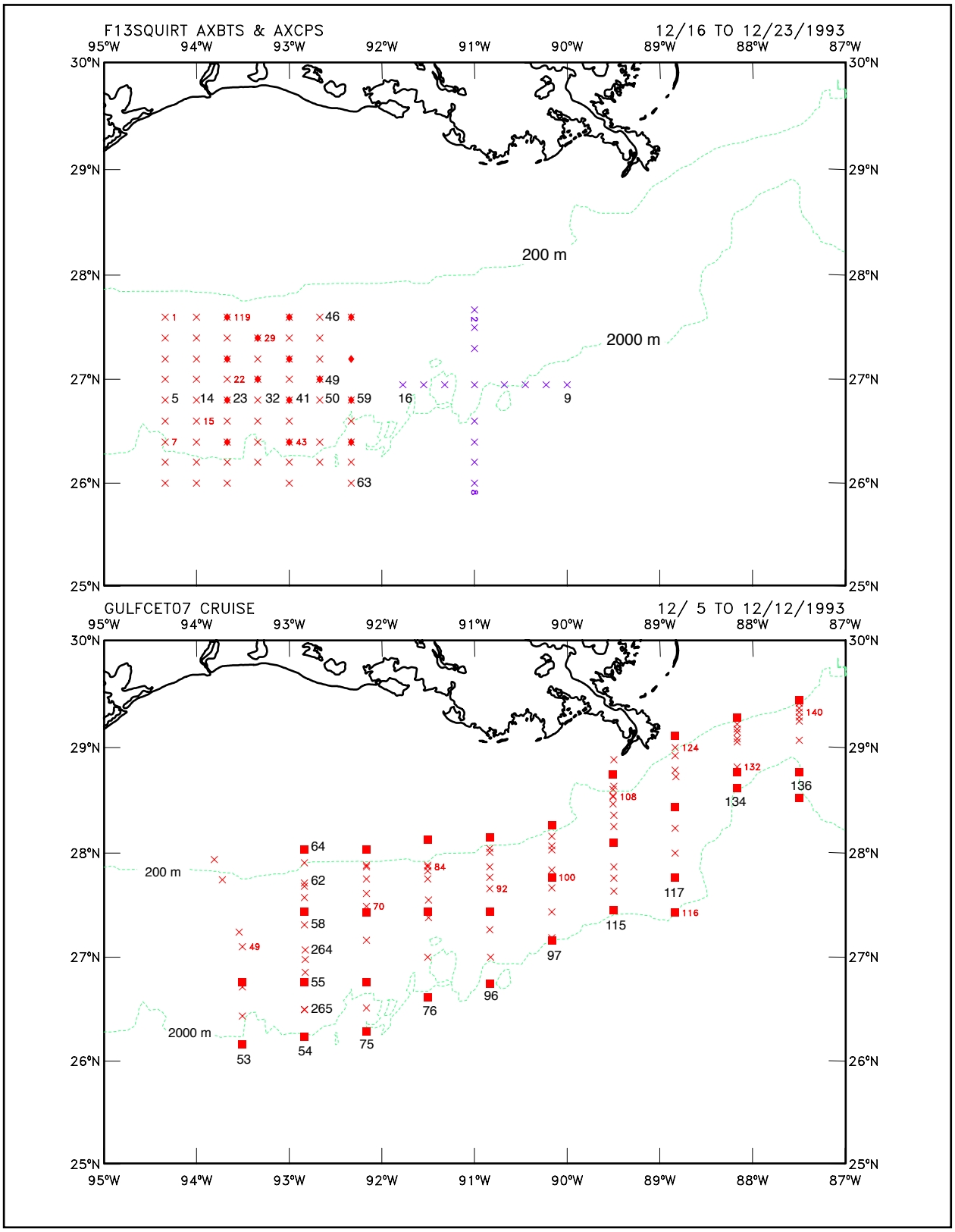

Figure 2.2-2. Station position maps for F13SQUIRT/F14LEDDY (top panel) and GULFCET07 (bottom panel). Station types are X - (A)XBT, Solid Square - CTD and Solid Diamond (AXCP). In the top panel the F14LEDDY stations are purple.

1. The wave motion is bottom intensified; thus current amplitudes increase in magnitude towards the bottom.
2. There is no phase difference between currents at different depths; therefore at any particular wave frequency, the motion is columnar.
3. The maximum frequency or cutoff frequency for TRW's is $N\alpha$ where α is the bottom slope, defined as normal to the general trend of the isobaths, and N is the Brunt-Väisälä frequency of the lower water column. Bottom slopes are defined over scales similar to the wavelengths of TRW's (~ 50 to 100 km). The effect of small or large perturbations of the bottom slope on TRW propagation is not covered by present linear theories. The wave frequency, ω, is proportional to the bottom slope and the cosine of the angle that the wavevector makes with the isobaths. At the highest allowed frequency, the phase velocity is parallel to the isobaths such that shallow water is on the right of the direction of wave propagation.
4. At the highest allowed frequency, wave motions are rectilinear and perpendicular to the phase vector and isobaths. At lower frequencies the wave motions become more parallel to the isobaths. Longer wave-length motions are also less bottom trapped than high frequency waves.
5. TRW's are dispersive and it can be shown that if the phase vector is directed into deeper water, then the energy flux has component towards the shallower water (Thompson, 1977). TRW's are refracted by changing topography. These ray-paths can be calculated by WKB theory which assumes that the environment (e.g. bottom slopes) change "slowly " compared to the wavelength of the motions. This is rarely strictly true in practice.

TRW ray paths in this study are calculated using the QG dispersion relation. The basis of the method is given in Meinen et al. (1993) and used by Pickart (1995) to calculate TRW ray paths generated by the deep Gulf Stream in the Middle Atlantic Bight. The dispersion relation for TRW's is given by the coupled equations (Pickart, 1995; Oey and Lee, 2002):

$$\mu^2 = (K^2 + \beta k/\sigma)\,(N/f)^2 \qquad (2.3\text{-}1a)$$

$$\mu \tanh(\mu h) = N^2/(\sigma f)\,(\mathbf{K} \times \nabla h)_z \qquad (2.3\text{-}1b)$$

where h is the water depth,
$N = (-g/\rho_0\,\partial_z\rho)^{1/2}$ is the Brunt-Väisälä frequency (assumed constant),
f is the Coriolis parameter using the β-plane assumption,
$\mathbf{K} = (k, l)$ is the wavenumber vector in east and north (x, y) coordinates,
σ is the wave frequency,
$1/\mu$ is the vertical trapping scale of the wave, and
∇ $(= \mathbf{i}\,\partial_x + \mathbf{j}\,\partial_y)$ is the horizontal gradient operator.

The subscript 'z' is the vertical component of the vector, thus $(\mathbf{K} \times \nabla h)_z = (k h_y - l h_x)$. For typical $N/f \approx 10$ and maximum slope gradients $|\nabla h| < \approx 0.05$ used in the model, it can be shown that the QG dispersion is valid for wave periods ≥ 20 days. The model analyses focus solely on waves

with periods > 20 days. When topographic slope dominates, $\beta_{Topo} = f|\nabla h|/h >> \beta$, and the β-term can be dropped. Then μ can only be real and it becomes the inverse vertical trapping scale of the wave. Equations (2.3-1) then give,

$$\sigma \tanh(NhK/|f|)/N = \mathrm{sgn}(f)\ (\mathbf{n_K}\times\nabla h)_z \qquad (2.3\text{-}2)$$

where $\mathbf{n_K}=\mathbf{K}/K$ is the wavenumber unit vector, and sgn(f) = sign of 'f'. Without loss of generality, σ can be taken to be >0, so that $(\mathbf{n_K}\times\nabla h)_z$ must have the same sign as sgn(f). Thus the phase propagation direction must lie to the right (left) of the direction of increasing water depth in the northern (southern) hemisphere. In other words, the wavenumber vector makes a *clockwise (anti-clockwise)* angle θ with respect to the direction of steepest topographic decent (i.e. with $\nabla h/|\nabla h|$). For $NhK/|f| \approx O(1)$ or larger (which typically requires wavelengths < 200 km), $\tanh(NhK/|f|)\approx 1$ or at most a weak function of "NhK/|f|," and (2.3-2) shows that the frequency σ is independent of the magnitude of the wavenumber, and depends only on the angle that the wavenumber vector makes with the x or y-axis. It follows then that the component in the direction of **K** of the rate of change of frequency in the wavenumber space, $\mathbf{n_K}\bullet\nabla_\mathbf{K}\sigma$, where $\nabla_\mathbf{K}=(\partial/\partial k, \partial/\partial l)$, must be zero, since this direction is by definition fixed and σ itself depends on it only, and not on the magnitude K. Thus, the wavenumber vector and group velocity $\mathbf{C_g}$ $(=\nabla_\mathbf{K}\sigma)$ must be perpendicular to each other. Moreover, (2.3-1b) (with $\tanh(NhK/|f|)\approx 1$) gives

$$\mathbf{C_g} = N\ \mathbf{n_K}\bullet\nabla h\ (\ l, -k)/K^2, \qquad (2.3\text{-}3)$$

so that $\mathbf{C_g}\times\mathbf{K} = N\mathbf{n_K}\bullet\nabla h = N|\nabla h|\cos(\theta)$. Thus $\mathbf{C_g}$ is directed clockwise (upslope) with respect to **K** when the latter points downslope, $0<\theta<\pi/2$, and anti-clockwise (downslope) when **K** points upslope, $\pi/2<\theta<\pi$ (Figure 2.3-1).

Under the WKB approximation, where changes in wave amplitude and phase caused by the environment are assumed to vary on scales larger than the local wavelength, the equations governing the path of a wave and its wavenumber are (LeBlond and Mysak, 1978; Lighthill, 1978):

$$D_t\,\mathbf{x} = \partial\sigma / \partial\mathbf{K} = \mathbf{C}_g \qquad (2.3\text{-}4)$$

$$D_t\,\mathbf{K} = \sum - \partial\sigma / \partial\gamma_i\ \nabla\gamma_i \qquad (2.3\text{-}5)$$

where $D_t = \partial / \partial t + \mathbf{C_g}\bullet\nabla$

is the derivative following the wavegroup, **x** is the path of the ray, and $\mathbf{C_g}$ is the group velocity, defined above. The γ_i are the environmental parameters that cause refraction of the wave. There are three such parameters for TRWs: h (water depth), ∇h (bottom slope), and N (Brunt-Väisälä frequency). Though the wavenumber vector undergoes refraction as the environmental

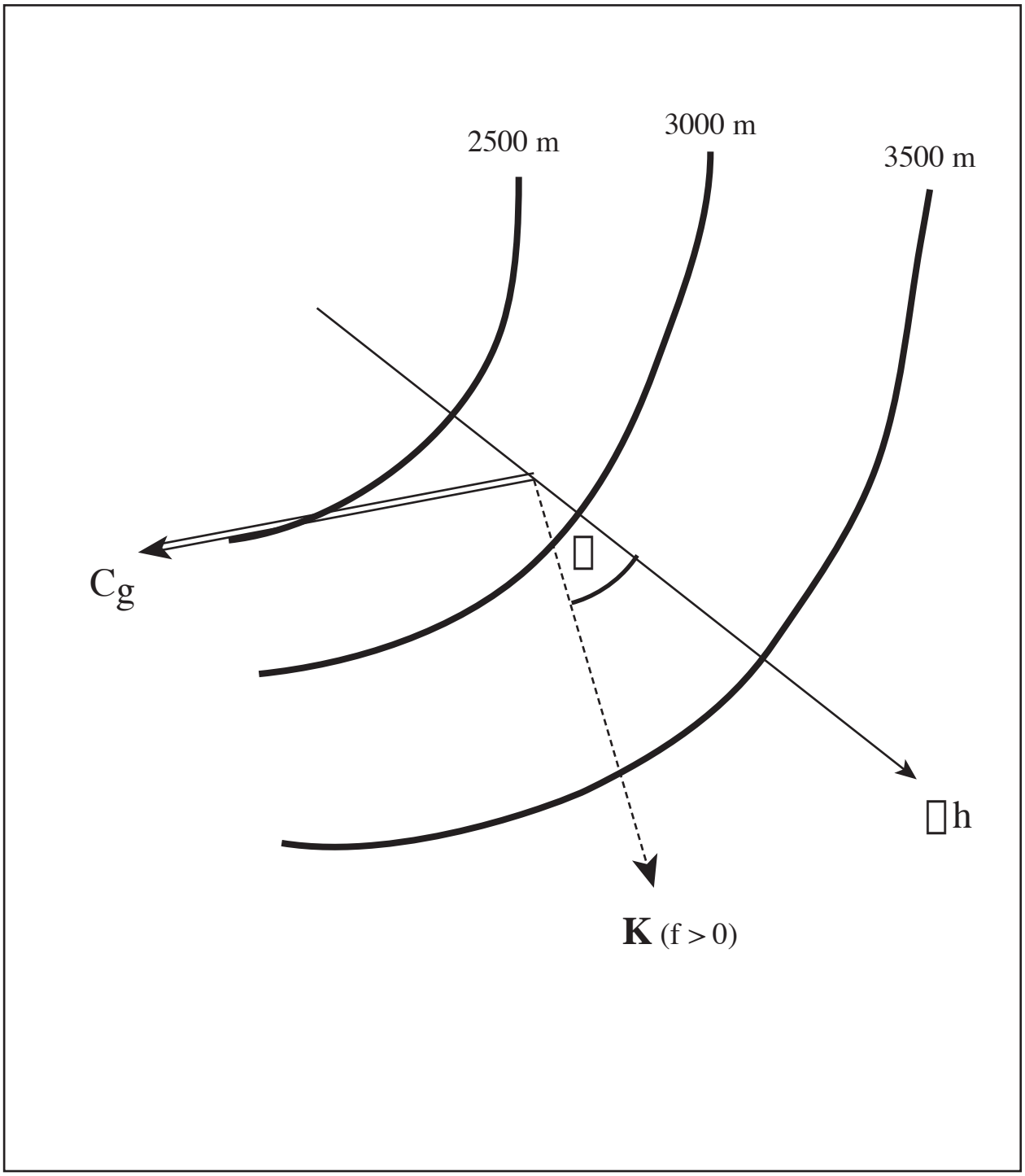

Figure 2.3-1. A schematic that describes the relations between three vectors: the gradient of water depth ∇h, wavenumber vector **K**, and the group velocity $\mathbf{C}_g$, in the northern hemisphere and when NhK/f is O(1) or larger (see text). α is the clockwise angle that **K** makes with ∇h. $\mathbf{C}_g$ is very nearly perpendicular to **K**. Moreover, $\mathbf{C}_g \times \mathbf{K} \propto \cos(\alpha)$, so that it is positive (negative) and $\mathbf{C}_g$ points upslope (downslope) when K points downslope (upslope) when $0<\alpha<\pi/2$ ($\pi/2<\alpha<\pi$). The figure shows the case $0<\alpha<\pi/2$.

parameters change along a path, the frequency remains constant, because by 2.3-4 and 2.3-5, $D_t\sigma = 0$. The WKB assumption is marginal though it is often used under conditions that have sharp changes in the environmental parameters. Therefore, the topography must be smoothed over at least the wavelength scale for the method to apply. Equations, (2.3-4) and (2.3-5), are solved using 4th order Runge-Kutta with adaptive step size methods (Press et al., 1992) to determine ray paths and the change in the wavenumber vector along the rays. The condition that the frequency must be constant along a ray path serves as a check on the numerical method.

The method requires specifications of four environmental fields: N(x,y,z,t), h(x,y), and the two components of ∇h(x,y). The topography was smoothed using a Gaussian-type interpolator (Oey et al., 2001) with a 'radius of influence' of 0.6°, comparable to the filter width of 150 km used by Pickart (1995). Figure 2.3-2 compares the smoothed topography with the original one used in the numerical simulation (see Chapter 3). The smoothing removes short-scale topographic irregularities but leaves the large-scale features (and also those of ∇h, not shown) essentially intact. To obtain a smoothed *N*, we performed time and depth averaging over the last seven years of the ten-year simulation, and also for depths below the $27.5\sigma_t$ surface (i.e. in layers 3 and 4). The resulting contours of N(x,y) are shown in Figure 2.3-2. Note that over the deep basin, $N \approx 10^{-3}$ s^{-1}. These smoothed values (N and h) are interpolated onto a longitude/latitude grid with constant grid sizes ($0.01^o \times 0.01^o$), on which ∇h is calculated using finite differences. Note that the uniform grid is used for calculating the environmental fields only, and does not define the actual coordinates of rays.

In addition to N(x,y,z,t), h(x,y) and ∇h(x,y), deep currents $\mathbf{u}_{deep}$ also affect ray paths (Oey and Lee, 2002). Figure 2.3-3 shows the modeled currents averaged over the last seven years of the ten-year simulation, at 200 m above the bottom in the Gulf (Oey et al., 2002). The modeled deep mean flow, $\mathbf{u}_{deep}=(u_1, u_2)$, is generally cyclonic around the deep Gulf. Between the 3,000 and 3,500 m contours in the northern Gulf, maximum speed reaches 0.07 m/s, but in general it is more sluggish ~0.03 m/s. Given TRW group speeds of about 10 km day^{-1}, the effects of $\mathbf{u}_{deep}$ can be as much as 50% or more at some location. To assess the effects, the ray equations (2.3-4 and 2.3–5) are modified to account for $\mathbf{u}_{deep}$ as follows (Lighthill, 1978). Firstly, the absolute frequency σ_a is connected to the relative frequency σ (i.e. relative to medium at rest) by the Doppler's relation:

$$\sigma_a = \sigma + \mathbf{u} \bullet \mathbf{K} \qquad (2.3\text{-}6)$$

Thus, the group velocity $\mathbf{C}_{ga}$ becomes

$$\mathbf{C}_{ga} = \nabla_{\mathbf{K}}\sigma_a = \nabla_{\mathbf{K}}\sigma + \mathbf{u} = \mathbf{C}_g + \mathbf{u}, \qquad (2.3\text{-}7)$$

where $\mathbf{C}_g$ is derived from (2.3-1). Thus, the ray path is defined by

$$D_t \mathbf{x} = \mathbf{C}_g + \mathbf{u}. \qquad (2.3\text{-}8)$$

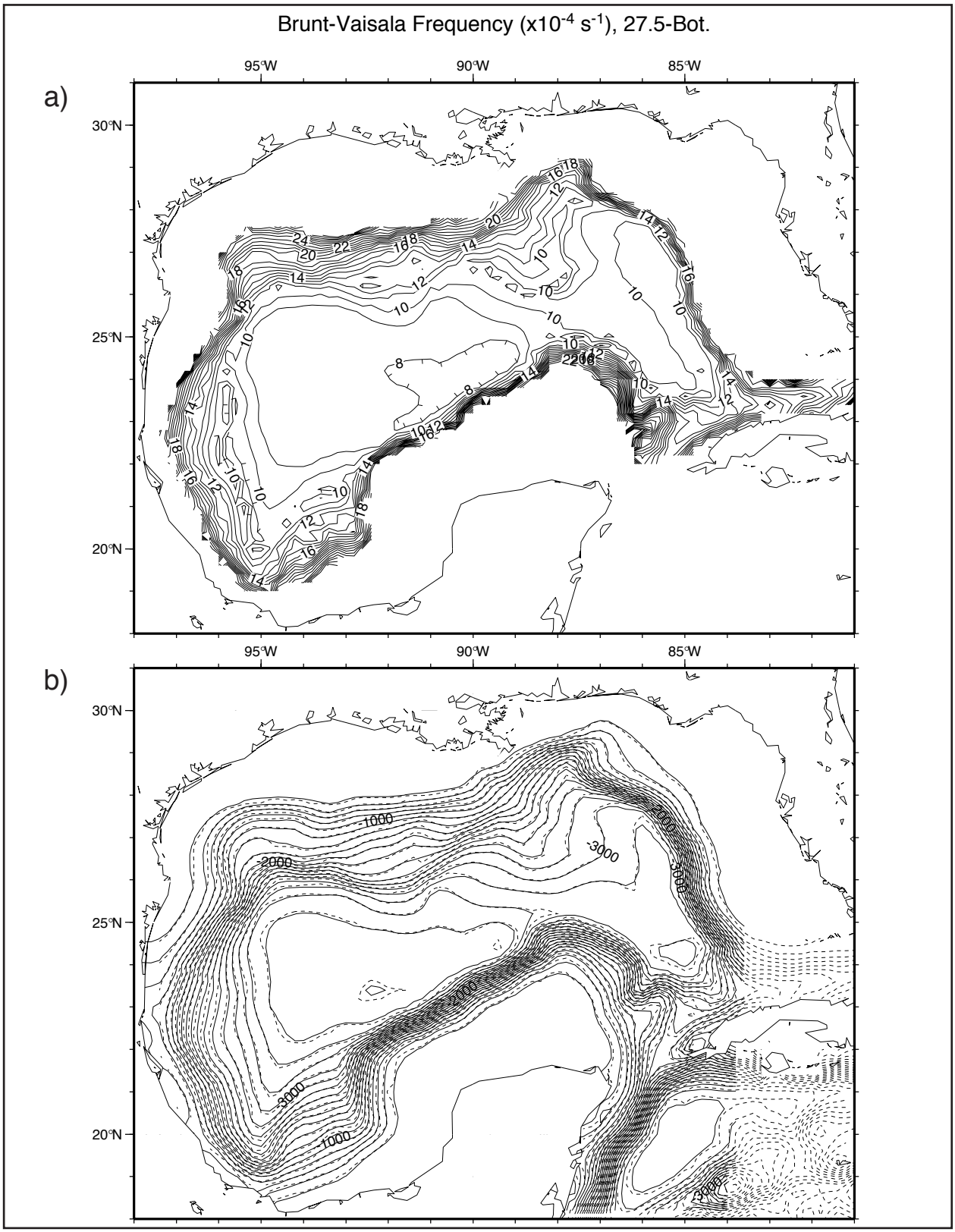

Figure 2.3-2. (a) Time (7 years) and depth (below 27.5 σ_t surface) -averaged Brunt-Väisälä frequency, N (10^{-4} s^{-1}). (b) Smoothed (solid) compared with model (dashed) topography. Smoothed fields were used in ray tracing calculations.

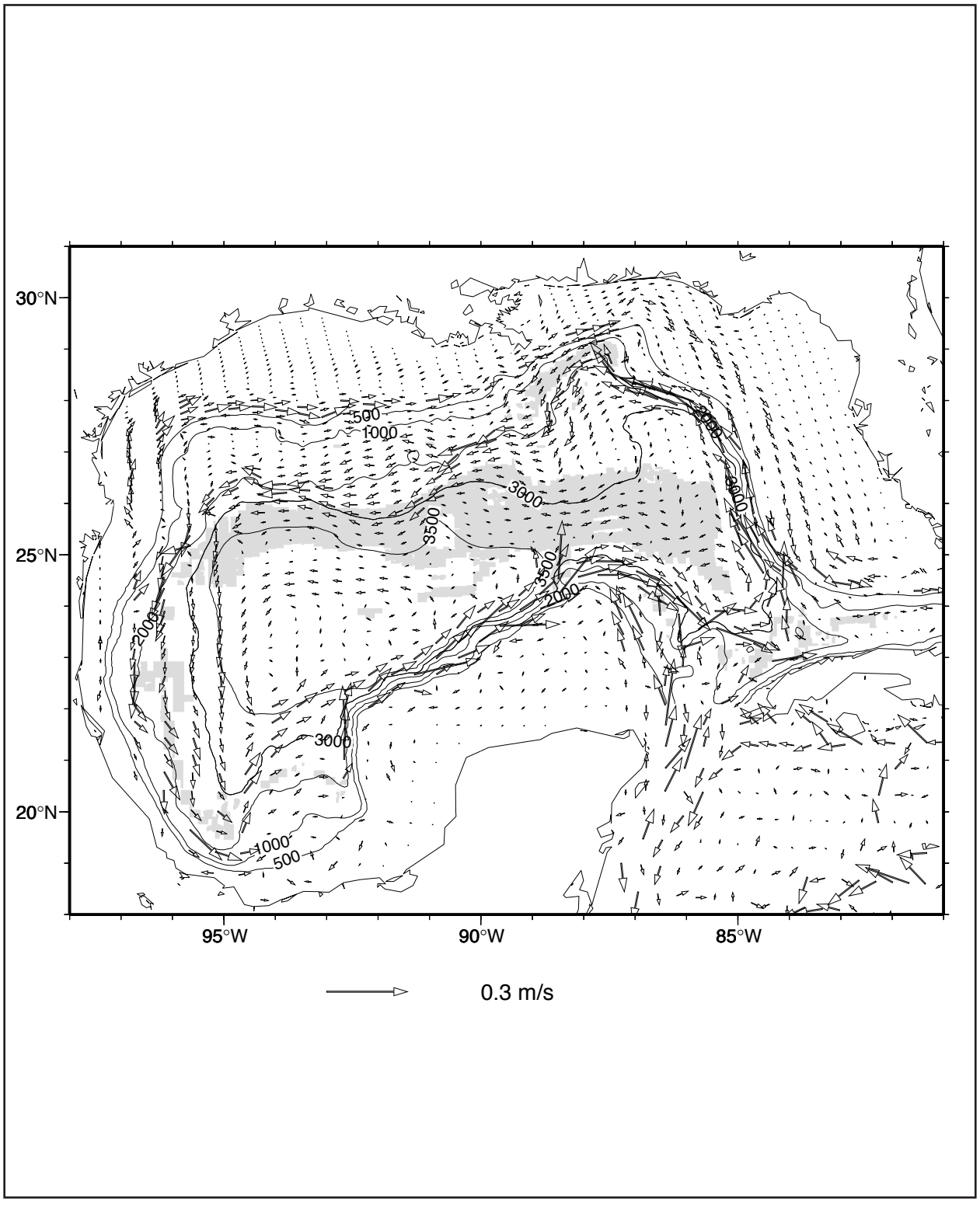

Figure 2.3-3. The modeled currents averaged over the last seven years of the ten-year simulation, at 200 m above the bottom in the Gulf from (Oey et al., 2002).

Similarly, the absolute frequency is used for the derivation of (2.3-5), to obtain

$$D_t \mathbf{K} = \sum - \partial\sigma / \partial\gamma_i \nabla\gamma_i - \mathbf{K} \bullet \nabla\mathbf{u} \qquad (2.3\text{-}9)$$

Equations (2.3-8) and (2.3-9) are used (in place of (2.3-4) and (2.3-5)) to trace rays when effects of mean flow are to be included. Multiply the x component of (2.3-9) by k and assume zonal h and N (or locally functions of the diabathic coordinate 'y' so that positive 'y' points in the opposite direction to the vector ∇h), and also $\mathbf{u}_{deep} = (u_{deep}(y),0)$, an estimate is obtained of how wavelength changes along rays embedded in a mean sheared flow:

$$D_t (k^2/2) = -l \sin(\theta)\, \partial(|h_y|N)/\partial y - kl\, \partial u_{deep}/\partial y. \qquad (2.3\text{-}10)$$

This shows that the effect of u_{deep} is that, for positive kl, the wave shortens as the ray propagates into a region of cyclonic sheared current $\partial u_{deep}/\partial y < 0$.

Using (2.3-6), (2.3-8) and (2.3-9), it can be readily shown that $D_t \sigma_a = 0$ along a ray. It follows then from (2.3-6) that $\sigma + \mathbf{u} \bullet \mathbf{K}$ is constant on a ray. Assuming a zonal shear flow and using (2.3-2), it can be estimated how rays are bent (i.e. how θ changes along rays) by the sheared current:

$$N|\nabla h|\sin(\theta) = -u_{deep}(y)\, k. \qquad (2.3\text{-}11)$$

Since $k < 0$, rays propagating upslope into a region of decreasing parabathic current (i.e. cyclonic shear), the effect of cyclonic shear alone is to bend rays back towards down-slope (i.e. θ decreases). Note that if furthermore $N|\nabla h|$ increases up-slope, then $D_t (k_i^2/2) > 0$ from (2.3-10) with $u_{deep} = 0$, and it is only necessary that $u_{deep} < 0$ for it to have the effect of bending rays down-slope.

Note that the above tacitly assumes $|\partial \mathbf{u}_{deep}/\partial z| << 1$, i.e. small vertical shears. This is consistent with slowly-varying N (over TRW wavelengths and periods) required by the use of the theory of bottom-trapped TRW; i.e. the dispersion relation (2.3-1). The results presented in chapter 3 suggest that in comparison to topographic vorticity gradient, gradients in N play a relatively minor role. While the theory is self-consistent in this regard, the question as to how a non-slowly varying N will affect ray paths, including the possible energy coupling of near-bottom with layers above, is beyond the scope of this study.

For the model, average bottom currents are readily available. Similar to the calculations for an average, horizontally varying N, a seven-year averaging was performed on the modeled currents at 200m above the bottom (Figure 2.3-3). The resulting $\mathbf{u}_{deep}$ is used in the ray calculations based on (2.3-8) and (2.3-9) to assess the effects of deep mean flows on TRW propagation.

2.3.2 Hydrographic Analyses

In classical analysis of hydrographic surveys, the distribution of potential vorticity (PV) on isopycnal surfaces is an important diagnostic of the dynamics. This is because PV is a conserved quantity in the absence of dissipation and external forces (Ertel, 1942) and can be used to analyze dynamical processes. To first order, water particles move along surfaces of constant potential density (i.e. isopycnal surfaces), and relative changes in the components of PV distributions on isopycnal surfaces occur during the formation of eddies. The discussion and derivations below follow the work of Allen and Smeed (1996) and Pollard and Regier (1992).

The Rossby-Ertel potential vorticity on an isopycnal surface is given as:

$$PV = (f + \zeta)\,(\partial\rho/\partial z)/\rho \;\big|_{\rho = \text{const}} \qquad (2.3\text{-}12)$$

Where the relative vorticity, $\zeta = \partial v/\partial x - \partial u/\partial y$, and potential density, ρ, are defined on an isopycnal surface. For horizontal scales greater than the local Rossby radius, $\zeta << f$ and the PV simplifies to:

$$PV = f\,(\partial\rho/\partial z)/\rho, \qquad (2.3\text{-}13)$$

which is usually referred to as the Sverdrup PV and depends primarily on the vertical distance between two isopycnal surfaces. For mesoscale flows in the Gulf of Mexico, $|\zeta| \approx 0.3f$, and though the Sverdrup term is dominant, the relative vorticity is an important component. Therefore, for the calculation of the Ertel PV, using (2.3-12), ζ is estimated from the geostrophic velocity components:

$$(U, V) = 1/(\rho_0 f)\,(-\partial P/\partial y, \partial P/\partial x) \qquad (2.3\text{-}14)$$

where the horizontal pressure differences are calculated from dynamic height. The horizontal dynamic height finite differences are readily calculated on sloping constant isopycnal surfaces with the assumption that the potential density surfaces are parallel over the scale of the difference estimation (usually a few kilometers). This is a good assumption in practice.

The three-dimensional velocity field can be separated into geostrophic and ageostrophic components. Thus,

$$(u, v, w) = (U, V, 0) + (u_a, v_a, w), \qquad (2.3\text{-}15)$$

where $|\mathbf{u}_a| << |\mathbf{U}|$. The equations of motion become

$$D_t U - f\,(V + v_a) = -1/\rho_0\,\partial P/\partial x \qquad (2.3\text{-}16a)$$

$$D_t V + f\,(U + u_a) = -1/\rho_0\,\partial P/\partial y \qquad (2.3\text{-}16b)$$

and the conservation of mass as

$$D_t \rho + w\, \partial\rho/\partial z = 0, \qquad (2.3\text{-}17)$$

which can be rewritten using the hydrostatic approximation as

$$N^2 w = -1/\rho_0\, D_t\, (\partial P/\partial z). \qquad (2.3\text{-}18)$$

The acceleration term, D_t, is approximated by using the geostrophic velocities (U, V), so that

$$D_t = \partial/\partial t + U\partial/\partial x + V\partial/\partial y\ .$$

Note that using (2.3-15) and (2.3-16), the ageostrophic velocity components are defined as proportional to the geostrophic acceleration terms as

$$D_t U = f\, v_a\ ;\ D_t V = -f\, u_a\ .$$

Using an f-plane assumption, differentiating (2.3-18) with respect to x and y and eliminating P from (2.3-16) generates equations for (u_a, v_a) in terms of w, U and V. The ageostrophic velocities are eliminated through continuity so that the omega or Q-vector equation becomes

$$f^2\, \partial^2_z w + \nabla^2\, (N^2\, w) = \boldsymbol{\nabla} \cdot \mathbf{Q}, \qquad (2.3\text{-}19)$$

where

$$\mathbf{Q} = [\ 2f\, (V_x\, U_z + V_y\, V_z),\ -2f\, (U_x\, U_z + U_y\, V_z)\ ]. \qquad (2.3\text{-}20)$$

For a horizontal surface, the geostrophic shear terms can be rewritten as horizontal density gradients (Wang and Ikeda, 1997), so that

$$\mathbf{Q} = [\ 2g/\rho_0\, (V_x\, \rho_y + U_x\, \rho_x),\ 2g/\rho_0\, (V_y\, \rho_y + U_y\, \rho_x)\ ]. \qquad (2.3\text{-}21)$$

Thus, **Q** can be derived from coincident interpolated dynamic height, and σ_t or σ_θ fields at any given depth level using (2.3-21). Equation (2.3-19) states that given suitable boundary conditions, the vertical velocity field can be diagnosed from the geostrophic velocity field. However, the vector **Q** and its divergence or convergence can be used directly to infer where up- and down-welling velocities, respectively, are likely to occur, without directly solving (2.3-19).

2.3.3 SVD Analysis

As one of the contributions to other studies, this project provided the current data from the *DeSoto Canyon Eddy Intrusion Study* (see Table 2.2-1 and Figure 2.2-1), as well as model runs, to a project that investigated how well the POM, with assimilation, could reproduce the dominant flow patterns in the DeSoto Canyon. The results were reported in Wang et al. (2003). The statistical technique used by Wang et al. (2003) to see if simulated and observed flow patterns had similar characteristics is called Singular Value Decomposition (SVD) analysis, which was introduced by climate studies, where similar problems of comparing model output with

observations where the flow fields are not fully deterministic arise (Bretherton et al. 1992; Lau and Weng, 2001; Robertson et al., 2000). The approach explores the possibility that model results may contain comparable spatial and temporal patterns with the observed currents, even if local (point-wise) correlations between the model and observations are low. The approach is slightly different from using Composite Principal Component Analysis (CPCA), which applies EOF analysis to combined spatial series from the model and observations, and Bretherton et al. (1992) have shown that SVD gives a better representation of the significant coupled patterns than CPCA (see also Wallace et al., 1992). Since this is an important method that should be increasingly applied to the comparison of models with spatially dense observations, where non-deterministic flows such as eddies are predominant, the basics of the SVD analysis are repeated here from Wang et al. (2003).

Both model and observational currents are mapped to coincident grids. In Wang et al. (2003), the mapping was performed using the Universal Co-Kriging (UCK) method of Pedder (1989) because daily maps of geopotential were required for comparison with SSH anomalies from altimeter data. Following Bretherton et al. (1992), the spatial vector time series *s(t)* and *z(t)*, can be expanded in terms of a set of patterns (*NS* and *NZ* are the vector dimensions in s(t) and z(t)):

$$s(t) \leftarrow \tilde{s}(t) = \sum_{k=1}^{NS} a_k(t)\, p_k \qquad \text{(2.3-22a)}$$

$$z(t) \leftarrow \tilde{z}(t) = \sum_{k=1}^{NZ} b_k(t) q_k \qquad \text{(2.3-22b)}$$

The time series $a_k(t)$ and $b_k(t)$ are called the left and right expansion coefficients and the vectors are p_k and q_k the corresponding spatial patterns. It can be shown that if p_k and q_k are the *k*-th left and right singular vectors of the covariance matrix C_{sz}, the covariance between the k-th left and right expansion coefficients, $< a_k b_k >$, is equal to the corresponding *k*-th singular value. The SVD expansion can be ordered such that the first mode corresponds to the largest singular value, and so on. The percentage of the covariance explained by the k-mode, the squared covariance fraction (SCF), is,

$$SCF_k = \frac{< a_k b_k >^2}{\|C\|^2} \qquad \text{(2.3-23)}$$

where the squared Frobenius matrix norm is the total amount of squared covariance summed over all entries in *C*:

$$\|C\|^2 = \sum_{i=1}^{NS}\sum_{j=1}^{NZ} C_{ij}^2 \quad . \qquad \text{(2.3-24)}$$

Obviously, $SCF_1 > SCF_2$, and the first mode extracts most of the spatial covariance (as defined by the Frobenius matrix norm).

3. Topographic Rossby Waves

This chapter is divided into two sections: the first concerns model investigations of TRW characteristics and dynamics that are based on Oey and Lee (2002), and the second is about the ability of the model to simulate the observed characteristics of the waves in various parts of the deep Gulf. The latter uses the deep current measurements listed in section 2.2.

3.1 Model Investigations

3.1.1 Introduction

Hamilton (1990) first gave observational evidence of TRW's in the Gulf of Mexico (GOM) through analysis of long-term current measurements below 1,000 m depth made in the late 1980's. Based on deep moorings over the slope and rise around the Gulf, east from Florida to northern and western Gulf, he found energy spectral peaks at 25, 45 and 100 days, within the range of periods expected for TRW's. The motions were characterized as columnar, with amplitudes decreasing with increasing height off the seabed. The waves are transverse and rectilinear such that the principal major axis is at an angle to the general trend of the isobaths. More detailed analyses showed that these waves have wavelengths of about 110-300 km, phase velocities that were offshore and energy propagation that were westward with speeds of approximately 9 km/day. More recent measurements (Hamilton and Lugo-Fernandez, 2001) made at the base of the slope (2,000 m), just south of the Mississippi delta at 90°W, showed high amplitude (~ 50 cm/s), short period (~10-12 days) period wave trains regularly passing through the site (Hamilton et al., 2003). These waves seem to originate on the west side of an extended LC and appear to be refracted back into deep water by the steep Sigsbee escarpment, since they are not observed further west in the basin. These short period waves are not likely to be resolved by the model grid and most of the attention in this section is on waves with periods of 20 to 100 days.

The Loop Current (LC), with speeds that can exceed 2 m/s near the surface and O (10cm/s) at 1,000 m depths, constitutes a major forcing to flow fluctuations in the Gulf of Mexico. On time scales from weeks to years, the LC can extrude as far northward as the Alabama-Mississippi continental rise near the foot of the De Soto Canyon, and retract southward to near the Yucatan Channel (Vukovich et al., 1979). This LC pulsation is often accompanied, at periods that range from 6 to 20 months, by shedding of Loop Current Eddies (LCE) - energetic warm-core rings (similar to those found in the Gulf Stream system) with diameters which typically range from 200 to 300 km and near-surface swirling speeds that exceed 1.5 m/s (Kirwan et al., 1988; Forristall et al., 1992; Hamilton et al., 1999). In addition, through some kind of dynamical instability, or otherwise a cascade mechanism that is not yet fully understood, smaller-scale eddies (cyclones in particular) and frontal meanders are believed to be generated from the larger-scale LC and LCEs (Paluszkiewicz et al., 1983; Hamilton, 1990, 1992; Hamilton et al., 2000).

Given their ubiquitous signatures, it seems logical to hypothesize that, through some mechanisms, the Loop Current and LCE's force deep-flow eddy kinetic energy (EKE) and TRW's in the Gulf. While field evidence is hard to come by, (numerical) models of the Gulf, forced by time-independent forcing, suggest that this might in fact be the case (e.g. Oey, 1996).

Motivated by Hamilton's (1990) work, Oey attempted to identify TRW's from his calculation of the LC and LCEs in the Gulf. Similar to what Hamilton found, the calculations yielded columnar motions for depths deeper than 1,500m at locations over the slope and rise around the Gulf, along-isobath motions that intensified near the bottom, spectral peaks within the 20 to 100 day periods, and westward energy propagation with speeds of about 12 km/day. Because these model runs used steady forcing, these findings established a direct link between LC and LCE-induced variability and bottom EKE, though they fell short of establishing what that variability might be, and of proving that the deep motions were indeed TRW's. Moreover, it is of interest to study, if TRW's do exist, what their paths are in the Gulf and whether or not (and how) they can account for EKE recorded (in the model and/or field experiments) at locations that seem distant from direct LC and LCE influences. These issues are addressed using an improved version of the primitive-equation (PE) model used by Oey (see section 2.1). It will be shown that, in a model forced by steady transport from the Caribbean Sea and Atlantic Ocean, the deep-flow EKE over certain parts of the slope and rise in the Gulf are TRW's, that these TRW's originate from regions beneath the LC and from locations coincident with the paths of propagating LCE's, and that the link between the energy of the large-scale, i.e. those of the LC and LCE's, and the near-bottom energy is surface high-frequency, short-wavelength disturbances produced around the LC and LCE's.

3.1.2 Setup of the Model for Deep Flow Experiments

The model, described in section 2.1, is initialized with an ocean at rest, and run in diagnostic mode for one month, during which the density field (ρ) is fixed at its annual-mean distribution. A (predominantly) geostrophically-adjusted velocity field is established during this time. The prognostic calculation is then initiated from this balanced field and a quasi-equilibrium state, in which regular, nearly-periodic LCE shedding occurred, is established in about 2 years. The integration is then continued through the tenth year. Figure 3.1-1a gives snapshot examples (every 90 days) of contours of ζ/f (relative vorticity divided by local Coriolis parameter) at $z=-50$ m, showing LCE shedding and westward propagation. Figure 3.1-1b plots time/latitude contours of free-surface elevation η along 90^oW, showing passages of LCEs when η maximizes to ~ 0.3 m. Various characteristics of the LC and LCEs are as follows. The shedding period is very nearly constant at 10 months (Figure 3.1-1b) and LCE diameters are about 300 km. Once shed, modeled eddies traverse across the Gulf in a southwestward direction at speeds of approximately 4 to 5 km day^{-1}, and decay eventually in the southwestern corner of the Gulf. In this constant-inflow experiment, the basic shedding mechanics and eddy kinematics follow closely those described in Hurlburt and Thompson (1980) (c.f. Sturges et al., 1993; Oey, 1996). Typical swirl speeds and ς/f around an eddy are 1.2 m s^{-1} and -0.4, respectively, while the corresponding values at the western edge of the LC in the Yucatan Channel are 1.5 m s^{-1} and 0.7. The maximum swirl speeds are weaker than those typically observed, about 1.5 to 2 m s^{-1} (Kirwan et al., 1988; Forristall et al., 1992). The resulting weaker forcing will likely result also in a weaker deep response. This should not however, seriously jeopardize our attempt to diagnose and study TRW's, which basically are linear waves. On the other hand, the maximum modeled swirl speeds represent improvements over those found in Oey (1996), which gives

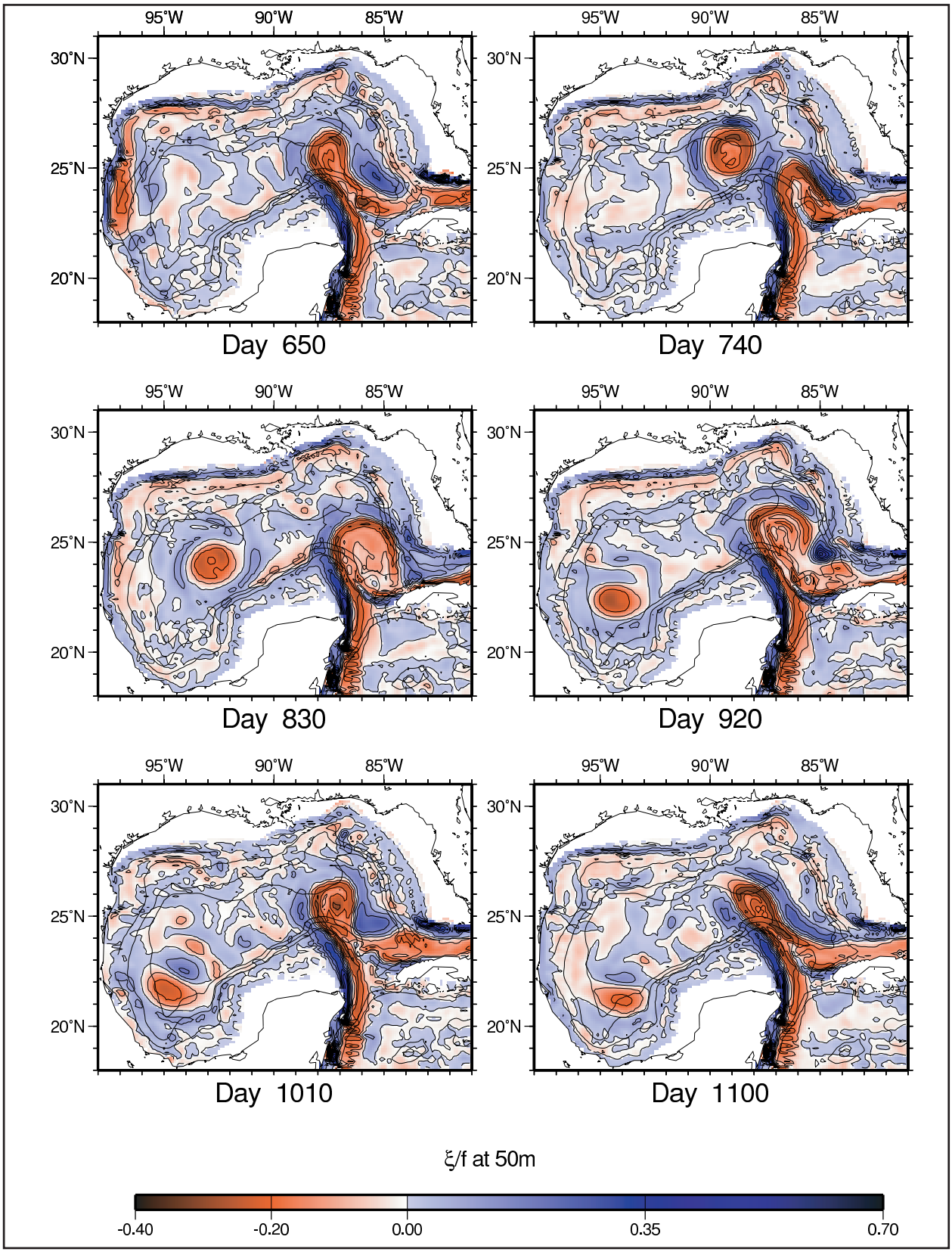

Figure 3.1-1a Ninety-day snapshots of relative vorticity (ζ/f; 5-day averaged) at z=-50 m showing LCE shedding, southwestward propagation, and decay.

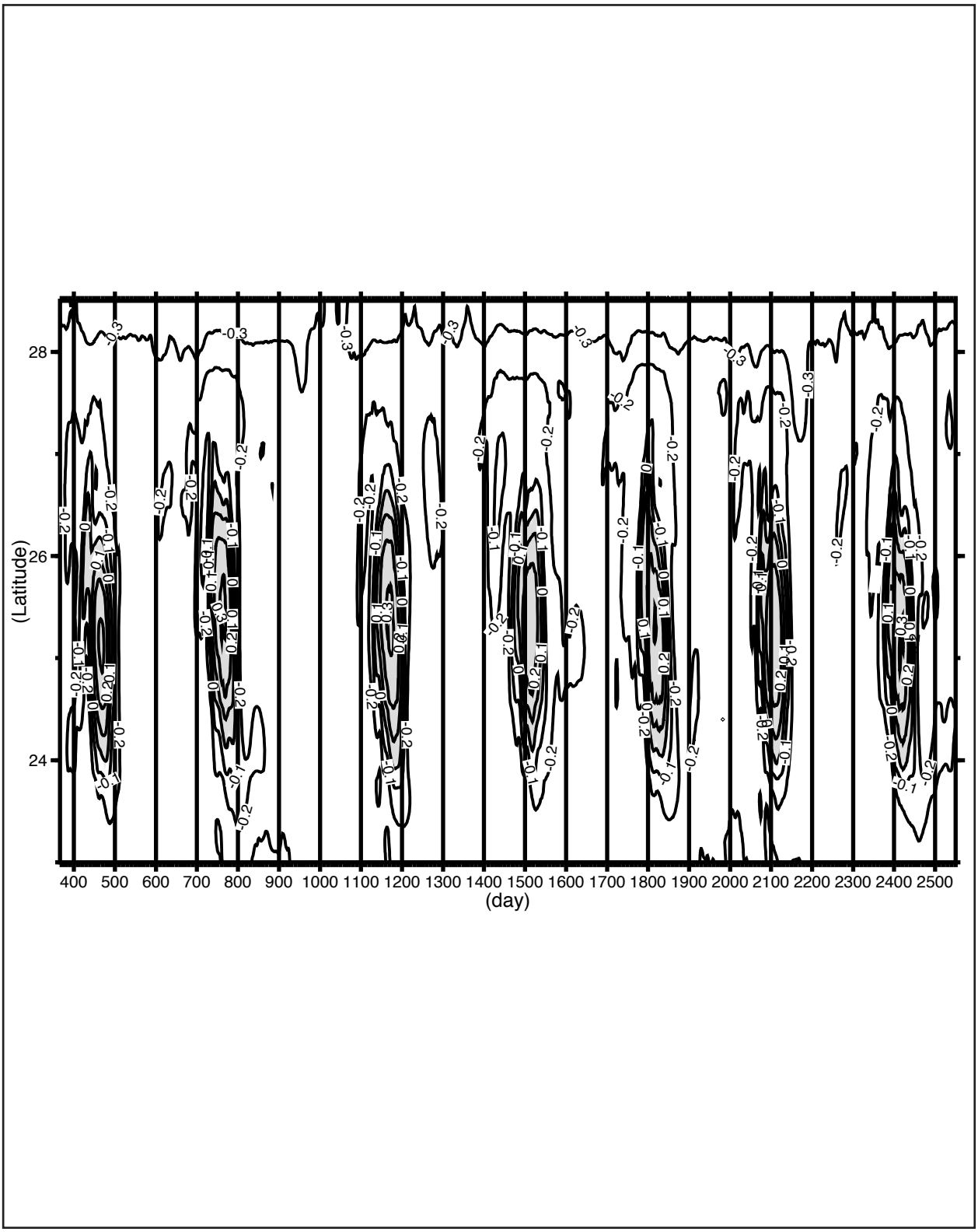

Figure 3.1-1b Time/Latitude contours of free-surface elevation η along 90°W, showing passages of Loop Current Eddies when η maximizes to ~ 0.3 m. Regions where $\eta > 0$ are shaded.

values of 0.76 m s^{-1} ($\varsigma/f \approx -0.25$). Because the forcings are similar in the two calculations, the improvements are a result of increased grid resolution (doubled) in the present case (c.f. Oey, 1998).

While the near-periodic shedding and constancy of direction of LCE propagation are idealized settings not found in the real ocean, they represent dynamically consistent forcing for (deep) flow EKE in the Gulf. By understanding how TRW's develop in this simplified system, we hope to develop hypotheses and ideas for future analyses of more realistic models, and of observations as well.

3.1.3 Model Data Processing

For the purpose of identifying TRW's in the PE model, it is useful to divide the model's results into four isopycnal layers, with layer 1 from surface to $27\sigma_t$ (~300 m thick), layer 2 from $27\sigma_t$ to $27.5\sigma_t$ (~ 500 m thick), layer 3 from $27.5\sigma_t$ to $27.7\sigma_t$ (~ 500 m thick), and layer 4 from $27.7\sigma_t$ to bottom (thickness ≈ 1,000 m or more). Figure 3.1-2 shows an example of this division at 90°W. Because TRW motions are columnar (vertically coherent) at depths below about 1,000 to 1,500 m, EKE is examined in the fourth layer, i.e. below the $27.7\sigma_t$ surface (note that this lies approximately 1,000 to 1,500 m below the free surface). The modeled currents are daily means, which are then depth-averaged in each layer. The depth averaging in the fourth layer precludes possible biases of high EKE that might occur in some region if a fixed z-level were used to search for TRW's. It has the added nicety of also eliminating any grid-point noise. On the other hand, the depth-averaging *reduces* by at least 50% the values of the near-bottom kinetic energy. The last 7 years of the 10-year run were then spectrally analyzed, and the results in the 20 to 100 day, TRW band examined.

3.1.4 Deep Flow Eddy Kinetic Energy

The model regions, where TRW's are active in the Gulf, are determined in this section. To do this we first search for areas where a significant (60%) part of the total energy falls in the TRW period range of 20-100 days, where the deep energy is above a certain threshold, and where bottom intensification exists. These regions are then checked so that the topographic slopes and stratification are such that the 20 to 100-day TRW's can be supported. The spatial correlations are then calculated so as to examine, in an *ad hoc* way, wave propagation in these regions of significant deep energy. The TRW dispersion equation (2.3-1) is utilized and the ray equations (2.3-4) and (2.3-5) (or (2.3-8) and (2.3-9) when deep mean currents are included) are integrated to show that rays originate in the LC and LCE's, and are confined in these significant deep energy regions.

Figure 3.1-3 compares the time series of lower-layer (i.e. layer 4) kinetic energy fluctuations (LOKE) at a station just west of the LC (88°W, 25.8°N) with the corresponding 20-100 day band-passed LOKE (henceforth referred to as $\text{LOKE}_{\text{20-100d}}$). At this station the amplitude and phase of the band-passed series generally follow those of the total series. The ratio of their standard deviations, $\text{LOKE}_{\text{20-100d}}/\text{LOKE}$ (note that here the same notation 'LOKE' is used for standard deviation) ≈ 0.68. Observations of deep currents show that, where TRW's are observed

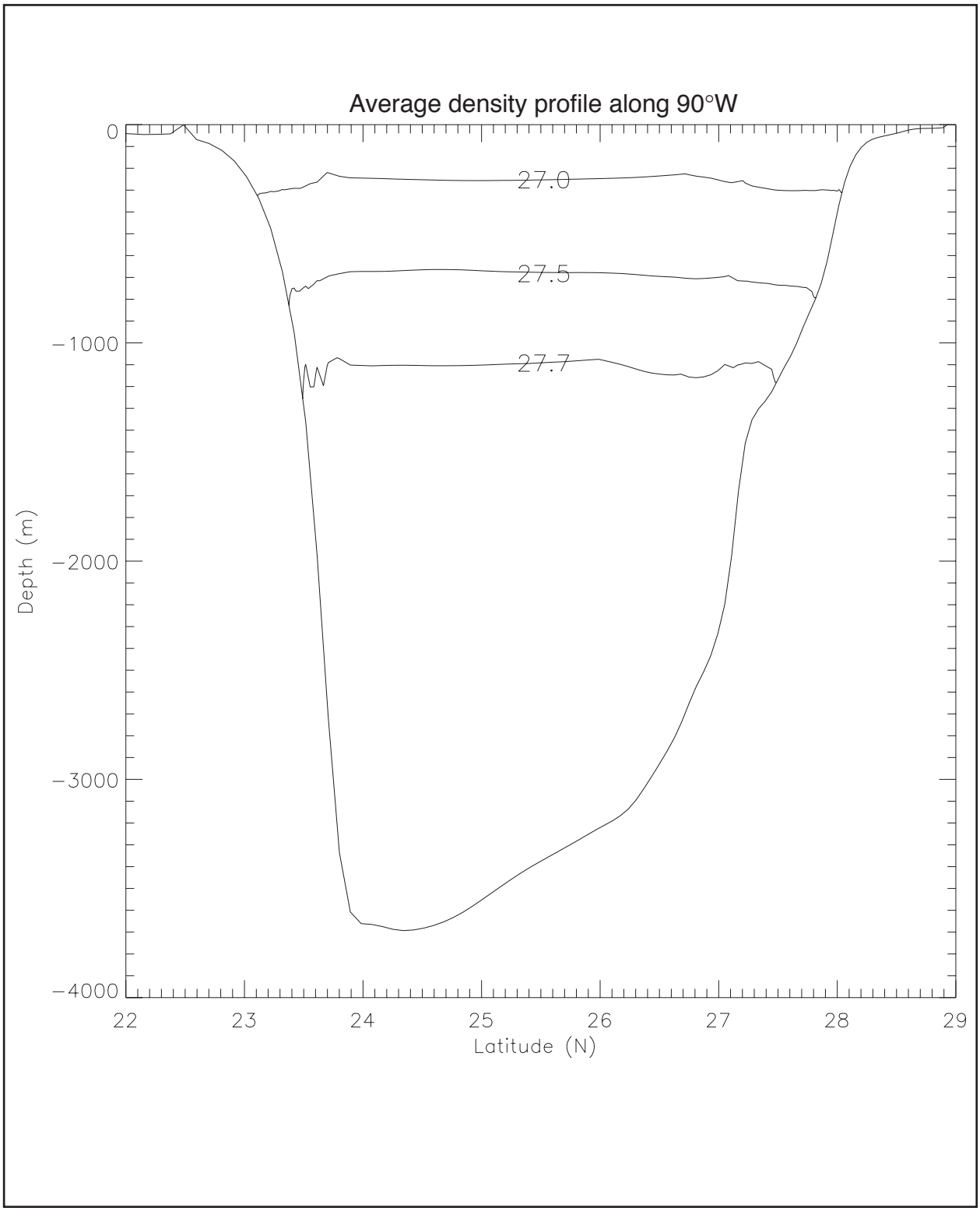

Figure 3.1-2. A time-averaged cross-sectional contour plot of density at 90°W that describes isopycnal division of model's three-dimensional field into four layers: layer-1 from surface to $27\sigma_t$, layer-2 from $27\sigma_t$ to $27.5\sigma_t$, layer-3 from $27.5\sigma_t$ to $27.7\sigma_t$, and layer-4 from $27.7\sigma_t$ to bottom.

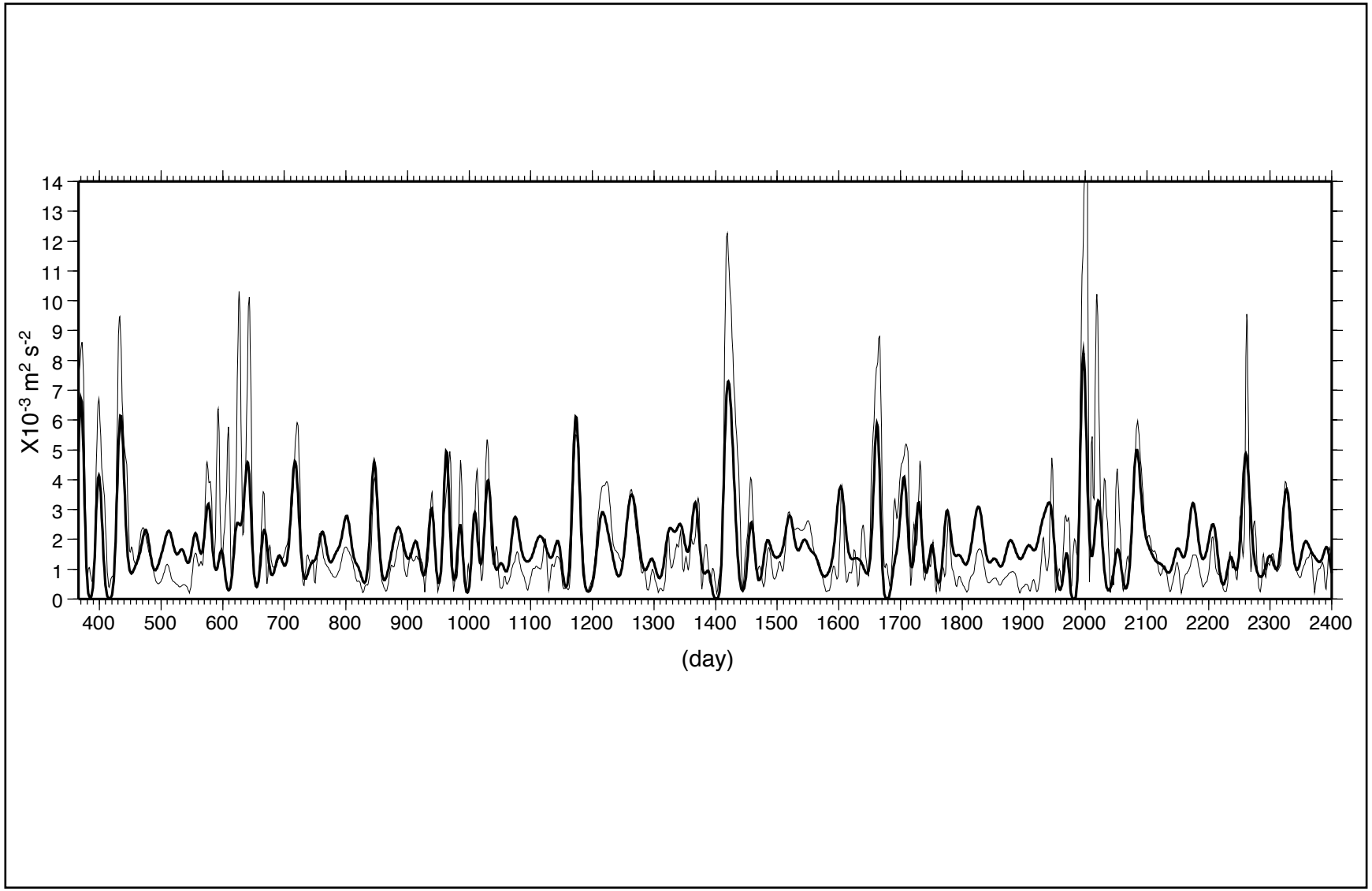

Figure 3.1-3 A comparison of the time series of lower-layer (layer #4) kinetic energy (LOKE; thin curve) at a station just west of the LC (88°W, 25.8°N) with the corresponding 20 to 100-day band-passed LOKE ($LOKE_{20\text{-}100d}$, thick curve).

over the continental slope of the Gulf, they generally account for some 95% of the total near-bottom EKE. In the present case in which the energy is averaged over the lower layer (thickness ~ 1,000 to 2,000 m assumed > TRW trapping scales; see below), the appropriate percent-value, assuming TRW exponential decay with height above the bottom (from a maximum of 95% at bottom), is $\approx (1 - e^{-1}) \times 0.95 \approx 60\%$. Thus Figure 3.1-3 suggests that, at least at this location, TRW's *may* exist. Therefore, only those regions where LOKE $_{20\text{-}100d}$/LOKE > 60% are considered. To avoid regions where the ratio is artificially inflated, a second, minimum-LOKE constraint is imposed such that the local LOKE exceeds 10^{-3} m^2 s^{-2}, the Gulfwide-averaged standard deviation of LOKE. A third constraint is also imposed such that only those regions where the kinetic energy shows intensification near the bottom (Hamilton, 1990) are considered. These constraints are probably over-restrictive in that they will likely eliminate potential sites (for TRW activities) where both TRW and strong locally-forced, non-TRW components of the EKE coexist, under the LC for example. Thus, while the minimum-LOKE constraint is satisfied, the ratio and bottom-intensification requirements may not be. On the other hand, the constraints ensure that what survive are robust features of the model that may have better chance of being observed in the real ocean.

Figure 3.1-4 gives LOKE $_{20\text{-}100d}$ after the above three constraints are imposed. It shows a significant LOKE $_{20\text{-}100d}$ region across the Gulf over approximately the 3,000-m isobath. This along-3,000 m-isobath band of LOKE $_{20\text{-}100d}$ will be refered to it as the "CGKE," or "central-Gulf LOKE $_{20\text{-}100d}$" band, and will be the focus of the investigations. While there are other significant LOKE $_{20\text{-}100d}$ regions in the model Gulf (e.g. 88°W, 28°N; Figure 3.1-4), the central-Gulf band suggests a *simpler* cause-and-effect scenario: i.e. forcing under the LC and southwestward propagating LCE's, and near-bottom energy that spreads westward. It is noted that the CGKE band not only indicates regions where LOKE $_{20\text{-}100d}$/LOKE > 60%, it also coincides well with areas where bottom intensification exists in the model Gulf. In other words, the extent and shape of the band in Figure 3.1-4 are essentially unchanged if only the bottom-intensification and minimum-LOKE constraints are imposed.

The CGKE band is now checked that it resides in a region where TRW's can be supported. Equation (2.3-2) is used to plot contours of the minimum period $P=2\pi/\sigma \leq \tanh(NhK/f)/(N|\nabla h|)$. Figure 3.1-5 shows P for $2\pi/K=110$ km, and using N(x,y) derived from the model as explained below. Except for the relatively gentle topography of the deep central Gulf where only long-period (>100 days) TRW's can be supported, waves of shorter periods can in theory exist almost anywhere in the Gulf. It is therefore, not immediately apparent why LOKE $_{20\text{-}100d}$ is confined only along the narrow band over approximately the 3,000-m isobath in Figure 3.1-4. In other words, why is there not a more expansive north/south spread of energy that exhibits TRW characteristics to other regions of the Gulf? The answer lies in the way that TRW energy is refracted. In the following, two methods are used to attempt the linking of the CGKE band with TRW's: firstly a somewhat ad-hoc phase and correlation analysis, and secondly a more precise ray (energy) tracing calculation. Based on these calculations, possible sources of these near-bottom EKE are discussed.

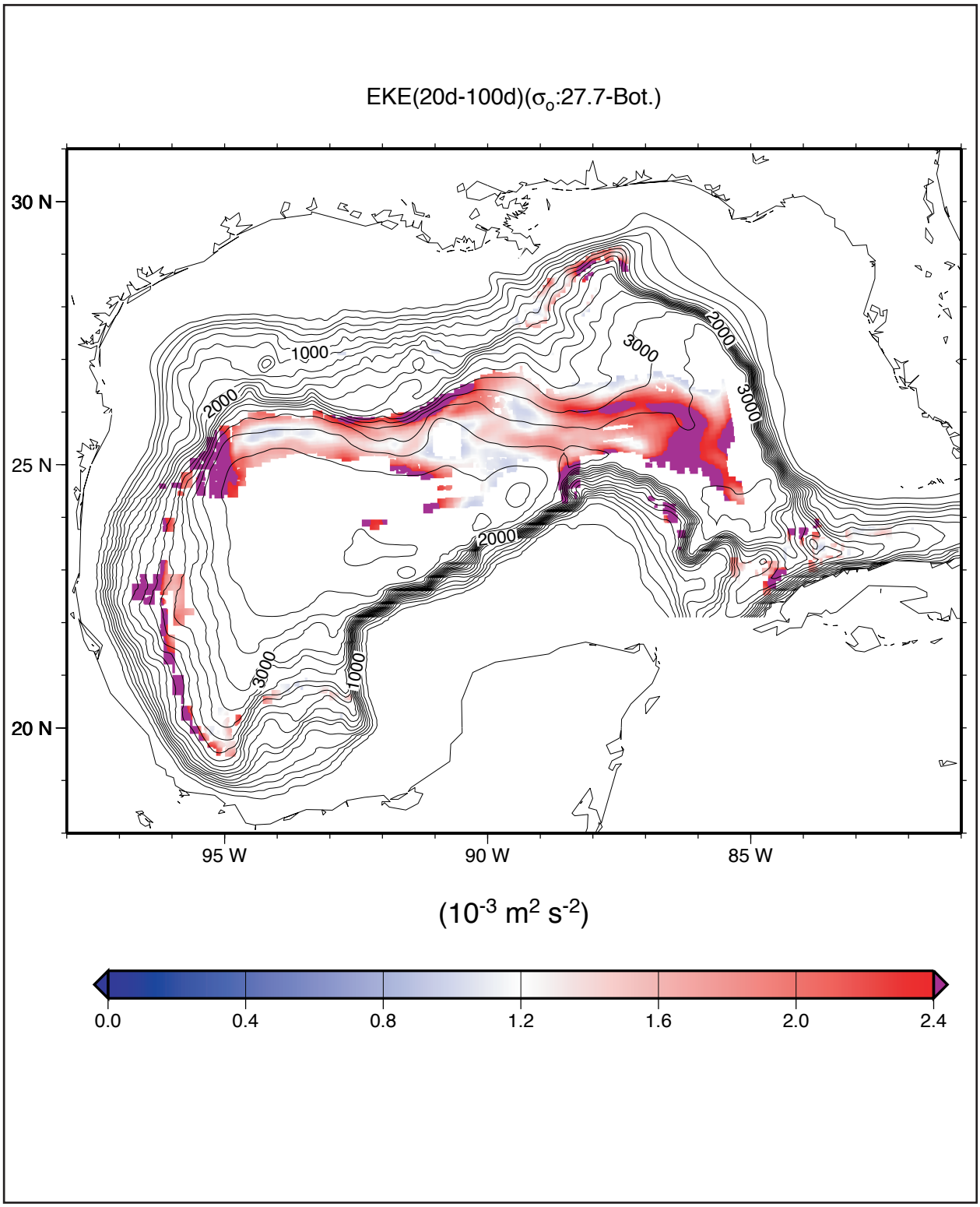

Figure 3.1-4. The lower-layer kinetic energy in the 20 to 100-day periods (LOKE $_{20\text{-}100d}$). Regions where the ratio of LOKE $_{20\text{-}100d}$ to total LOKE is less than 60%, where there is no bottom intensification, and where LOKE does not exceed the Gulfwide average of 10^{-3} m^2 s^{-2} are omitted as discussed in the text.

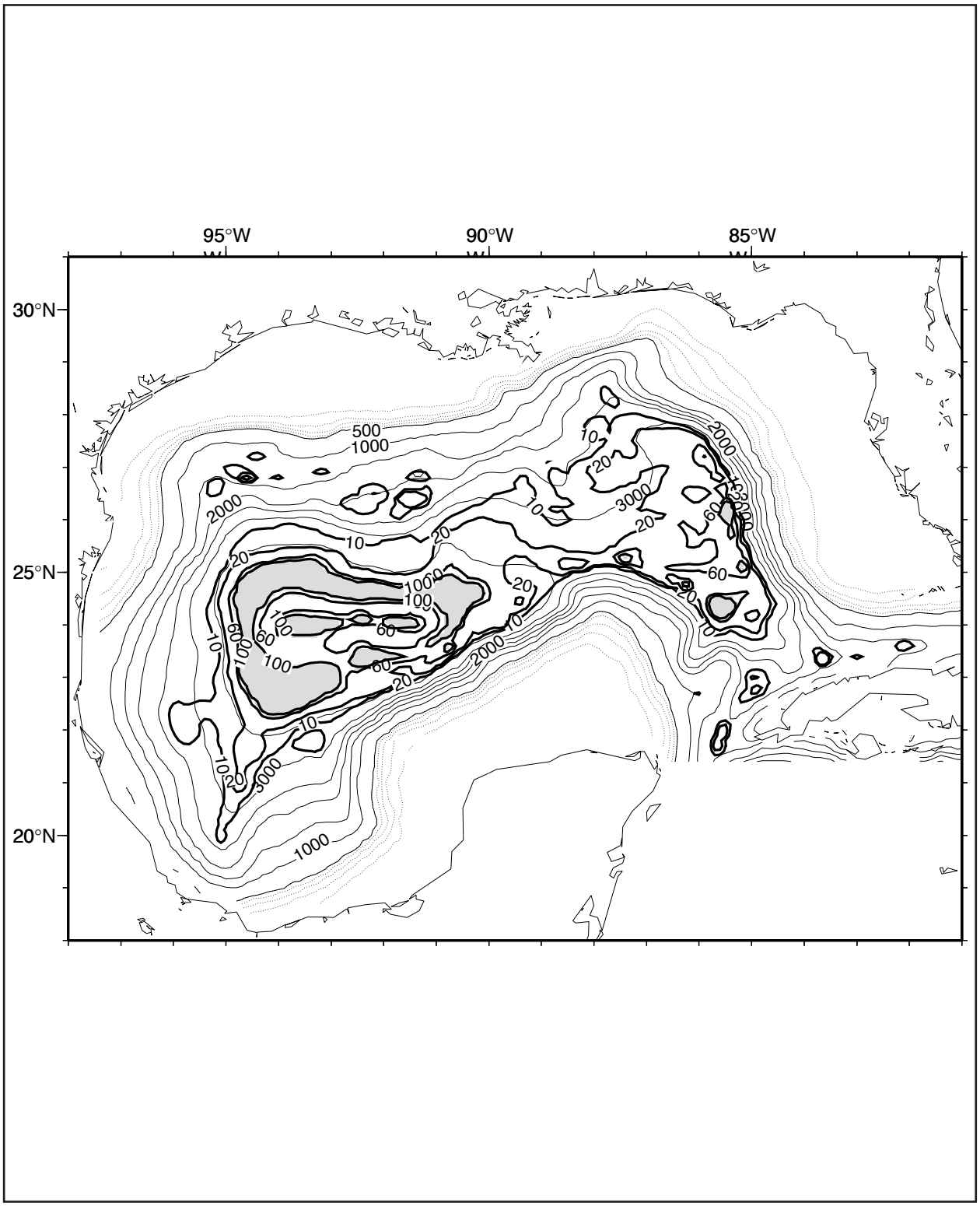

Figure 3.1-5 Contours of the minimum period (in days) $P=2\pi/\sigma \leq \tanh(NhK/f)/(N|\nabla h|)$ allowed by the TRW dispersion relation, for N given in Figure 2.3-2a and 2p/K=110 km. Regions that cannot support TRWs with periods shorter than 100 days are shaded.

Phase and Correlation Analysis

Time-lagged correlations were computed of the LOKE $_{20-100d}$ time series at 88°W, 25.8°N (e.g. Figure 3.1-3) with all other grid points, chosen because it is near the generation site of TRW's (see below). The top panel of Figure 3.1-6 shows contours of the lagged correlation (which differ from zero at the 95% confidence level) in the CGKE region, from 86°W to 92°W, and the lower panel, the lags in days. These calculations show that the CGKE band coincides with region of significant correlation, with fair values = 0.45 at approximately 92.2°W, 25.8°N, a distance some 400 km west of the 'X' point (the 95% significance level is ≈ 0.15 at this western point). In the vicinity of the 'X' point, the time-lag contours suggest a *phase* propagation from northeast to southwest. Strictly speaking, time-lag contours and phase lines are equivalent only for monochromatic waves, however, TRW spectra are often dominated by a single peak (Hamilton, 1990). Since the isobaths are approximately east/west in this region, the southwestward phase propagation is consistent with a southwest-directed or down-slope wavenumber vector, hence northwest-directed or up-slope group velocity that one would deduce from the TRW dispersion relation (see Section 2.3 and Figure 2.3-1).

Ray-Tracing Calculations

The approximate coincidence of the region of significant correlation with the CGKE band suggests a 'channeling' effect of near-bottom energy over the 3,000-m isobath, perhaps related to refraction of TRW's. To study this, wave rays were traced using the QG dispersion relation (Section 2.3). In addition to yielding information on various wave properties along the paths, the calculations also helped locate sources of TRW's. In the Gulf Stream region, the ray-tracing method has been used by Pickart (1995) to identify TRW's and TRW sources.

Initial Positions and Wavenumber Vectors of the Rays

To integrate equations (2.3-4) and (2.3-5) (or (2.3-8) and (2.3-9) if mean flows are included), initial position (x_o, y_o) and wavenumber vector (k_o, l_o), as well as the frequency σ defined for each ray, must be assigned. By integrating the equations backward (inverse ray-tracing; Pickart, 1995) from positions in the CGKE band, test calculations with various (k_o, l_o) (at period = 64 days, $-0.125 < l_o < -0.03$ km^{-1} and $|k_o| << |l_o|$, where here the direction of l_o is opposite to that of the local ∇h; thus hodograph ellipses are predominantly aligned with the local isobaths, Hamilton (1990)) satisfying the dispersion equation indicate that rays consistently trace back to locations under the LC and around the northern edges of the southwestward propagating LCE's. These tests suggest that LC and LCE variability are the prime driver of the lower-layer fluctuations found in the PE model. With these tests serving as a rough guidance, six initial positions, (x_o, y_o), shown as '+' in Figure 3.1-7a, are chosen, and the ray equations are then integrated *forward* with a set of (k_o, l_o) determined from the PE model outputs as follows. For convenience, the stations and corresponding rays will be referred to consecutively from east to west as station/ray #1 through station/ray #6.

In the vicinity of each initial position, energy spectra at a cluster of 'n' stations (n=10, including (x_o, y_o) was used), hence their phases at each frequency, are computed. Any three stations then give at least two linearly independent equations for the two unknowns *k* and *l*. The set of *k* and *l*

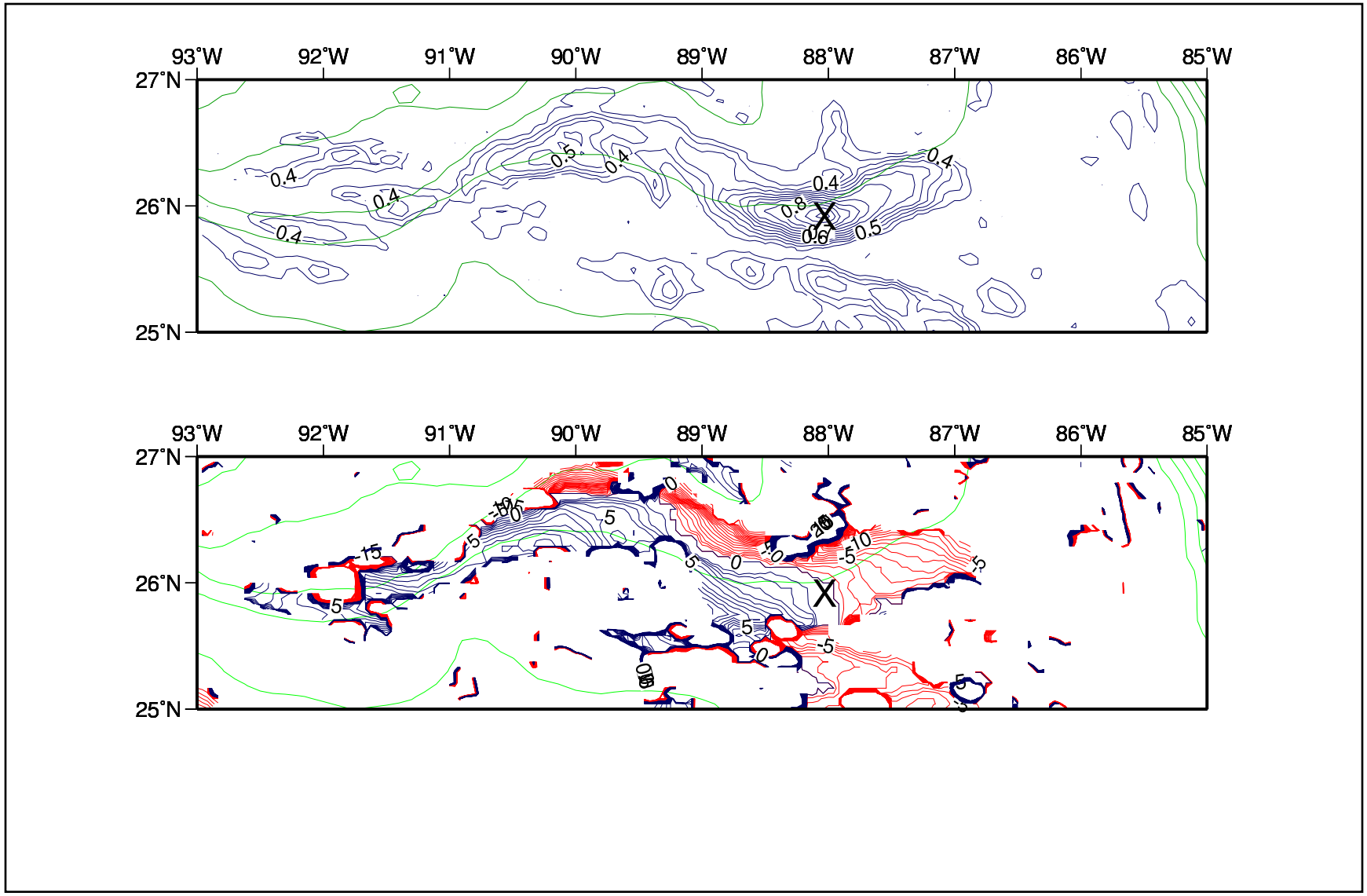

Figure 3.1-6. Top panel: contours of maximum lagged correlation (at 95% significance level) in the vicinity of the 3000 m isobath (CI=500 m), CGKE band (see text), from 86°W to 92°W. Lower panel: the corresponding lags in days.

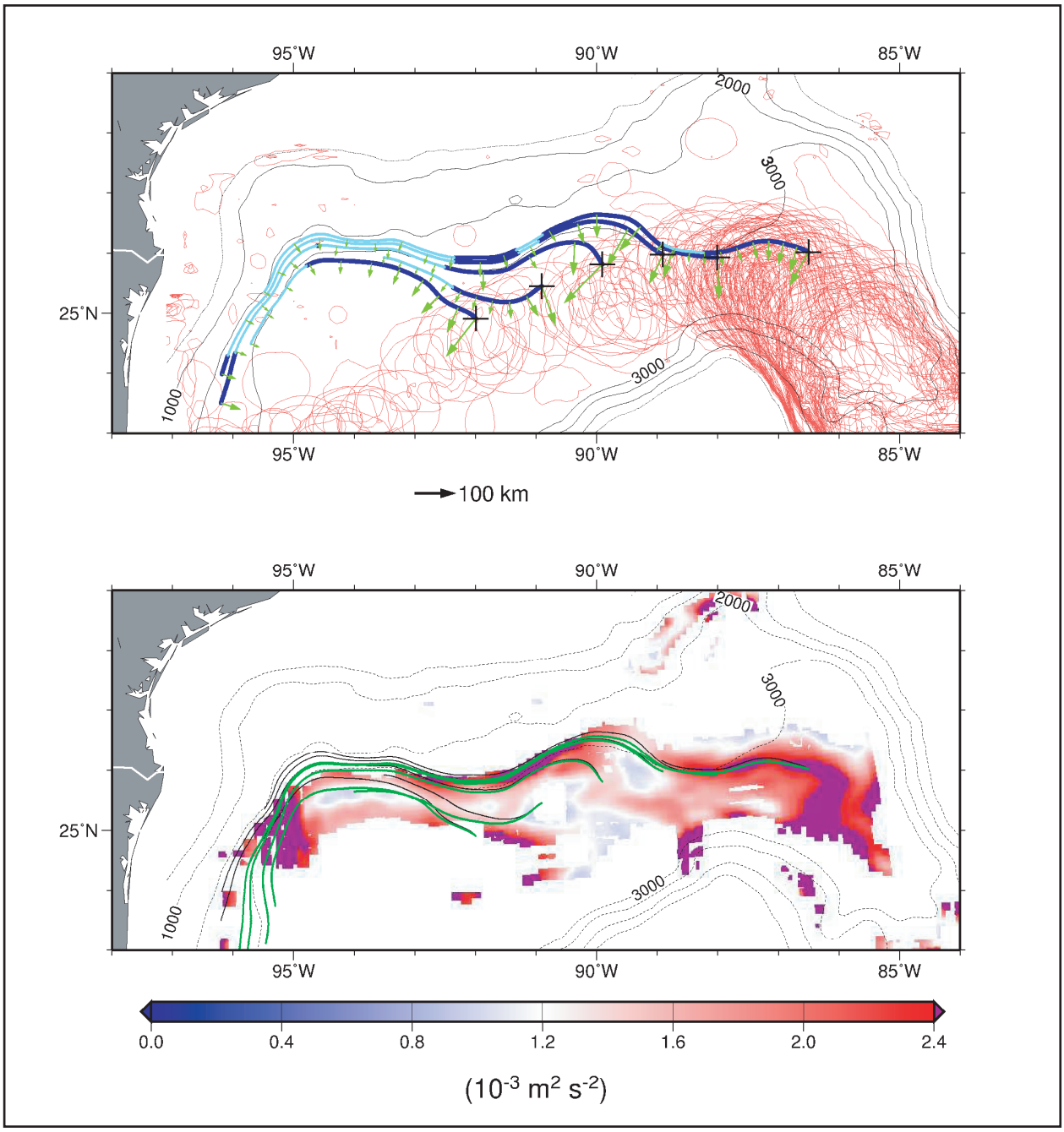

Figure 3.1-7a. Top panel: wave rays (in blue; lighter blue for wavelength < 30 km) traced using the TRW dispersion relation indicating deep energy paths in the Gulf that originate under the Loop Current and Loop Current Eddies. The outer rims of LC and LCEs are indicated in red by the 10-year assemblage of the ζ/f=-0.2 contours at z=-50 m obtained from the PE model. The green arrows indicate wavenumber vectors, plotted every 10 days along the path, with lengths equal to wavelengths (the 100 km scale is shown below the panel). Bottom panel: the 20 to100-day deep energy from Figure 3.1-4. Superimposed is a comparison of rays from the top panel (thin solid) with those derived by including effects of deep mean flow (thick green curves; using equations (2.3-8) and (2.3-9)).

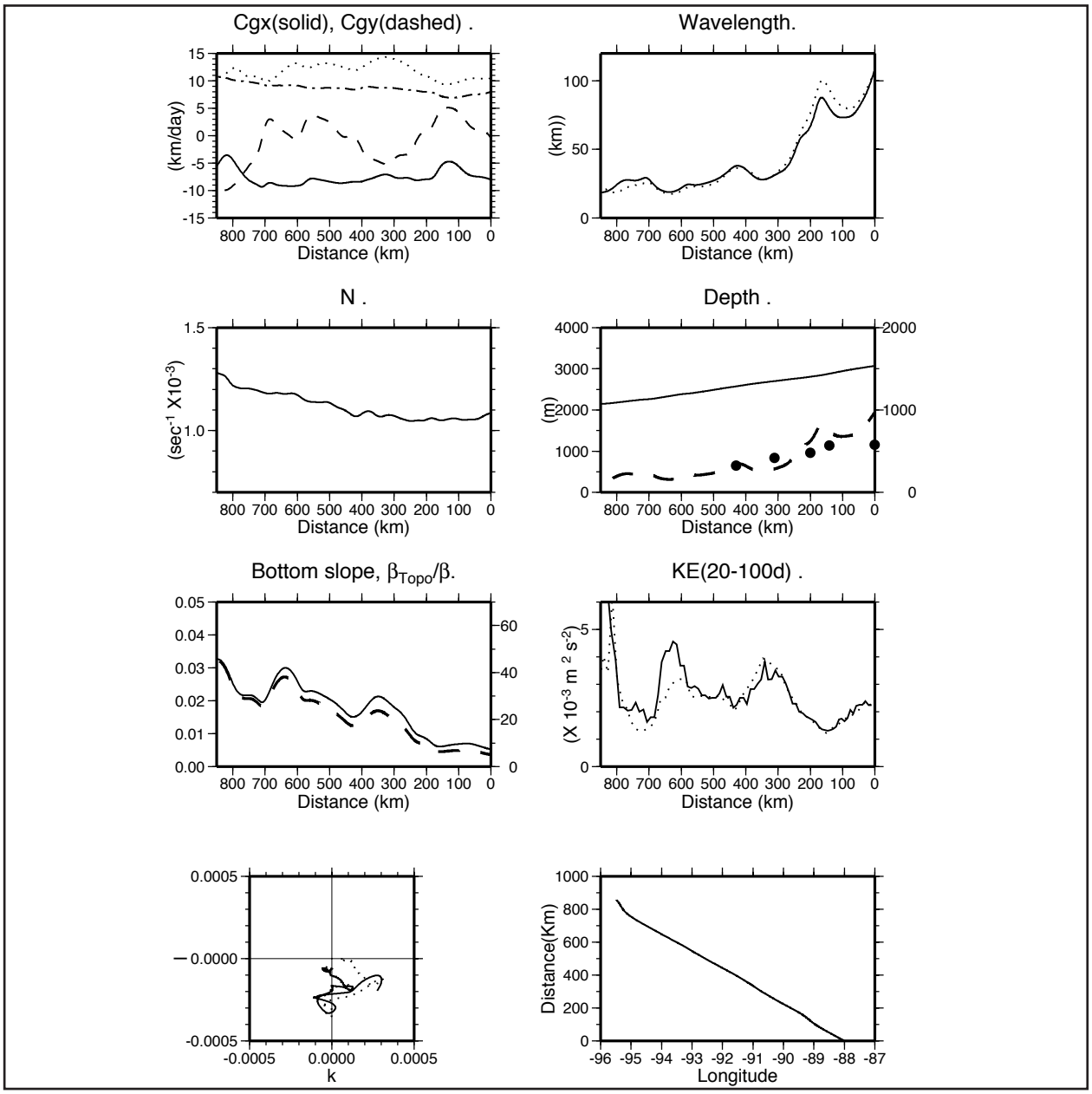

Figure 3.1-7b. Various TRW and ambient properties along ray #2 of Figure 3.1-7a: Top to bottom left-side panels: 1) east/west (solid) and north/south (dashed) group velocity components, and corresponding speed (dash-dot); 2) Brunt-Väisälä frequency; 3) topographic gradient (solid; left y-axis) and ratio of topographic to planetary beta, $\beta_{Topo}/\beta = fl\nabla hl/(h\beta)$ (dash; right y-axis); and 4) wavenumber vector (k,l) variation. Top to bottom right-side panels: 1) wavelength; 2) water depth (solid; left y-axis), trapping scale (dash; right y-axis), and estimates from the numerical model results at five locations along ray #2 (full circles; see Figure 3.1-9); 3) lower-layer EKE in the 20 to 100-day periods; and 4) distance along the ray as a function of longitude. The dotted-curves show respective properties corresponding to the ray that includes effects of deep mean currents (group speed in the top-left panel).

thus solved from all (non-redundant) triad permutations are then averaged. Figure 3.1-8 shows an example, at Station 2 (see Figure 3.1-7a), of four such solutions plotted on the dispersion curves for four frequencies. The frequencies were chosen to correspond to spectral peaks at this and its surrounding nine stations, at periods ≈ 32, 42.7, 51.2 and 64 days (c.f. Oey, 1996). The results at other stations are similar. The wavelength values range from 63 to 210 km and they are averaged for each period. Figure 3.1-8 shows that the averaged solution (k_o, l_o) pairs correspond to wavelengths $2\pi/K \approx 85$ to 150 km for the four selected periods. Moreover, they reside within the linear portion of the dispersion curves, i.e., they approximately satisfy equation (2.3-2) with $\beta \approx 0$ and when $\tanh(NhK/f) \approx$ constant. Thus, for each frequency, only the ratio k_o/l_o (i.e. the angle θ) is relevant. While group speeds increase with increasing wavelengths (equation (2.3-3)), ray-paths are relatively insensitive to wavelength (see below). In the following, $2\pi/K = 110$ km is used for the 'benchmark' calculation so that equation (2.3-2) then yields a first guess value of either k_o or l_o, and is used in an iterative process to solve (2.3-1) for more precise values of k_o and l_o. Hamilton (1990) estimates from observations (his Table 2) wavelengths from 110 km to 300 km for TRW periods from 18 to 300 days. Thus the wavelength values estimated from the PE model are on the lower end of the observed. However, more recent observations (Hamilton et al., 2003) with more closely spaced current meter arrays indicate wavelengths of ≈ 60 to 150 km for shorter period TRW's. The sensitivity of the ray solution to larger wavelengths is evaluated below.

Results and Interpretations

In Figure 3.1-7a, an example of six rays emanating from initial stations marked '+' is shown superimposed on ten-year assemblage contours of $\zeta/f = -0.2$ at $z = -50$ m. This value of ζ/f is used as it indicates well the outer rim of the LC and LCE's. The contours show the predominantly southwestward propagation of LCE's from their initial birth-place in the LC. Each ray is integrated for 100 days, using a period of 64 days, and on each one, the wavenumber vector direction, with length proportional to its *wavelength*, is plotted at 10-day intervals. Rays at periods 32, 42.7 and 51.2 days (Figure 3.1-8) have also been tested and the results will be discussed later.

Rays 1 and 2 originate from under the region of active LC north-south pulsation and LCE shedding. At station #1, the topographic slope is weak, and $\beta_{Topo}/\beta = f|\nabla h|/(h\beta) < 1$. Waves that emanate from here are at first predominantly planetary, and propagate slowly (~ –3 km/day). It later converges with ray #2, which is detailed next.

At station #2, $\beta_{Topo}/\beta \approx 6$, and ray #2 follows closely the 3,000-m isobath, crosses over it, but remains just inshore of it as the ray continues to the western Gulf. Its path, together with that of ray #1, coincides closely with areas of significant LOKE $_{20\text{-}100d}$, from about 87°W through approximately 92°W (Figure 3.1-7a, lower panel). West of 92°W, the wavelength shortens to values < 30 km, which is too short to be resolved by the PE model (this portion of the ray is of lighter shade in Figure 3.1-7a, top panel). The lower panel of Figure 3.1-7a (see also Figure 3.1-4) also shows areas along the 3,000 m-isobath where LOKE $_{20\text{-}100d}$ attains local maxima near station #2 or the 'source,' and near 91°W, 94°W and 95°W where rays converge. The ray equations can be used to explain the 'channeling' effect (of LOKE $_{20\text{-}100d}$) over the 3,000 m-isobath, mentioned previously, and also why TRW wavelengths shorten westward. Specifically,

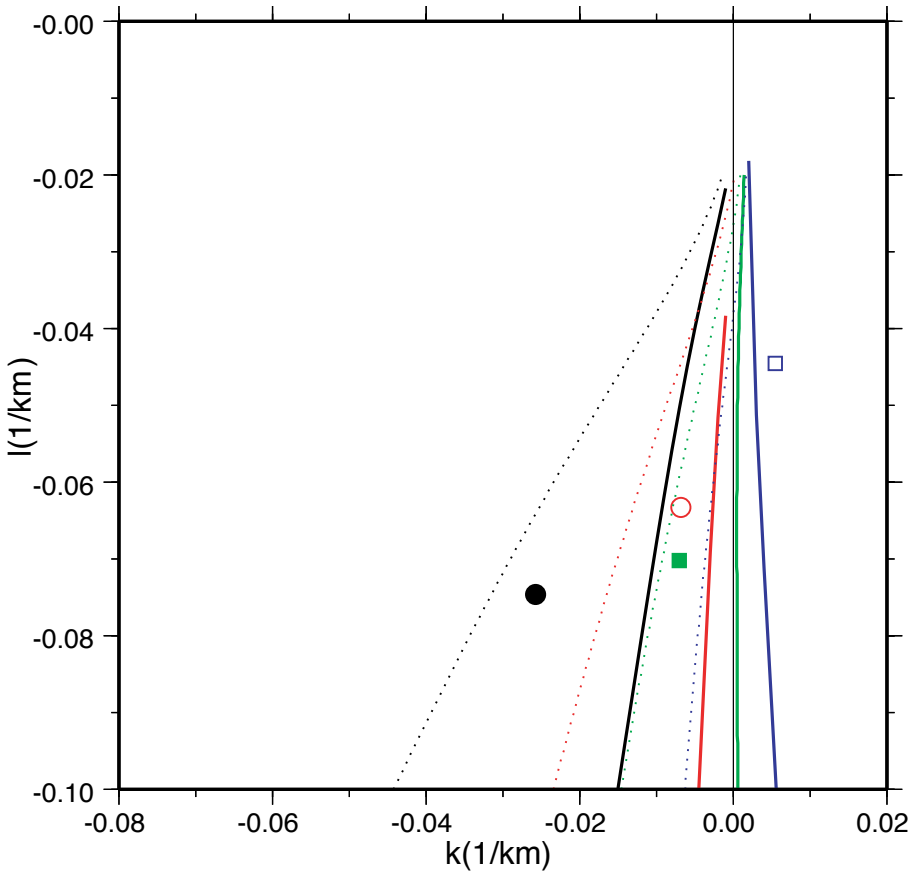

Figure 3.1-8. TRW dispersion curves corresponding to peak spectral periods of 32 days (left-most solid and dotted curves), 42.7 days, 51.2 days and 64 days. Solid and dotted curves are for $N=10^{-3}$ s^{-1} and 6.25×10^{-4} s^{-1}, respectively. The symbols denote averaged values derived from the numerical model results at station #2 of Figure 3.1-7a: filled circle for 32 days, open circle for 42.7 days, filled square for 51.2 days and an open square for 64 days

it can be explained why the ray must bend from propagating northwestward to southwestward at about 90°W, and why further west it stays inshore of the 3,000-m isobath, and does not veer northward to cross the 2,000 m isobath. Since β_{Topo}/β remains >> 1 (see Figure 3.1-7b and discussion of it below), equation (2.3-2) is an excellent approximation to the dispersion relation. Thus,

$$\sigma = N|\nabla h|\sin(\theta)/\tanh(NhK/|f|) \approx N|\nabla h|\sin(\theta), \qquad (3.1\text{-}1)$$

where θ is the clockwise angle the wavenumber vector makes with the direction of steepest topographic decent (i.e. with $\nabla h/|\nabla h|$; Figure 2.3-1). Also for $NhK/|f| \approx O(1)$ or larger, the 'tanh' is a weak function of 'NhK/|f|', and the first form of (3.1-1) is good with 'tanh' ≈ constant. Since σ is constant along a ray, $\sin(\theta)$, and hence θ (which remains in the first quadrant, i.e. $\theta < 90^o$), must decrease as the ray enters regions of steeper topographic slopes and/or stronger stratification. In other words, the wavenumber vector must become more *perpendicular* to, and the ray path (which points in the direction of the group velocity; see discussion in Section 2.3)) more *aligned* with, the local isobaths. Figure 2.3-2b shows that the topographic slope becomes steep between the 2,000 m and 3,000-m isobaths west of 90°W. This, coupled also with increasing (though slight) stratification to the north (Figure 2.3-2a), explains why the ray must turn from northwestward to southwestward around 90°W, and must be confined between the 2,000 and 3,000-m isobaths further west. The agreement of this 'channeling' or 'focusing' effect of the ray path and the CGKE band lends support to the idea that the latter is a manifestation of TRW's contained in the PE model.

It can be explained also how wavelengths are shortened by refraction as TRW's propagate northwestward into regions of increasing topographic slope and stratification. Multiply (2.3-5) by k_i and use (3.1-1):

$$d(k_i^2/2)/dt = -\,l\,\sin(\theta)\,\partial(|h_y|N)/\partial y, \qquad (3.1\text{-}2)$$

in which it is assumed for simplicity that contours of h and N are predominantly zonal. It is clear from Figures 2.3-2 that both $\partial|h_y|/\partial y$ and $\partial N/\partial y$ are positive inshore of the 3,000-m isobath and since l <0, $d(k_i^2/2)/dt$ >0 and TRW wavelength shortens along the ray. Hamilton (1990) also noted westward shortening of TRW's from observations.

Figure 3.1-7b gives various properties along the ray path #2. The magnitude of the group velocity (dotted curve in first left panel) varies from about 8 km/day at the initial location (station #2) to over 10 km/day as the ray turns southward along the Mexican/Texas slope, with an average of about 9 km day^{-1}. These values of the group speed are consistent with those reported by Hamilton (1990) and Oey (1996). The x-component (C_{gx}) is negative through the entire ray-path as wave energy propagates westward, while the y-component (C_{gy}) attains both positive and negative values as the ray undulates in accordance with the location of steep topographic gradient as explained above. This undulation is also reflected by the changing sign of the *x-component* of the wavenumber vector *k*, shown on the bottom left panel, since this is very nearly perpendicular to C_{gy}. The TRW is continuously being refracted along the ray-path and its wavelength shortens from an initial value of 110 km to 30 km (first right panel). In addition to Gulf processes (Hamilton 1990), Pickart (1995) also found wave-shortening over the

slope off Cape Hatteras. As noted above, topographic slope steepens (Figure 3.1-7b: third left panel – solid line) and topographic beta dominates on ray #2 as β_{Topo}/β increases to over 40 near the western Gulf (third left panel – dashed line). The solid curve in the second right panel indicates decreasing water depth along the ray, while the dotted curve shows the vertical trapping scale μ^{-1} of the wave. Along the ray, this is very nearly proportional to the wavelength, as can be seen by comparing the first and second right panels. This follows directly from the linear theory for which the vertical structure ~ $\cosh(\mu z) \approx \cosh(NKz/f)$ from (2.3-1a). The values vary from about 1,000 m at the beginning of the ray to 300 m some 300 km to the west. The trapping scales from the PE model profiles may be estimated in Figure 3.1-9. Here the vertical profiles of the square root of the 20 to 100-day kinetic energy at five locations from east ('A') to west ('E') are plotted along ray #2. Excluding the very near-bottom boundary layer (<50 m), where the energy is low, the profiles all show energy decay with height from the bottom, to a minimum that probably represents the combined effect of the upper-ocean energy decay (i.e. the first baroclinic mode) and TRW decay from below. Apart from this complication, one may assume an exponential decay from each profile's maximum to its minimum, and estimate the corresponding e-folding decay height. The solid-circle symbols in the second right panel of Figure 3.1-7b show the five estimated values. Though values differ, the PE model results also show westward decreasing trend of the trapping scales (from 600 to 300 m) in agreement with the TRW solution. Finally, the third right panel shows LOKE $_{20\text{-}100d}$, the accumulated energy of not only those TRW's that originate at station #2 and propagate along ray #2 at the 64-day period, but also those of other rays. It illustrates energy increases due to ray-focusing at the previously mentioned locations: 91°W, 94°W and 95°W. It is noted that these local maxima in LOKE $_{20\text{-}100d}$ coincide with minima in wavelength (first right panel), a feature consistent with the linear wave theory, where energy varies as the square of the wavenumber.

To get a sense of the bottom motions, Figure 3.1-10 shows examples of vector stick plots at locations 'A' and 'D' of Figure 3.1-9a, upward from the near-bottom depth level where the LOKE $_{20\text{-}100d}$ shows maximum (Figure 3.1-9b). The top panel shows vectors at a representative near-surface level. The up- or y-directed sticks in these plots denote motions parallel to local isobath, positive clockwise around the Gulf (i.e. generally eastward). Both locations show columnar (i.e. in-phase) structures that decay with height in the lower 1,000 m or so of the water column, and fluctuations in the 20 to 100-day periods can be seen. At location 'A', the motion appears to be uncorrelated with the near surface. Therefore, their relation, if any, cannot be seen in this plot of the whole motion (see, however, below), because LC and LCE fluctuations dominate the near-surface motions. At location 'D', away from the direct influence of the LC and LCE's, the near-bottom and near-surface motions are more correlated, yet the former over a height of about 1,000 m from the bottom is evidently more topographically controlled, i.e. more aligned with isobaths. Note that in the mean, near-surface currents at these and other locations are anticyclonic, while near-bottom currents are cyclonic around the Gulf (see Figure 2.3-3). To assess the effects of deep currents on ray properties, section 2.3 extends the ray equations (2.3-4) and (2.3-5) to include the ambient mean currents of Figure 2.3-3. One important effect is to change the velocity of the ray, equation (2.3-8), which in general increases the westward propagation speed. The green curves in the lower panel of Figure 3.1-7a show that with deep currents, rays #2 and #3 have looped around the western portion of the model Gulf. The averaged group speed increases from 9 to 12 km day^{-1} (Figure 3.1-7b, top left panel). The latter value agrees with Oey (1996), who also found (from correlation and time-lag

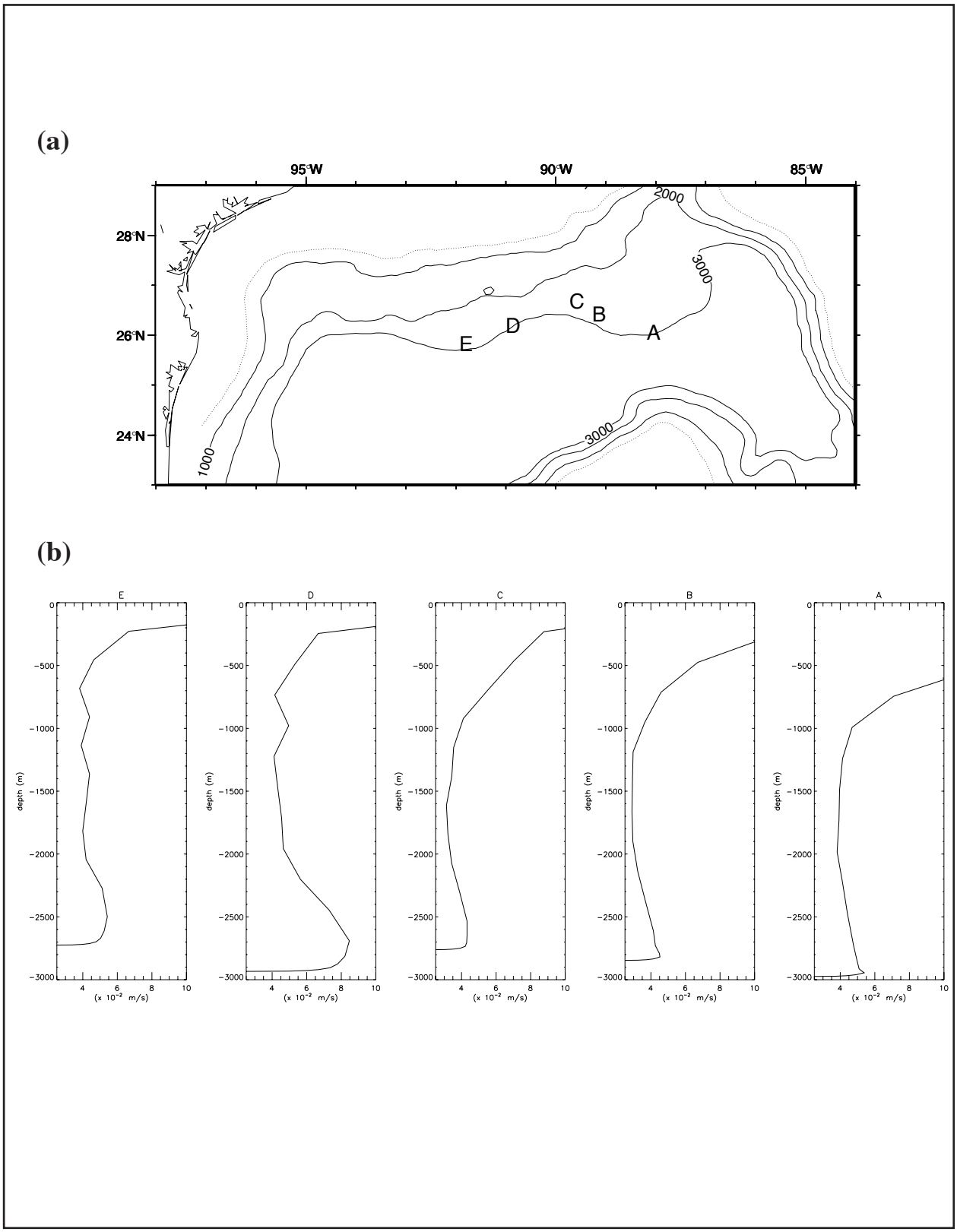

Figure 3.1-9. (a) Five locations along ray #2 (see Figure 3.1-7a) where vertical profiles of the square root of kinetic energy in the 20 to 100-day band are plotted (b).

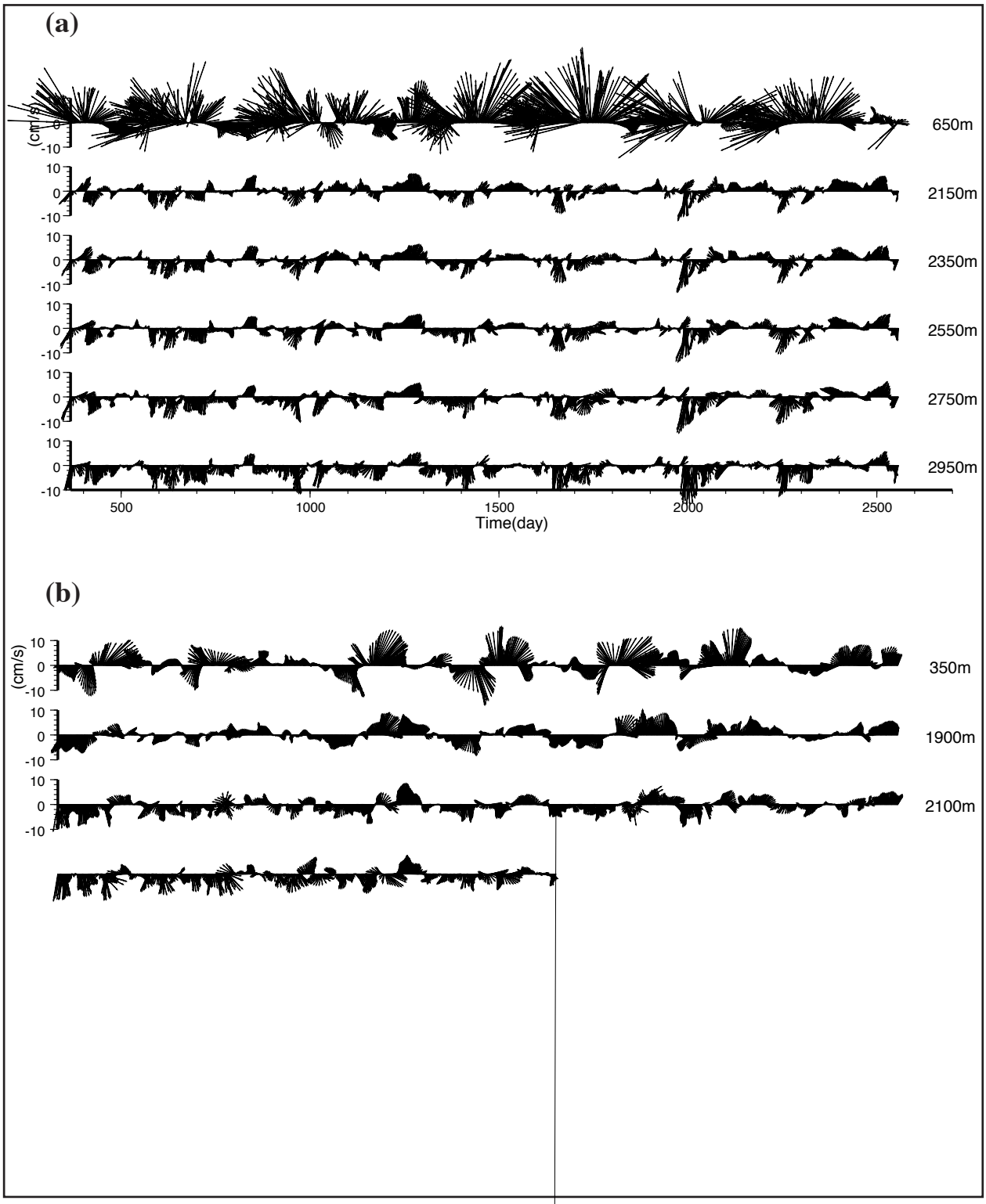

Figure 3.1-10. Vector stick plots at location ‘A’ (a) and 'D' (b) of Figure 3.1-9a, upward from the near-bottom depth level where the LOKE $_{20\text{-}100d}$ shows a maximum (bottom panel). The top panel shows vectors at a representative near-surface level. Up or y-directed sticks in these plots denote motions parallel to the local isobath, positive clockwise around the Gulf (i.e. generally eastward).

analysis) a value of 12 km day^{-1}. A less obvious effect is that current shears (and divergences) also diffract rays (Lighthill, 1978; see below) as can be seen from equation (2.3-9). These tend to 'bend' rays into the main CGKE region especially in the western Gulf, thus improving the overlapping of rays with areas of more significant LOKE $_{20\text{-}100d}$ obtained from the numerical simulation (Figure 3.1-7a, lower panel; see also Figure 3.1-7b where changes in ray properties of ray #2 are given).

Ray #3 originates from a location just outside the direct influence of the LC north/south pulsation, but affected by LCE sheddings and passages. Its path is similar to that of ray #2. It propagates upslope, and after crossing the 3,000-m isobath, converges with ray #2 westward from approximately the 90°W. It is concluded, therefore, that rays #1, 2 and 3 represent waves that originate from a region of active LC and LCE fluctuations. The paths traced by these rays coincide well with the eastern portion (~ from 86°W to 92°W) of the CGKE band. East of approximately 89°W, the band is likely a result of both locally forced (by LE and LCE's) and TRW components. West of 89°W, free TRW's are likely as the direct influence of LC and LCE's is almost nil.

Rays # 4, 5 and 6 were chosen to originate from the northern rims of propagating LCE's. Ray #4 first propagates northwestward, turns southwestward then westward to remain just offshore of the 3,000-m isobath before crossing it at approximately 92°W. Being initially over a relatively gently-sloping portion of the central Gulf, ray #4 starts off as a predominantly planetary Rossby wave (group velocity ~ −5 km day^{-1}), then quickly becomes TRW with its group speed increasing to ~10 km day^{-1}. Rays #5 and 6, and another ray further west (not shown), in part account for the moderate LOKE $_{20\text{-}100d}$ near the western Gulf (~93 to 94.5°W, 25°N). They exist as mixed topographic and planetary Rossby waves as β_{Topo}/β remains below 10 through most of their paths. Rays #4, 5 and 6 were also traced backward (from stations 4, 5 and 6). The results (not shown) indicate that they do not connect back to the LCE shedding zone in the eastern Gulf. This confirms that the energy along these rays originate from propagating LCE's in the central Gulf.

Depth-profile analysis similar to that conducted for ray #2, was performed for the other rays (c.f. Figures 3.1-9 and 3.1-10) and the near-bottom intensification of currents was confirmed. The wavenumber analysis (c.f. Figure 3.1-8), based on the PE model results, also confirms that the (k, l) pairs at locations on ray paths are consistent with the TRW dispersion curves. These, the phase and correlation analysis (Figure 3.1-6), and the coincidence of ray paths with the CGKE band (Figure 3.1-7), strongly support that TRW's exist in the PE model results. In summary, it is concluded that two types of TRW's can account for the CGKE band. The first is a predominantly topographic Rossby-wave type that originates under the region of active LC and LCE fluctuations in the eastern Gulf, and that tends to be 'channeled' between the 2,000 and 3,000-m isobaths. Though the CGKE band and rays extend into the western Gulf, it is cautioned that wave-shortening due to refraction means that the waves are under-resolved (~west of 92-93°W) with the present (PE) model's resolution. The second is a mixed topographic and planetary Rossby-wave type that originates from under LCE's that propagate southwestward over the deeper waters of the central Gulf. These waves account for LOKE $_{20\text{-}100d}$ found offshore of the 3,000-m isobath in the western Gulf.

Effects of Wavelength, Stratification, Periods and Deep Currents on Rays

It was mentioned previously that the averaged TRW wavelengths deduced from the simulation results are shorter than Hamilton's (1990) estimates from observations, but more consistent with later observations from the base of the slope at 90°W (Hamilton et al., 2003). Hamilton reported wavelengths from 110 to 300 km, while estimates from the numerical simulation range from 63 to 210 km. An average of 110 km was used as the initial condition for ray tracing. The rather wide range suggests that the WKB assumption of slowly varying (time and space) N (and other environmental variables) may not be strictly satisfied in the simulation results. It is also found that N varies depending on the depth-range used for averaging. Thus, $N \approx 2.5\times10^{-4}$ s^{-1} over the CGKE region if only the lowest 500 m is used. Figure 3.1-8 also plots, for each of the four periods, the dispersion curves corresponding to $N= 6.25\times10^{-4}$ s^{-1} (dotted curves), an average of the benchmark $N \approx 10^{-3}$ s^{-1} (approximately over the 3,000-m isobath) and $N = 2.5\times10^{-4}$ s^{-1}. Thus, the estimated (k_o, l_o) pairs are within the range of uncertainty in N. This uncertainty is also reflected in the value used by Hamilton, $N=5\times10^{-4}$ s^{-1}, an averaged value based on CTD casts for 1,500 to 3,000 m depth in the central Gulf. In view of the rather wide ranges in which both N and $2\pi/K$ can vary, it is of interest to examine how they affect the ray-paths.

The effects of **K**, N and σ on rays can be assessed from equations (2.3-3) and (3.1-1) (again assuming $\beta_{Topo}/\beta >> 1$ which is a good approximation). The former shows that $|\mathbf{C_g}| = N|\nabla h|/K$, so that group speed increases with wavelength but decreases with N. The ray path also depends on the direction of $\mathbf{C_g}$, or on the requirement that σ is constant (or σ_a=constant when $\mathbf{u}_{deep}$ is included, see Section 2.3) along the ray. For $NhK/|f| \approx 1$, the "tanh" term changes slowly for changes in its argument and can be assumed constant. Equation (3.1-1) shows then that for fixed N and σ, increasing the wavelength (from the 110 km used in Figure 3.1-7a) will merely increase the group speeds of the rays, otherwise the ray-paths are similar to those shown in Figure 3.1-7a (not shown). This insensitivity of the *ray-path* to wavelength has been found to be valid for $2\pi/K$ up to ~250 km. However, if N (and/or period) is decreased, the angle θ would increase and rays would tend to propagate more upslope than those shown in Figure 3.1-7a. Though the relation is nonlinear (equations 2.3-4 and 2.3-5), we find that these deductions based on (2.3-3) and (3.1-1) provide a fairly accurate picture of the effects of changes in wavelength, stratification and period on the ray path. In the top panel of Figure 3.1-11, two rays are plotted, starting from station #2, the original ray from Figure 3.1-7a with $N=10^{-3}$ s^{-1} and $2\pi/K$=110 km, and a more upslope ray for $N=6.25\times10^{-4}$ s^{-1} and $2\pi/K$=150 km (both rays are virtually unchanged when $2\pi/K$ is increased to, say, 250 km – when the time variable is scaled by ratio of the original K to new K to account for the corresponding increase in the group speed). Since only the ratio σ/N matters in equation (3.1-1), it is found that for $N = 10^{-3}$ s^{-1}, rays propagate upslope for $2\pi/\sigma \approx 43$ days or shorter, similar to the upslope ray of Figure 3.1-11. It appears, therefore, that the CGKE band seen in the simulation cannot be explained by shorter-period TRW's (<43 days) and/or TRW's at lower possible ranges of $N < 10^{-3}$ s^{-1}.

The situation is quite different when $\mathbf{u}_{deep}$ is included. The generally westward flow with cyclonic shear between the 1,000-2,000 m and 3,500 m isobaths (Figure 2.3-3), coupled with increasing $N|\nabla h|$, constitute sufficiently strong constraints for rays to bend down slope (see Section 2.3, equation (2.3-11)). Intuitively, rays are 'blown down wind' or westward. This is

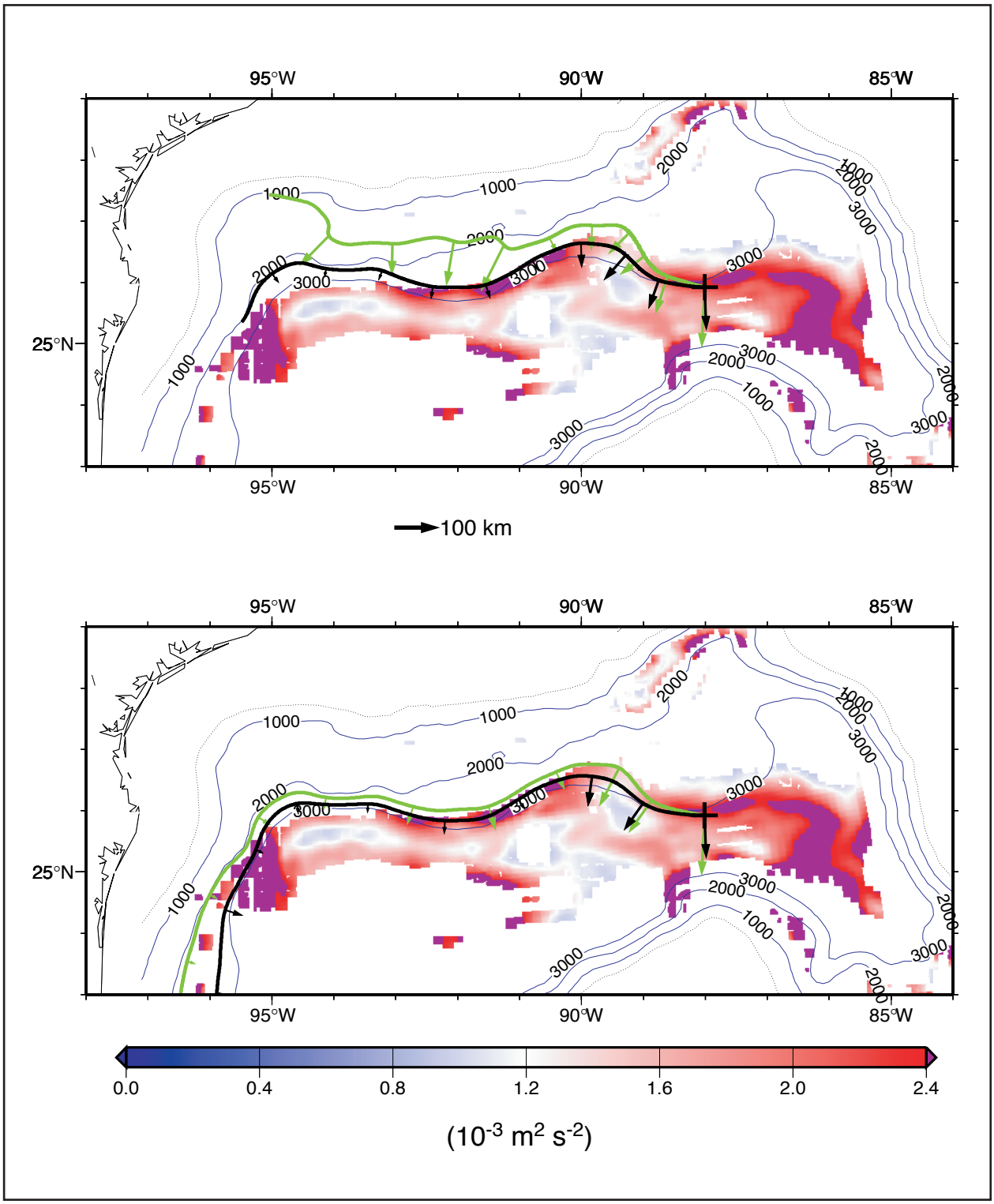

Figure 3.1-11. Sixty four-day period TRW rays traced from station #2 using the benchmark N-field of Figure 2.3-2 and initial $2\pi/K$=100 km (ray on down-slope side), and 0.625×benchmark N and initial $2\pi/K$=150 km (up-slope side). Top panel does not include $\mathbf{u}_{deep}$, while lower panel does. In both panels, the LOKE $_{20\text{-}100d}$ contours from Figure 3.1-4 are superimposed.

more so in the upper than lower slope region if a cyclonic shear exists. The lower panel of Figure 3.1-11 shows this effect, and shows how rays are confined to remain in the vicinity of the 3,000-m isobath. Extensive tests verify that this confinement of rays is valid also for rays of other periods, 32, 42.7 and 51.2 days, for longer wavelengths up to ≈ 250 km, and also for other stations. Figure 3.1-11 shows that the down slope turning of the ray is first affected near 90~91°W in a region of cyclonic shear ($\varsigma \approx 0.05f\ s^{-1}$). The amount of turning caused by current shear as ray propagates up-slope can be estimated from equation (2.3-11):

$$\delta\theta|_{\varsigma\neq 0} \approx -\int_{ray} |k|\ \varsigma/(|\nabla h|N)\ C_{g2}\ dt, \qquad (3.1\text{-}3)$$

which, with appropriate values (from the PE model) $|k| \approx 0.01\ km^{-1}$, $\varsigma \approx 0.05f\ s^{-1}$, $|\nabla h|N \approx 5\times10^{-6}\ s^{-1}$ and $\int_{ray} C_{g2} dt \approx 10$ km, gives $\delta\theta|_{\varsigma\neq 0} \approx -4^o$. This value, while reasonable, is likely to be an under-estimated one. As explained in Section 2.3, since $d(|\nabla h|N)/dt > 0$, dk_i^2/dt also > 0 (from equation (3.1-2) or (2.3-10)), and the mere existence of a deep current (without shear) in the direction of k (<0) would cause rays to turn down slope, i.e. contributes to additional (more negative) δθ. An upper-bound (i.e. maximum possible turning) estimate of this latter effect is obtained from equations (2.3-10) and (3.1-2) with ς=0:

$$\delta\theta|_{\varsigma=0} = \int_{ray} (d|k|/dt)(|\nabla h|N)^{-1}\ u_{deep}\ dt > \int_{ray} (\partial|\nabla h|/\partial y)|\nabla h|^{-1}\ u_{deep}\ dt\ , \qquad (3.1\text{-}4)$$

which, with $(\partial|\nabla h|/\partial y)|\nabla h|^{-1} \approx 2\times10^{-2}\ km^{-1}$ and $\int_{ray} u_{deep} dt \approx -5$ km, gives $0 > \delta\theta|_{\varsigma=0} > -6^o$ or roughly the same contribution as that from current shear alone. It is concluded therefore that the presence of deep currents over the 2,000-3,500 m isobaths (Figure 2.3-3) explains why in the PE model simulation there is little LOKE upslope, i.e. why the LOKE is predominantly confined within the CGKE band. This is particularly so for TRW rays with periods shorter than about 43 days, and the ray-confinement is more effective when the current also contains a cyclonic shear. In the region of the base of the slope at 90°W where the PE model shows strong, deep cyclonic flows, the recent current observations (Hamilton et al. 2003) also show that TRW energy does not penetrate upslope of the Sigsbee Escarpment. Hamilton et al., (2003) speculate that reflection of upslope propagating TRW's by the steep escarpment may account for the lack of energy over the lower slope, but the refraction mechanisms discussed here may also contribute to the insulation of the slope from energetic TRW motions.

3.1.5 Discussion

The model LC executes a south-north-south vacillation approximately every 5-6 months, and sheds a LCE every 10 months or so. These periods are too long for a direct forcing of the TRW's. The vorticity maps of Figure 3.1-1 show the appearance of small-scale disturbances around the LC and shedding and propagating LCE's. The study of these *meanders* (i.e. the mechanism of how they are produced) clearly deserves a separate treatment (see recommendations in Chapter 6). However, it is shown, in the following, how these short-scale fluctuations can provide the necessary linkage for energy transfer from the LC and LCE's to deep motions. An example of a specific TRW event is given and the implications of what ray-paths may mean to the existence of deep currents, discussed.

Sources of TRW Energy

The example focuses, on station #2, the origin (energy source) for ray #2. Results at other stations are similar. Figure 3.1-12 shows, at 5-day intervals, vorticity maps in an enlarged region of the LC during a period of its northward extrusion before an eddy-shedding event. It shows clearly the appearance of high cyclonic vorticity perturbations that propagate around the LC and into the Florida Straits (e.g. day 901-921, and also day 931-956). The source of these cyclonic disturbances appears to be along the western edge of the LC in the Yucatan Straits. The meander begins as these disturbances traverse across the Yucatan shelf and slope into the deep Gulf (e.g. day 921, 926 and 931). Because of the color contrast, cyclones are most visible in these maps, but propagating anticyclones are also present. These cyclones and anticyclones constitute the propagating meanders that were referred to above. By noting the recurrences of the meanders from these and similar maps, it is possible to infer time scales (~ periods) of approximately 20 to 60 days, and spatial scales (~ wavelengths) about 100 to 200 km. To examine more closely how these shorter-scale fluctuations near the surface excite deep currents, time-series analyses of various dynamical variables was performed at several stations. An example at station 2 of Figure 3.1-7 (shown as the '+' point in Figure 3.1-12) is given in Figure 3.1-13. The top two panels give time variations of the layer-1 depth and (relative) vorticity, respectively, that cover approximately five periods of northward LC extrusion and eddy-shedding. LCE shedding occurs at approximately model day 450, 750, 1,150, 1,500 and 1,800 (denoted by the symbol 'E' in each panel; c.f. Figure 3.1-1b), each time at the 'foot' of a sudden drop in layer-1 depth. The drop is followed by a trough (i.e. a low) that lasts approximately 100 days, then a relatively slower rise that crests in approximately 200 days, that signifies the northward extrusion of LC past the station. On these LC-extrusion and LCE-shedding time scales, the vorticity is highly anticorrelated with layer-1 depth: it becomes more negative (i.e. anti-cyclonic) during layer-1's rise and maximizes to about zero vorticity during layer-1's trough. Apparent in the vorticity time-series is the existence of high-frequency fluctuations during periods of LC extrusion (when ζ/f becomes more negative and layer-1 deepens), and the absence of these fluctuations when the LC retreats southward of the station after each shedding. The layer-1 depth time-series shows similar, though less transparent, characteristics. It is clear that these fluctuations are associated with propagating meanders and other LC variability when the latter extends northward (Figure 3.1-12).

The existence of these fluctuations in the 20 to 100-day, TRW periods can be most clearly seen in the band-passed time series. The middle two panels of Figure 3.1-13 show 20 to 50-day band-passed kinetic energy in layers 1 and 4, respectively, and lower two panels show same in the 50 to 100-day periods. The plots show clearly the amplification of these shorter-period (i.e. periods less than LC north-south vacillation and LCE-shedding periods) fluctuations near the surface during the LC's northward extrusion phase, and also how they almost disappear when the LC retracts following a shedding event. The fluctuations transmit to the lower layer (#4), where the energy of the combined 20 to 50-day and 50 to 100-day intervals account for approximately 64% of the total lower-layer energy. Thus longer-period LC vacillations and LCE sheddings near the surface have little direct signature in the lower layer (they actually account for less than 10% of the lower-layer energy, with the remaining, approximately 25%, residing in the almost steady bottom currents), while the short-scale parasite fluctuations they produce, which account

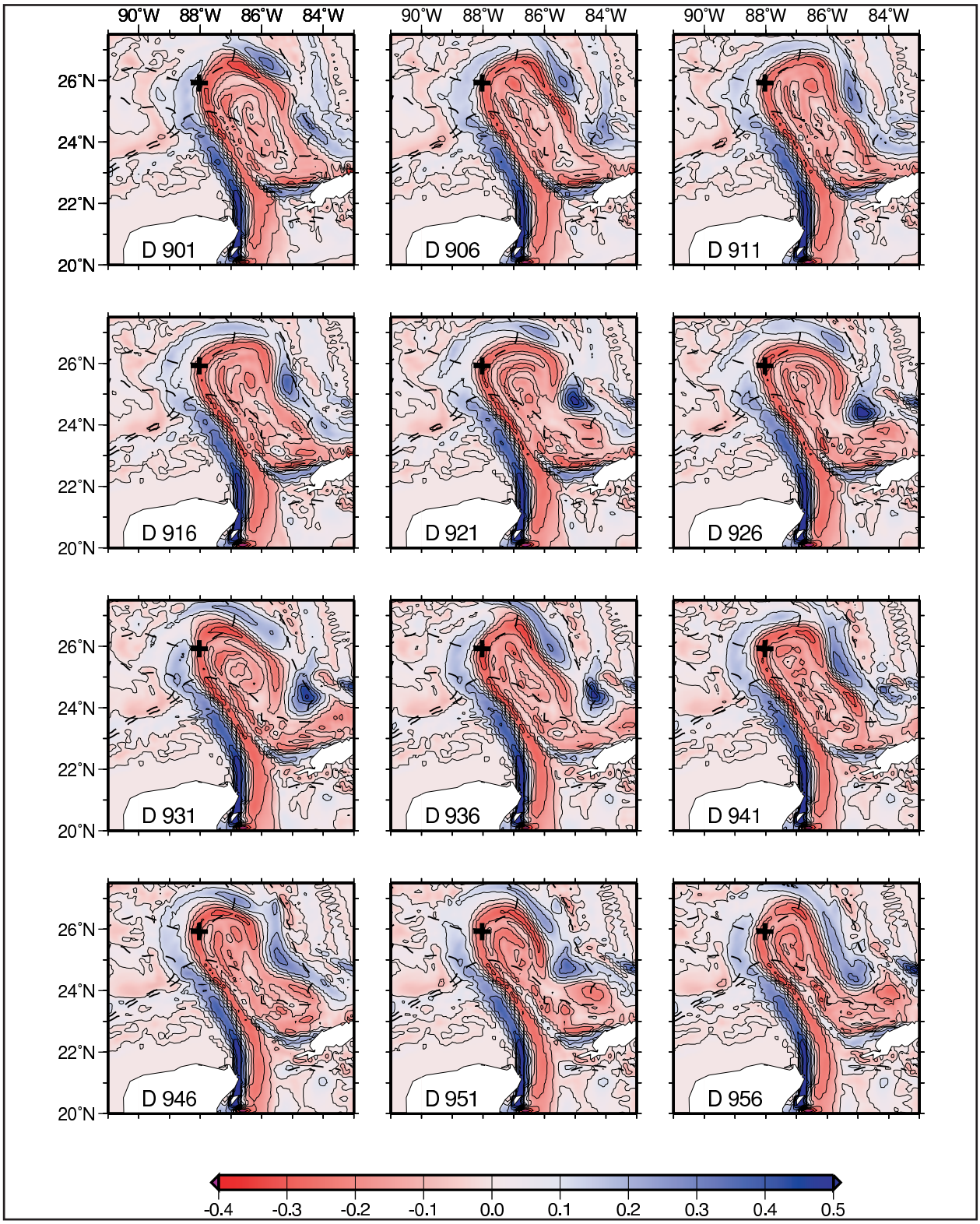

Figure 3.1-12. Vorticity maps at 5-day interval in an enlarged region of the LC during a period of its northward extrusion before an eddy-shedding event (on day 1150, not shown). The '+' symbol indicates origin of ray #2 of Figure 3.1-7a. Dashed contours denote the 3000 m and 3500 m isobaths.

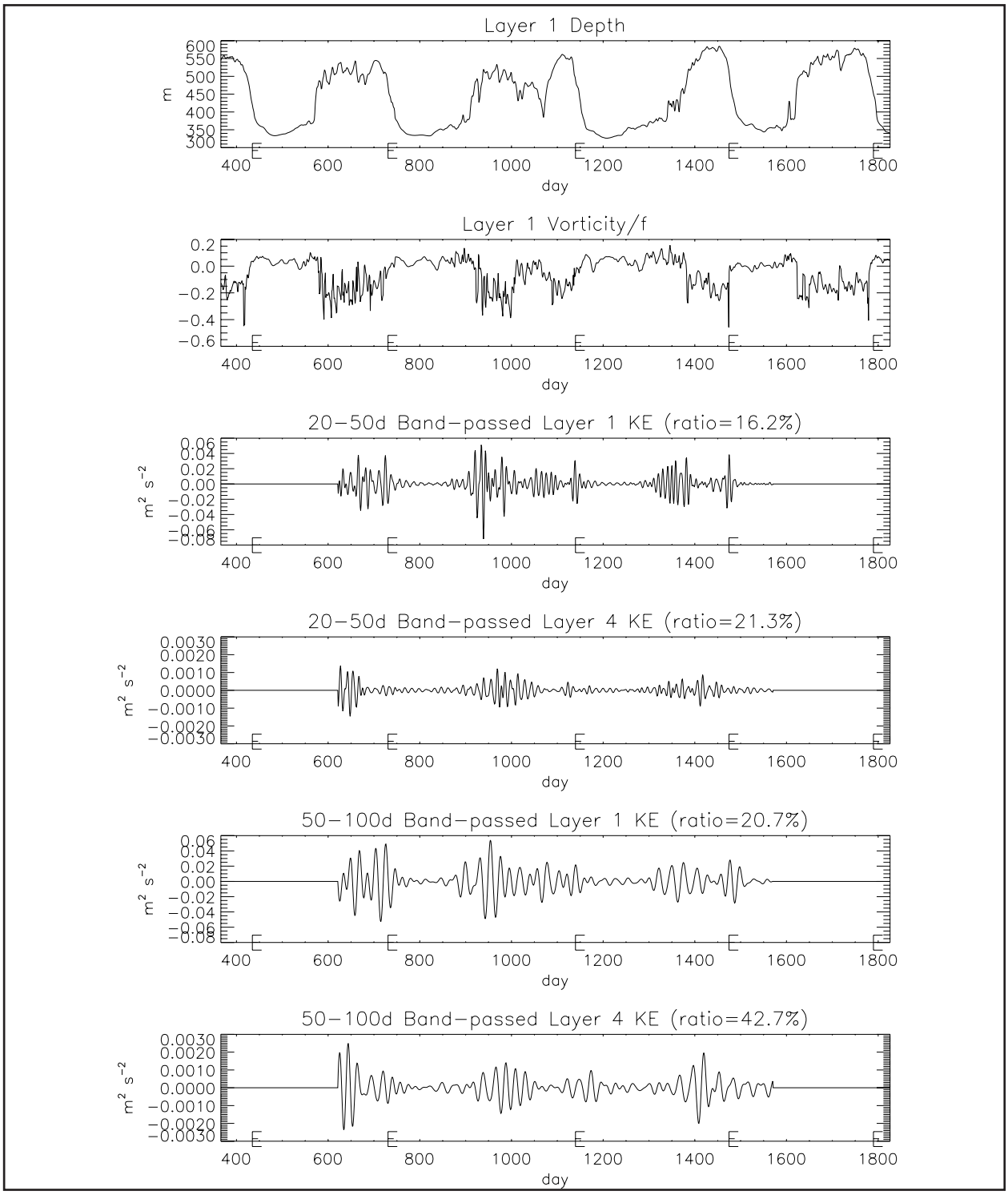

Figure 3.1-13. Time-series at station #2 (i.e. the '+' point in Figure 3.1-12). Top two panels: time variations of the layer-1 depth and (relative) vorticity; middle two panels: 20 to 50-day band-passed kinetic energy in layers 1 and 4; bottom two panels: 50 to 100-day band-passed kinetic energy in layers 1 and 4. The symbol 'E' indicates times when LCEs are shed in the model. Ratio (in panels 3 to 6) = (Energy in respective band)/ (Energy over the entire spectrum).

for only 37% of the near-surface kinetic energy (Figure 3.1-13), have profound impact on the lower-layer motions.

To infer the inter-connections between the upper and lower-layer fluctuations, the time-lagged correlations of various quantities were calculated, focusing on the 20 to 100-day periods. Let h_i, ζ_i, and KE_i be the fluctuations in the layer-depth, relative vorticity and kinetic energy, respectively, of the i^{th} layer. Typical for these time series, correlations which exceed 0.15 differ from zero at the 95% confidence level. It is found that h_1 and ζ_1 are *negatively* correlated (= -–0.5) with the former leading slightly by 1 day. Because potential vorticity is conserved, the negative correlation (and non-zero lag) suggests the importance of advection in layer 1 where currents due to the LC are strong, typically of O(1 m^{-s}). On the contrary, h_4 and ζ_4 are positively correlated = 0.5 with zero lag, which suggests excellent *local* conservation of potential vorticity: $\partial[(f+\zeta_4)/h_4]/\partial t \approx 0$. The link between near-surface and near-bottom motions comes through h_1 and h_4, which are negatively correlated (= –0.6) with h_1 leading h_4 by about 3 days. Thus, bottom energy in the 20 to 100-day periods originates from regions under active LC and LCE variability, and its excitation by LC and LCE's, therefore, goes as follows. Through dynamical instabilities of some kind, propagating meanders develop around the perimeter of these larger-scale features, where currents are strong (~1 m^{-s}) and strongly sheared. These meanders have length scales of O (100~200 km) and temporal scales of about 20 to 60 days (Figure 3.1-12). Though not as readily identified from the vorticity maps, there also exist fluctuations of comparable energy in the 50 to 100-day band (Figure 3.1-13). Variations that cause layer-stretching (shrinking) near the surface force shrinking (stretching) of the near-bottom layer, which through potential vorticity conservation induces anticyclonic (cyclonic) near-bottom vorticity. It is not entirely trivial however, how this near-bottom vorticity fluctuations transforms into the kinetic energy of TRW's (included in KE_4). Indeed, the conditions under which a transfer of energy from the surface meanders to TRW motions might be possible, have not been studied. The transfer *may be* caused by the phase-matching mechanism proposed by Pickart (1995; due originally to Malanotte-Rizzoli; see also Pedlosky, 1977), especially in the vicinity of station #2 where the 3,000-m isobath tilts from southwest to northeast (Figure 3.1-12; similarly also for station #1 on the 3,200 m isobath). This tilt allows eastward TRW phase propagation (Figure 2.3-1) that can couple with the eastward meanders that propagate past this station, so that energy radiation becomes possible. In Pickart's study, this coupling mechanism explains that the TRW energy found off Cape Hatteras was forced by eastward Gulf Stream meanders. A similar mechanism maybe at work also in the present PE model simulation (see below), though clearly this needs to be studied in more detail, preferably within a more idealized model setting. At the I1 site (see Section 2.2), north of station #2, Hamilton et al. (2003) found a few events where current fluctuations were visually coherent through the 2,000 m water column. These events were associated with cyclonic eddies on the LC or a LCE front. Thus, there is some, but not conclusive, observational support for this type of coupling mechanism.

Though weaker in strengths, similar excitations of TRW's by meanders around the LC as described above also exist around detached LCE's that propagate southwestward in the PE model (not shown). In this case, the combined planetary beta and (gentler) sloping topography in the deeper portion of the central Gulf (beyond the 3,000-m isobath) contribute to the west/ northwestward spread of TRW energy, as discussed previously for rays #4-6 in Figure 3.1-7a.

Robustness of the Calculation and Example of a Specific Event

The excitation mechanism suggested herein is apparently more akin to Pickart (1995) than to that described in Hogg (1981) and Louis et al. (1982). These latter works suggest forcing of the TRW's through response to specific ring shedding event, that is, being more of an impulse response, rather than a near-periodic forcing problem by propagating meanders. In the Gulf of Mexico, Hamilton (1990) found correlations between pairs of eastern and western moorings that were related to LCE-shedding events. On the other hand, secondary small-scale features such as meanders owe their existence to forcing by LC and LCE's, the movement of which over a specific area (topographic slope in particular) can therefore be considered as 'impulsive' (~1–2 weeks). While costs and logistics generally dictate that observations (of TRW's) are for specific events, modelers can afford longer-term (model) data and are compelled to demonstrate the occurrence of more than one or two specific events only, as these can arise due to specialized forcing, initial and boundary conditions, and sometimes even to the particular model grid being used. Therefore, an analysis of the deep EKE, as a seven-year ensemble of specific excitation and propagation events of TRW's (Figures 3.1-4 and 3.1-7), has been performed. The existence of a band of deep EKE across the central Gulf (the CGKE) provides some evidence that the simulated events are robust model features that are repeatable (this is clear from animation of LOKE). To further ascertain this, the 10-year simulation has been repeated by doubling the horizontal grid resolution. It is found that this doubled-resolution experiment also gives a very similar (last seven year) composite map of deep EKE containing the CGKE band as in Figure 3.1-4, and which also is made up of individual TRW excitation and propagation events. The difference is that the deep EKE is now more intense (Oey, 1998). Therefore, an example is given of a typical TRW excitation and propagation event taken from the doubled-resolution seven-year ensemble.

Figure 3.1-14 plots images of EKE at 188 m above the bottom, where the EKE is dominated by energy in the 20 to 100-day band, and contours of $EKE|_{20\text{-}100d}$ are virtually identical. The EKE (model sigma-level 17; green-red-yellow, values less than 1.4×10^{-2} m^2 s^{-2} are omitted) is superimposed on 200 m Eulerian trajectories (tracked for 5 days and launched at every 12^{th} grid point) that are colored with local values of ς/f (dark blue for cyclone ≥ 0.4 and red for anticyclone ≤ -0.4). These trajectories indicate the locations of the near-surface LC and eddies. For example, the LC front is delineated by the transition from red to blue trajectories. On days 1,345 and 1,370, the front passes over point #1 and point #2, respectively. Point #1 is the same as station #1 of Figure 3.1-7, and point #2 is slightly south (by 0.3^{o}Lat) of station #2. Note also that meanders typically have cross-frontal amplitude of about 50 km (i.e. $\approx$ 10 grids), and therefore cannot be readily distinguished in trajectories launched every 12^{th} point. They are nonetheless easily seen in maps of relative vorticity as in Figure 3.1-12. On day 1,370, high EKE region is seen stretching westward and onshore from point #1, following approximately the 3,000-m isobath. High EKE is also seen at point #2. On days 1385 and 1405, these high EKE progressed westward to point 'R', the ray-convergence zone discussed previously in conjunction with Figure 3.1-7. Despite the rich (surface) eddy structures west of 88°W, deep EKE rarely rises above the 1.4×10^{-2} $(m\ s^{-1})^2$ cut-off except near the 3,000-m isobath when the high EKE arrives, a phenomenon strongly suggestive of TRW propagation as discussed previously. Figure 3.1-14 also shows two TRW rays launched from point #1 using properties at day 1345 as initial conditions, and also from point #2 using day 1370 as initial conditions. Both calculations also

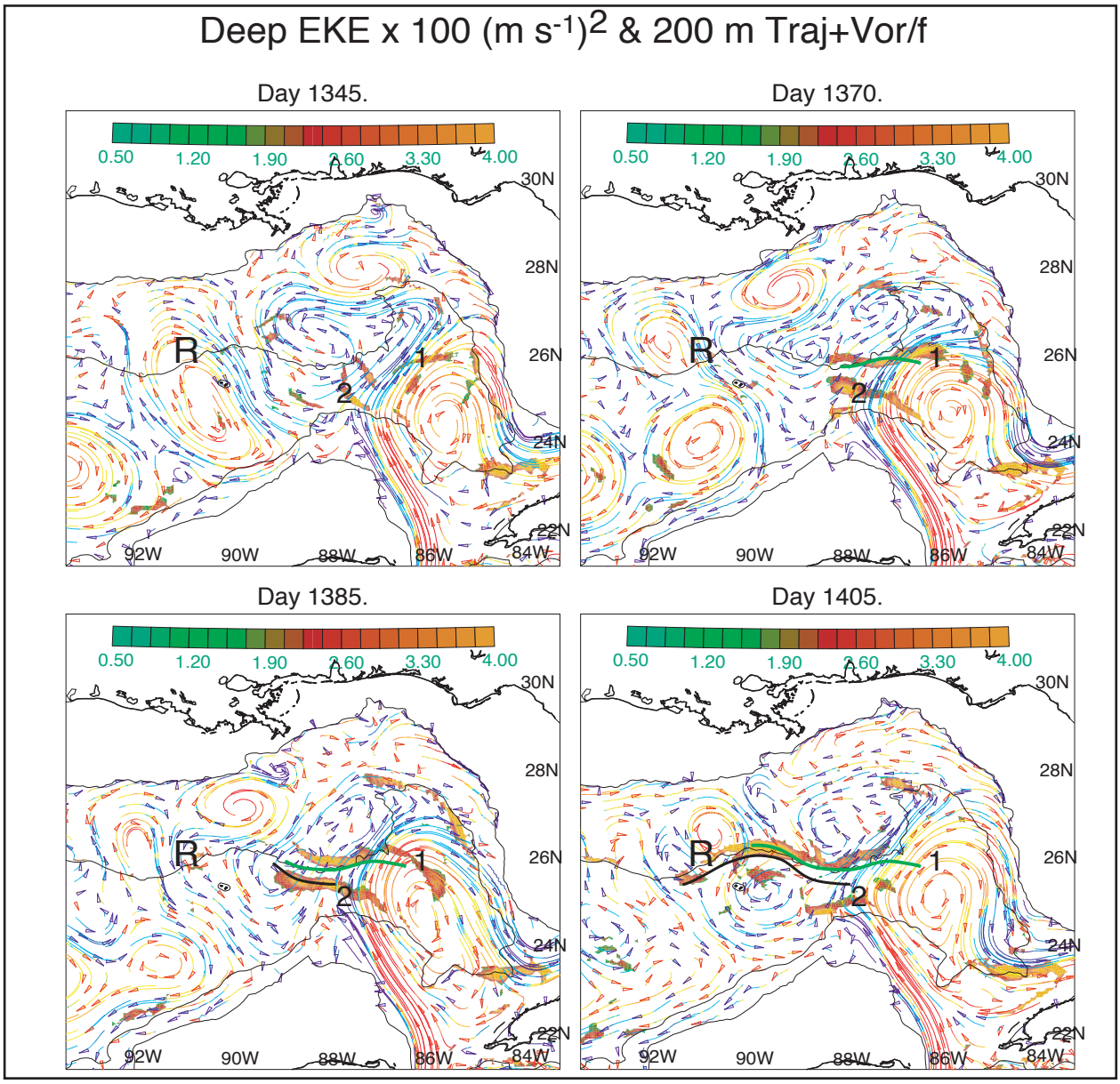

Figure 3.1-14. Modeled eddy kinetic energy (green-red shade, values ≤ 1.4×10^{-2} m^2 s^{-2} are omitted) at 188 m above the bottom on day 1345 (top-left panel) when the northern edge of LC touches point #1 and a TRW ray (green) is initiated there; on day 1370 (top-right) when the northwestern edge of LC touches point #2, and a second TRW ray is initiated there (black); on day 1385 (bottom-left), and day 1405 (bottom-right). The arrowed curves are Eulerian trajectories at 200 m below the surface, released at every 12th model point and each tracked for 5 days (scale = 0.5 m s^{-1} per 100 km), and colors on them indicate local values of V/f; dark-blue is cyclonic ≥ 0.4, and red is anticyclonic ≤ -0.4. Dotted curves are the 200-m and 3000-m isobaths. Point 'R' marks the location where TRW rays converge. Note that despite rich (surface) eddy structures west of 88°W, deep EKE rarely rises above the 1.4×10^{-2} m^2 s^{-2} cut-off, except near the 3000-m isobath where TRW's pass.

include deep mean (seven-year) currents (see previous section). Despite the many simplifications inherent in the TRW theory, the rays are seen to track the high EKE progression fairly well. In particular, both rays would eventually converge near 90° to 91°W. Also, the velocity of progression of the EKE feature, ≈ –8.3 km day^{-1}, matches well the average of the group velocities of the two rays (≈9 km day^{-1}). Similar events of excitation and propagation of TRW's are also found to be triggered by southwestward propagating LCE's in the western Gulf (not shown).

Ray-Paths and the Existence of Deep Currents

It has been showed that the generally westward deep currents in the model Gulf increase the TRW group speeds, and also confine rays to the vicinity of the 3,000-m isobath in more accordance with the simulated CGKE band (Figures 3.1-7 and 3.1-11). Thus, knowledge of group speeds and ray-paths may provide information on deep currents. Based on a time-lagged correlation analysis between two deep moorings, one in the eastern (Mooring G at (85°30'W, 25°36'N) on 3,200 m; see Section 2.2) and another one in the western Gulf (Mooring Q at (94°53'W, 25°52'N) on 3,000 m) Gulf, Hamilton (1990) obtained a lag-time of 106 days, and estimated a *lower bound* group velocity of –9 km day^{-1} by assuming a straight-line distance between the two moorings. If, as suggested by our ray calculation, the ray-path is curved approximately following the 3,000-m isobath, the additional distance of 140 km would yield a group velocity of about –10.3 km day^{-1}. Hamilton also used the dispersion relation to arrive at an estimate of $|\mathbf{C_g}| \approx 8.5$ km day^{-1} based on a wavelength value of about 189 km. Thus, there is a difference in group velocity of about –2 km day^{-1}. Hamilton's $\mathbf{C_g}$ values can be compared with the present averaged values (after applying a small 5.5% adjustment to account for the differences in wavelength and N between Hamilton's and this work) of –11.3 and –8.5 km day^{-1}, with and without $\mathbf{u}_{deep}$ respectively. In the present case, the difference, about –3 km/day, is entirely caused by $\mathbf{u}_{deep}$. The –2 km day^{-1} (≈–2 cm s^{-1}) difference in Hamilton's case may also be due to the existence of deep currents. His analysis, and also that of Hamilton et al. (2003) for site I1, suggests that the observed TRW's do not stray far up-slope, which may also imply existence of deep shear flows.

3.2 Comparisons with Deep Current Measurements

This section discusses the characteristics of the deep velocity field from the model run, described above, and the same model run (i.e. the same grid, forcing and boundary conditions) with assimilation of satellite altimetry and SST, using the methods of section 2.1.1. The assimilation scheme synchronizes the upper-layer eddy field with reality and therefore, the interest is in whether the energy levels of the TRW's are improved over the regular non-assimilated run. The assimilation method does not directly influence the model fields below ~ 500 m. Profiles of velocity, temperature and salinity were extracted from the model runs at the positions shown in Figure 3.2-1. The last three years of the runs were used with a time interval of 3 hours. The positions in Figure 3.2-1 include all the mooring sites in Table 2.2-1, as well as other deep-water sites taken from the SAIC database, and a set of slope positions at regular intervals around the Gulf.

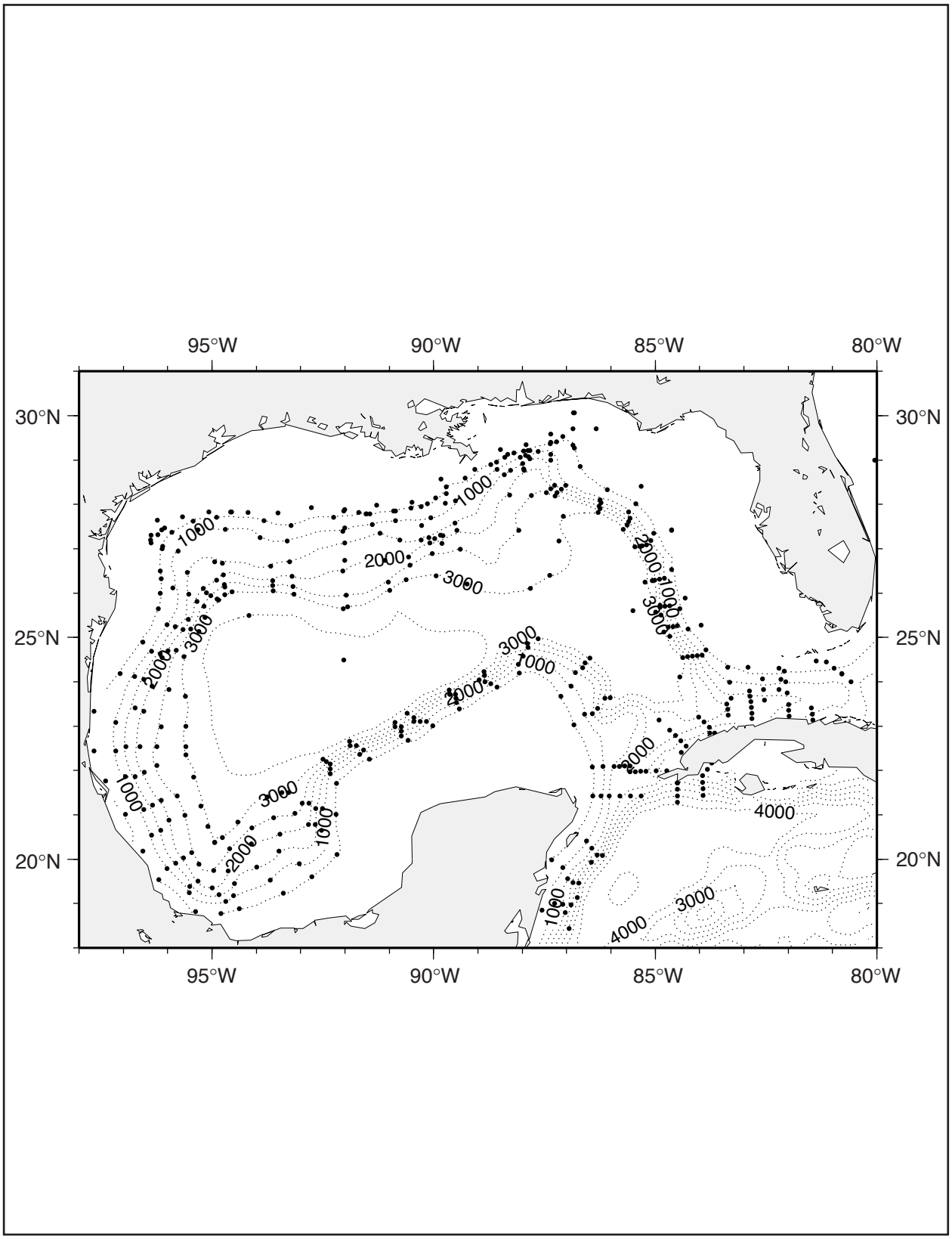

Figure 3.2-1. Positions of model-saved daily profiles of velocity, temperature and salinity.

3.2.1 Statistics and Spectra

Figure 3.2-2 shows the standard deviation ellipses for the observations and from the regular run. The observations are generally within about 200 m from the bottom and the model data is from the nearest sigma-level. The last two years of the model run were used, and the observations were 40-HLP filtered and vary in length from about 2.5 to 0.5 years. The model underestimates the kinetic energy (KE) at almost all sites for reasons discussed above. The largest differences are under the LC (site G) and south of the delta (site I). The latter seems to be an exceptional area for high energy TRW's (Hamilton et al. 2003) which are characterized by short periods (~ 10 to 12 days) and short wavelengths (~ 60 to 100 km). The model is not expected to be able to resolve such motions and thus the comparison at this site is not particularly valid. The model shows rather more homogeneous distribution of KE than the data, though the observations are taken over different periods. The model data are also more polarized along the isobath direction than the observations, and again this is probably because the model favors the longer period and longer wavelength waves. However, the model does show an increase in energy from the base of the slope into deeper water, as observed, because of the CGKE band. When the assimilation model results are compared (Figure 3.2-3), it is immediately apparent that the model deep KE has increased over the regular run at all sites. Except for under the LC (site G), the deeper sites (GG and R) have the largest increases indicating that the CGKE band is more active. Site I also shows a large relative increase and it is speculated that a more accurate pulsating of the LC may be generating TRW's that are propagating into this region south of the delta. A comparison of upper-layer eddy speeds as a function of horizontal eddy scale, between model runs, shows that the assimilation model generates similar higher speeds at scales similar to the model with double resolution, but without assimilation (Figure 3.2-4). Therefore, the higher speeds of upper-layer eddy flows, in the assimilation model, are reflected in the lower KE increases. Despite the improvements, the assimilation model still underestimates the observed KE.

The KE spectra, in variance preserving form where equal area under the curve represent equal variances in frequency space, for the observed currents at five of the deep-water sites are given in Figure 3.2-5. All the moorings show bottom intensification where more than one measurement is available below 1,000 m. The highest energies are in the east (G and I1) and apart from G, which is under the LC, all sites show a prominent peak at about 20 to 30 days. Under the LC at G, the highest energies are at longer periods of 30 to 50 days and around 100 days. At I1, there is high energy at higher frequencies (periods of 7 to 12 days) that is not in evidence at the other sites. The bottom left-hand plot in Figure 3.2-5 shows the large increase in energy between the base of the slope (FF) and the deep basin (GG). There is a similar contrast between P and R and A and G in the western and eastern Gulf, respectively (not shown – see Hamilton, 1990). Similar KE spectra for the same sites (except FF), but using data from the assimilated model, are shown in Figure 3.2-6. Apart from the differences in the variance scales, noted in Figure 3.2-3, the model spectra also show bottom intensification at most frequencies and similar spectral peaks. Site G, under the LC, is more barotropic than other sites and its prominent spectral peak is at about 20 to 30 days, similar to the other model sites. Site I1, however, does show an 8 to 10-day peak as well as the one at longer periods, indicating that the model is generating some of the higher frequency TRW energy on the northwest side of the LC. The model I1 and G also have an energetic peak at periods greater than 100 days. This is probably related to LC pulsation and if it occurs at all in the observations at G and I1 that can

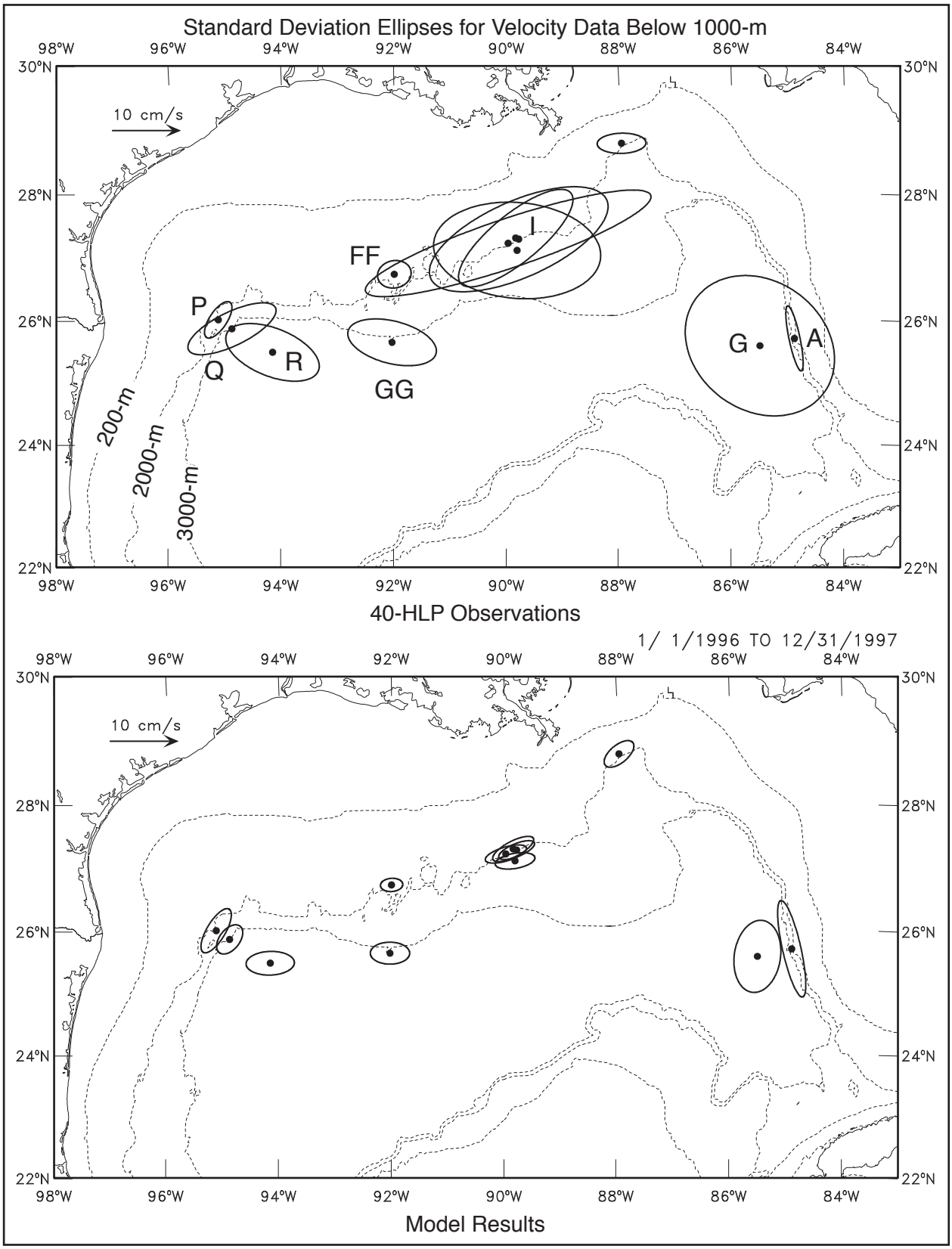

Figure 3.2-2. Standard deviation ellipses for velocity data below 1000 m from observations (top panel), and the regular model run.

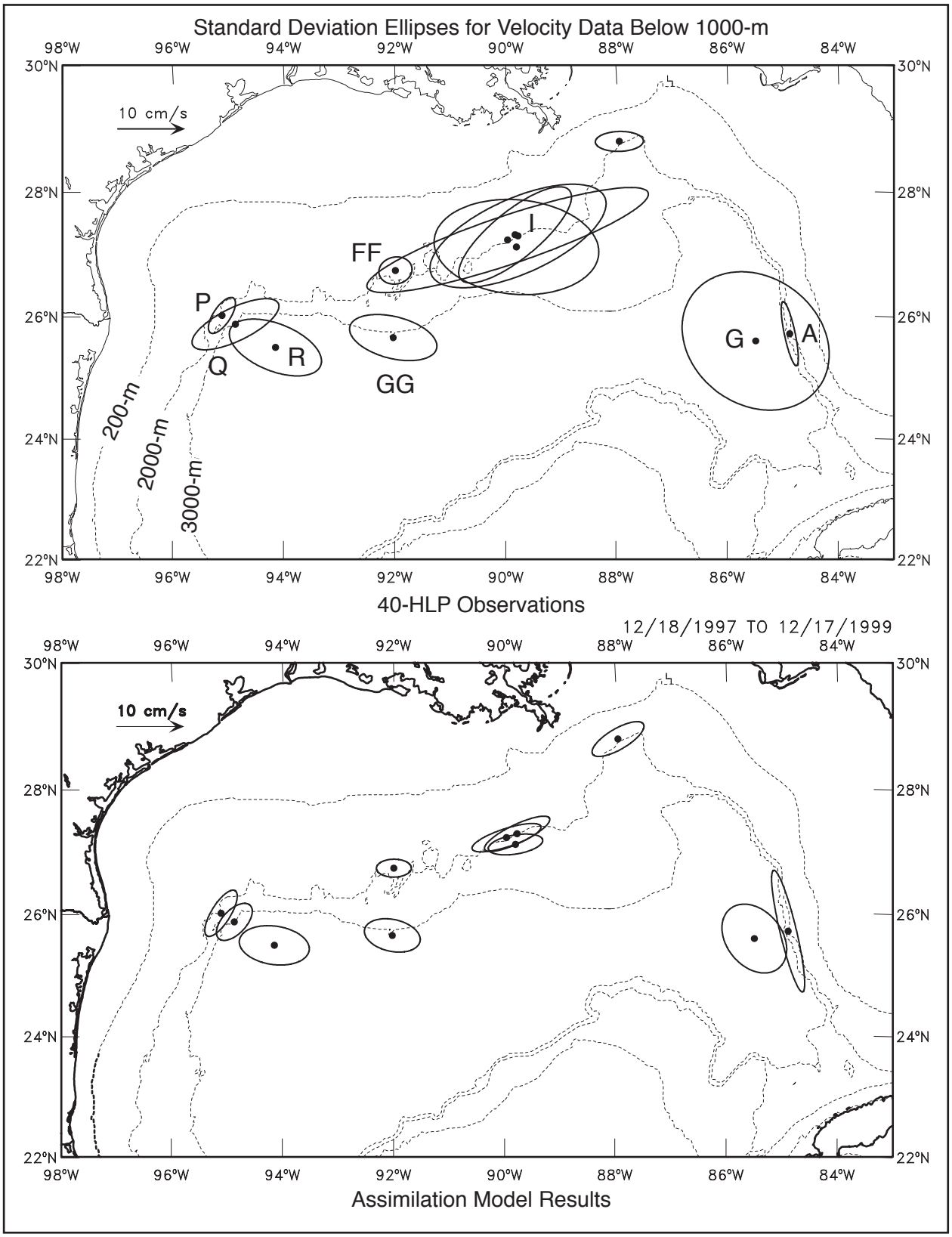

Figure 3.2-3. Standard deviation ellipses for velocity data below 1000 m from observations (top panel), and the assimilation model run.

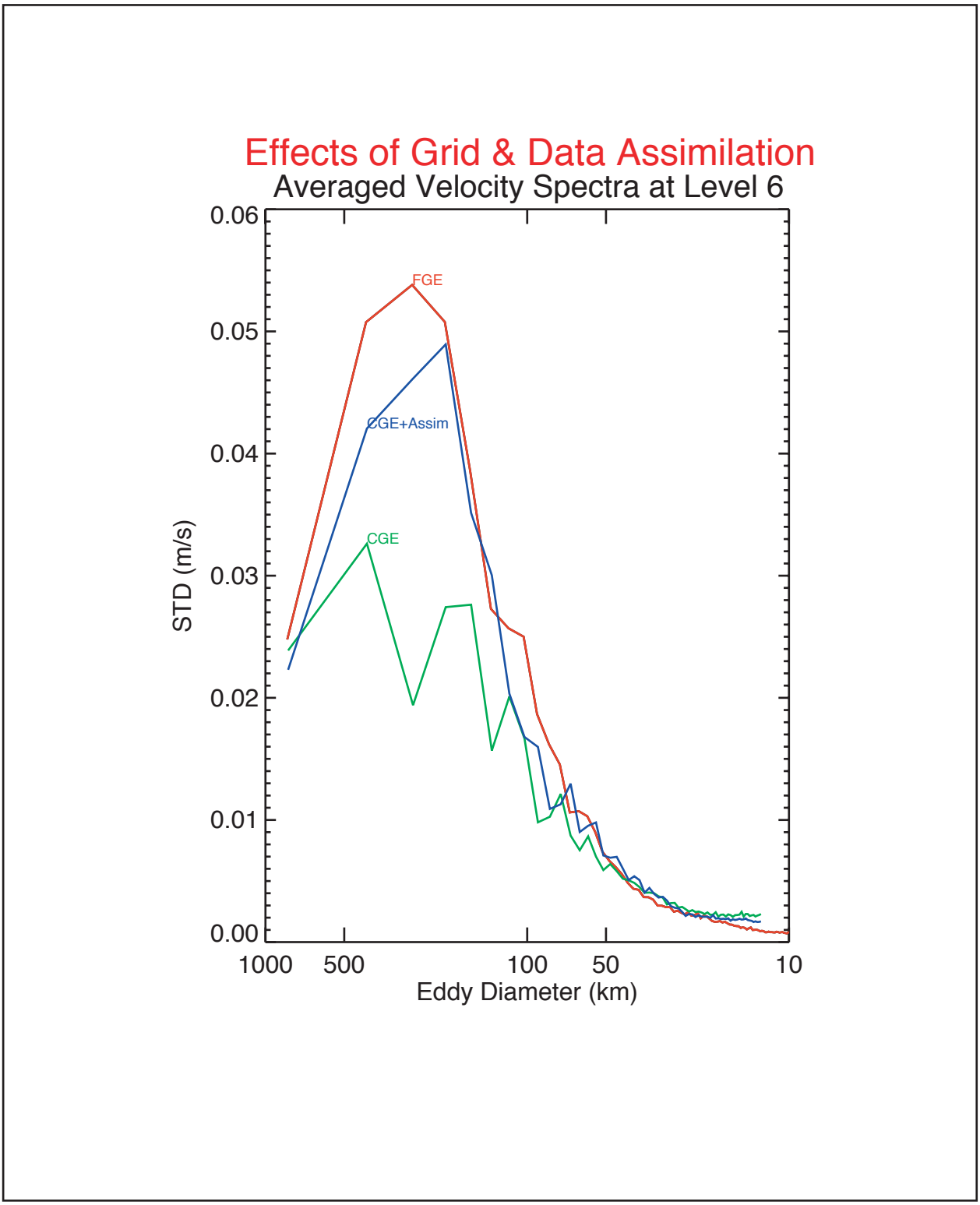

Figure 3.2-4. Eight-year, time-averaged velocity spectra expressed in m s^{-1} at sigma-level 6 (100 m below the surface) as a function of the spatial scale for model region north of 26°N but deeper than the 500 m isobath. Green - regular model, blue - model with assimilation, and red - regular model with double resolution.

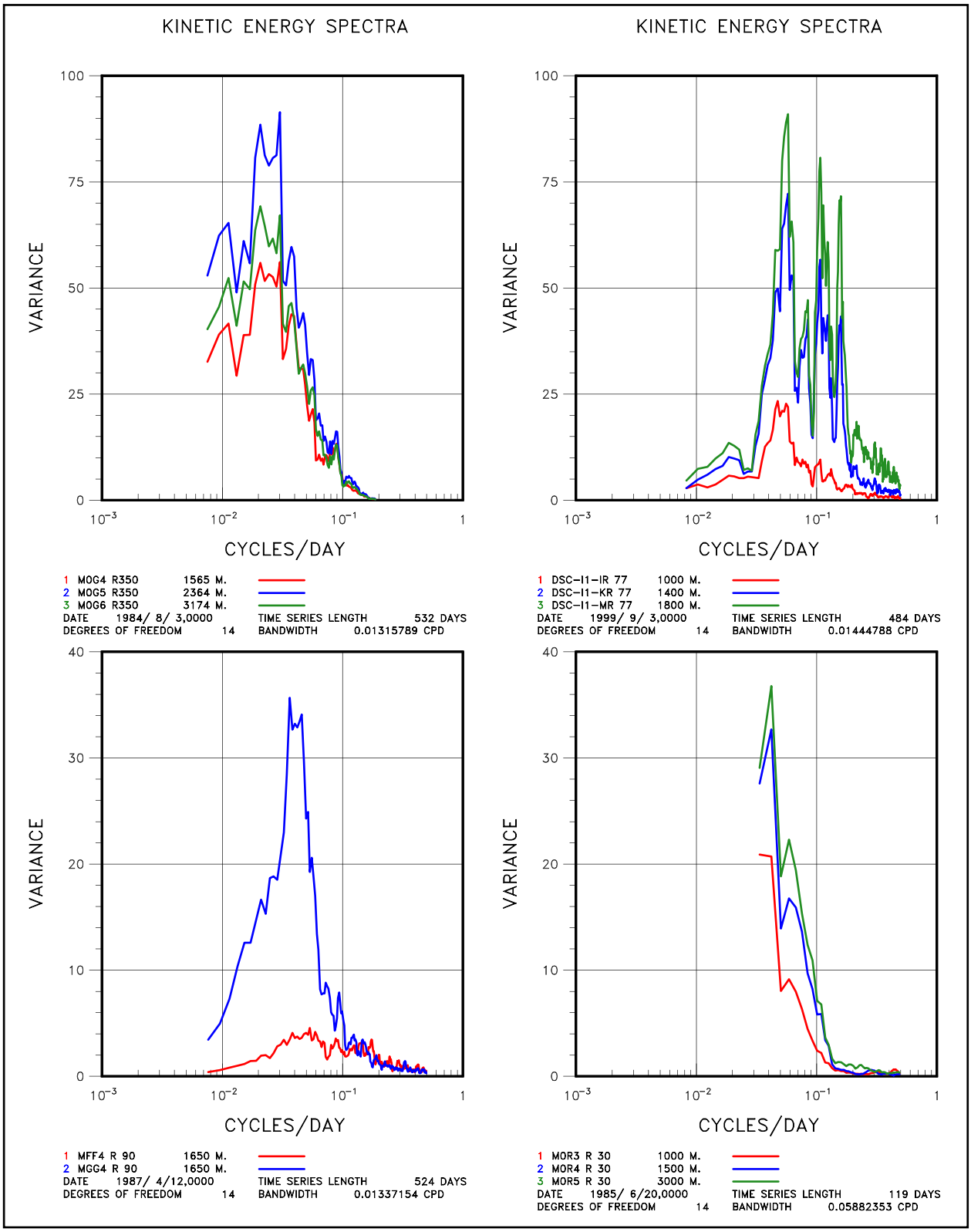

Figure 3.2-5. Kinetic energy spectra for mooring sites G (top left), I1 (top right), FF (red) and GG (blue) (bottom left), and R (bottom right) from observed currents. Depth levels and time periods are indicated in the labels.

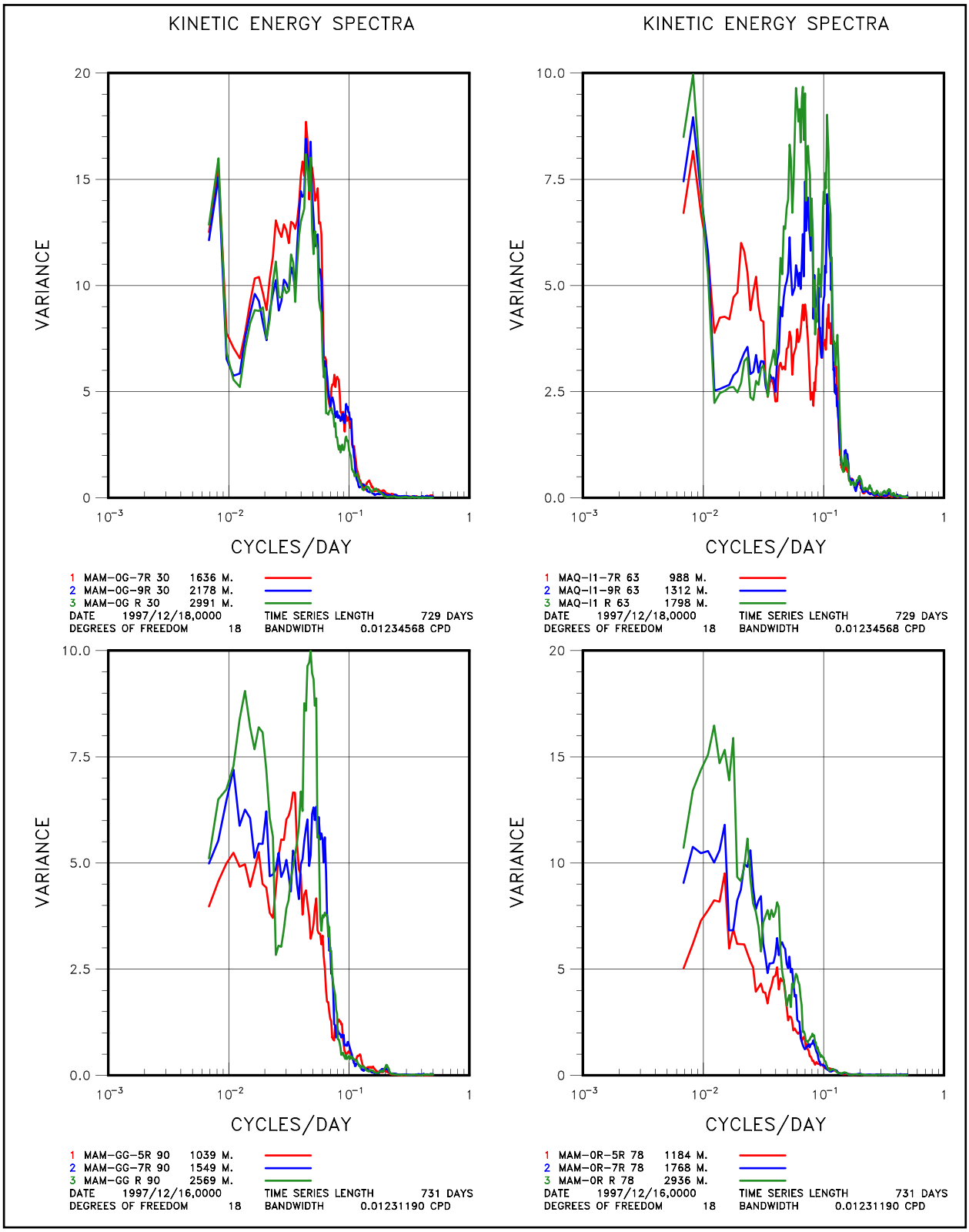

Figure 3.2-6. Kinetic energy spectra for mooring sites G (top left), I1 (top right), GG (bottom left), and R (bottom right) using assimilated model currents. Depth levels are indicated in the labels.

resolve such long periods, it is much less apparent. Sites GG and R in the central and western Gulf show model energy at longer periods (40–100 days) that is not observed at least at GG. The observations at R are not long enough to resolve properly such long periods. Thus, the agreement of the spectral peaks and the evidence of bottom intensification between model and observations is encouraging and support the notion that TRW's are being generated and propagated in the model as discussed in the previous section.

One of the most important characteristics of the observed deep currents is the high coherence of the columnar flows. Therefore, it is useful to examine the model output to determine how depth-independent flows are in the lower water column. Figure 3.2-7 shows the results of calculating the coherence squared and phase differences between widely spaced depth pairs for sites G, I1 and R. The model data shows the high coherence and zero phase differences, similar to the observations at G and I1. The coherence levels are well above the 95% significance levels for these sites. At R, however, the model shows much less coherence than the observations, which still have a strong columnar character. Similar differences are found at P and Q. Therefore, the model seems to have difficulty in maintaining the barotropic nature of flows in the lower water column as the TRW's propagate into the western Gulf. Therefore, there is the unusual situation that the model results show more noise than the observations as far as the vertical structure is concerned.

The observed current data has been used to estimate wavelengths and dominant periods of TRW's (Hamilton, 1990; Hamilton et al., 2003). The ray-tracing equations (2.3-4) and (2.3-5) were used to trace wave paths backwards and forwards from the mooring site. The results are given in Figure 3.2-8, which should be compared with Figure 3.1-7. Rays traced from GG and R are refracted to the south along the Mexican slope and originate in the deep central Gulf. This implies that their origin is more likely to be associated with propagating eddies than the LC. However, longer wavelengths and periods can originate in the east, because the group velocities become more parallel to the isobaths (e.g. Figure 3.1-7). These calculations were performed with no background advection by the mean, deep flows that may significantly increase the southward refraction as discussed above. This latter effect may be particularly important for I1, where there is a steep escarpment and little of the high energy associated with the short wavelength TRW's appears to penetrate north and west of the site. Hamilton et al. (2003) deal with this by artificially reflecting the waves at the escarpment. A westward directed mean slope current that decreases in the offshore direction may achieve the same effect, and this is supported by the observations. Mean currents for a two-year period at 200 m from the bottom are shown (Figure 3.2-8) for I1 and a site ~ 25 km offshore (I3) that show a westward, cyclonically sheared, mean (~ 3 cm/s at I1). Whatever the mechanism, it is clear that 10 to 14 day waves, at I1, probably originate on the west side of the LC where they have the scales and periods that have a similar match to propagating cyclones on the LC front (c.f. Pickart, 1995). Moreover, these short period waves do not appear to penetrate very far to the west and this explains why little 10-day energy is observed at GG (Figure 3.2-5).

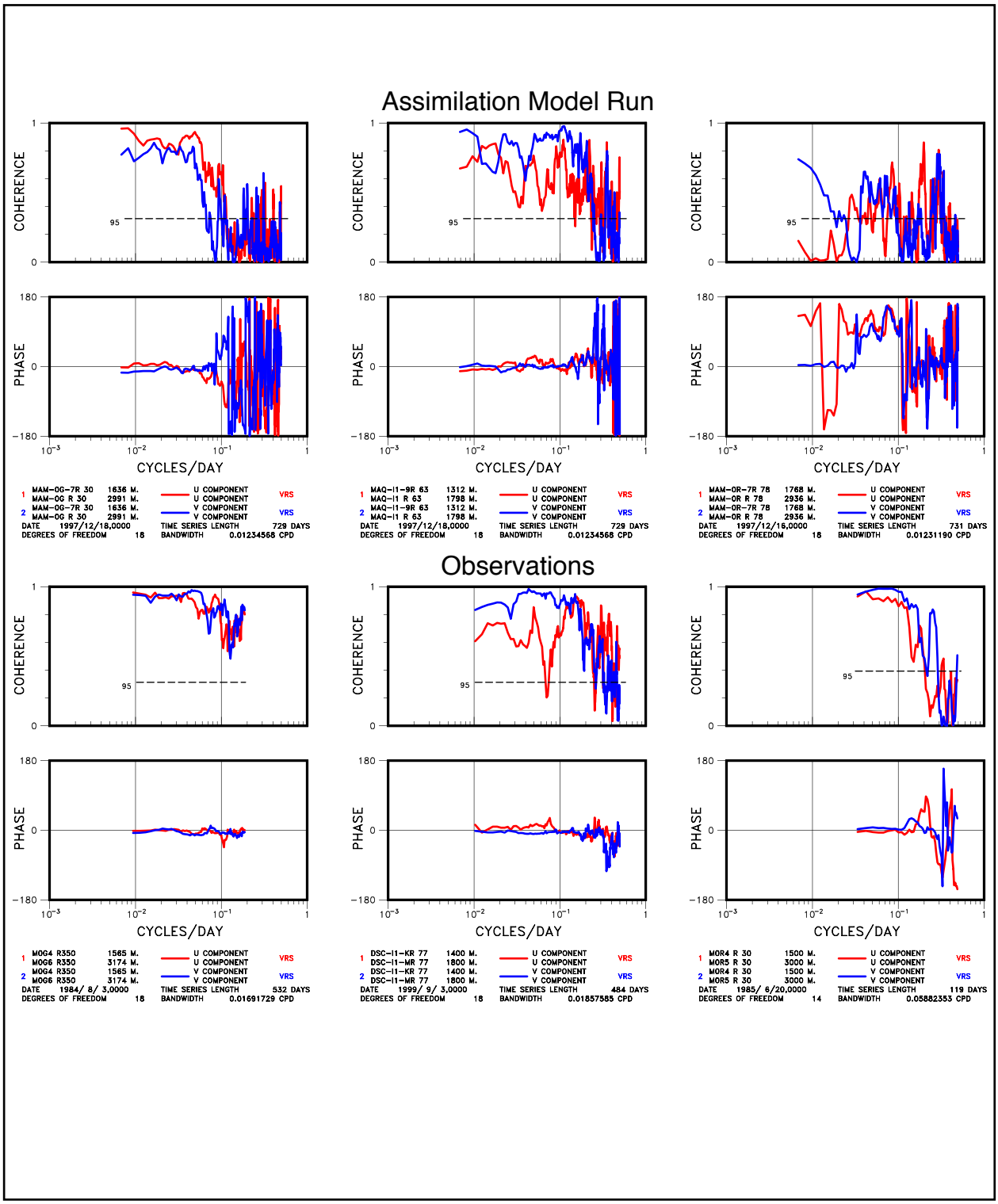

Figure 3.2-7. Coherence squared and phase differences between indicated depth levels and velocity components for sites G (lhs), I1 (middle) and R (rhs). The U and V components are across and along isobath directions, respectively. Top row is from the assimilation model run, and the bottom is from the observations. The 95% significance level is indicated.

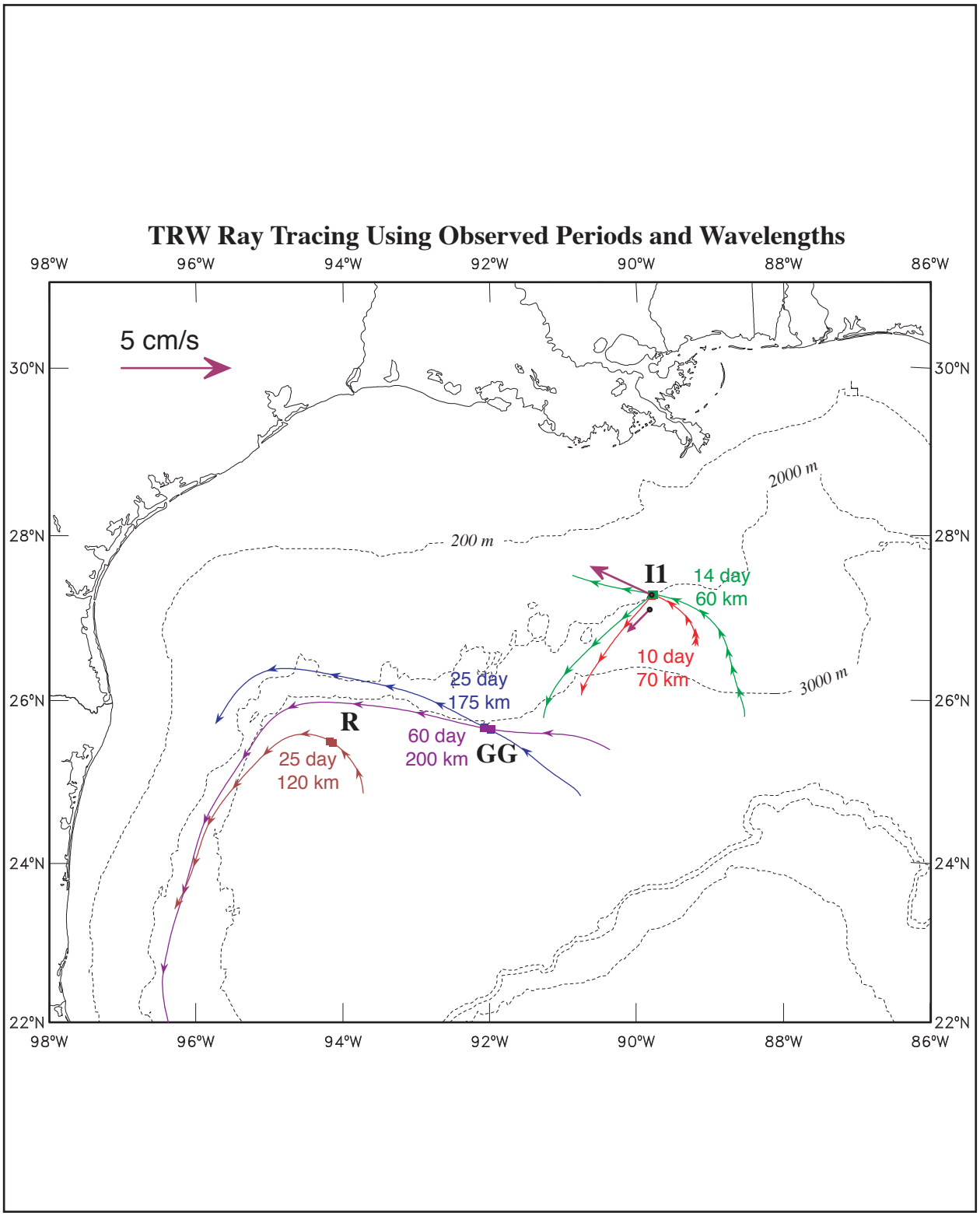

Figure 3.2-8. TRW ray tracing using observed estimated periods and wavelengths. Rays are traced backwards and forwards from the mooring sites. Arrow heads are every 5 days. The purple arrows represent two-year mean currents (9/1999 to 9/2001), 200 m from the bottom.

4. Slope Eddies

4.1 Introduction

In general, LCE's do not collide directly onto the northern Gulf slope as they rarely intrude northwards of about the 1,000-m isobath. As a result of extensive hydrographic surveys by ship and aircraft (LATEX C and GulfCet; Berger et al. 1996), the northern slope has been shown to be populated by a complex eddy field of smaller (than typical LCE's) cyclones and anticyclones with diameters ranging from ~ 20 to 150 km. An example is given in Figure 4.1-1. Eddy scales seem to be related to water depth, probably through the baroclinic Rossby radius, so that larger eddies tend to be observed on the lower slope and smaller on the upper. These slope eddies are ubiquitous and their occurrence is found at all positions along the slope from west Texas to the De Soto Canyon. The larger scale eddies have rotational periods of ~ 10 to 20 days, which are longer than typical LCE's (7 to 10 days in the central Gulf). Extensive drifter deployments in the SCULP-1 study showed that the eddies interact, with the smaller translating around the larger in the direction of the swirl velocities of the larger, more energetic eddies. This also applies to the interaction of slope eddies with eddies in the deep basin. Thus, the leading edge of a westward propagating LC anticyclone can move a peripheral cyclone onto the slope, where it may become stranded and remain on the slope as the LCE continues to the west. Similarly, a large deep-basin eddy can move smaller lower-slope eddies into deeper water (Hamilton et al., 2003). Drifters can show the short-term (a few weeks at most) evolution of specific slope eddies. However, the long-term evolution of the slope eddy field is not understood. There is limited evidence in a couple of cases that slope cyclones of ~ 100 km diameter can persist for longer than 6 months (Hamilton, 1992; Hamilton et al., 2003). Evidence will be presented that in at least one case, energy of the eddy field appears to increase with time scales of days.

The technical problem is then to initialize the model with hydrographic measurements of small-scale eddies over a limited area of the Gulf (slope), and at the same time also account for the large-scale eddy field. It is noted that the scales of the slope eddies in Figure 4.1-1 are not, at present, well resolved by satellite altimetry. The north-central Gulf slope during two periods of the LATEX C and GulfCet observations (Hamilton et al., 2003): (A) December 3-14, 1993 and (B) December 16-23, 1993, will be the focus of this work. The scientific problem is therefore, given the slope eddy field, what can be deduced about its evolution? An attempt is made to address this problem using model simulations with and without data assimilation.

4.2 Observations

The measurement locations during the two observational periods (Period A and Period B) are shown in Figure 2.2-2. The corresponding 200-m sigma-t, the 200 to 780-m dynamic height and 200 to 780-m geostrophic velocity are shown in Figures 4.2-1, 4.2-2 and 4.2-3, respectively. Period A is characterized by a series of anticyclonic and cyclonic eddies spanning from west to east over the northern slope of the Gulf. The northern portion of an LCE can be seen from 92°W ~ 90.5°W. The magnitude of the 200 m geostrophic velocity (relative to 780 m) is about 0.25 m s^{-1}. Period B is over the north-central slope only from 94.5°W ~ 90.2°W. This region will be the primary focus of the model analyses (below). When comparing with Period A, it is clear that the

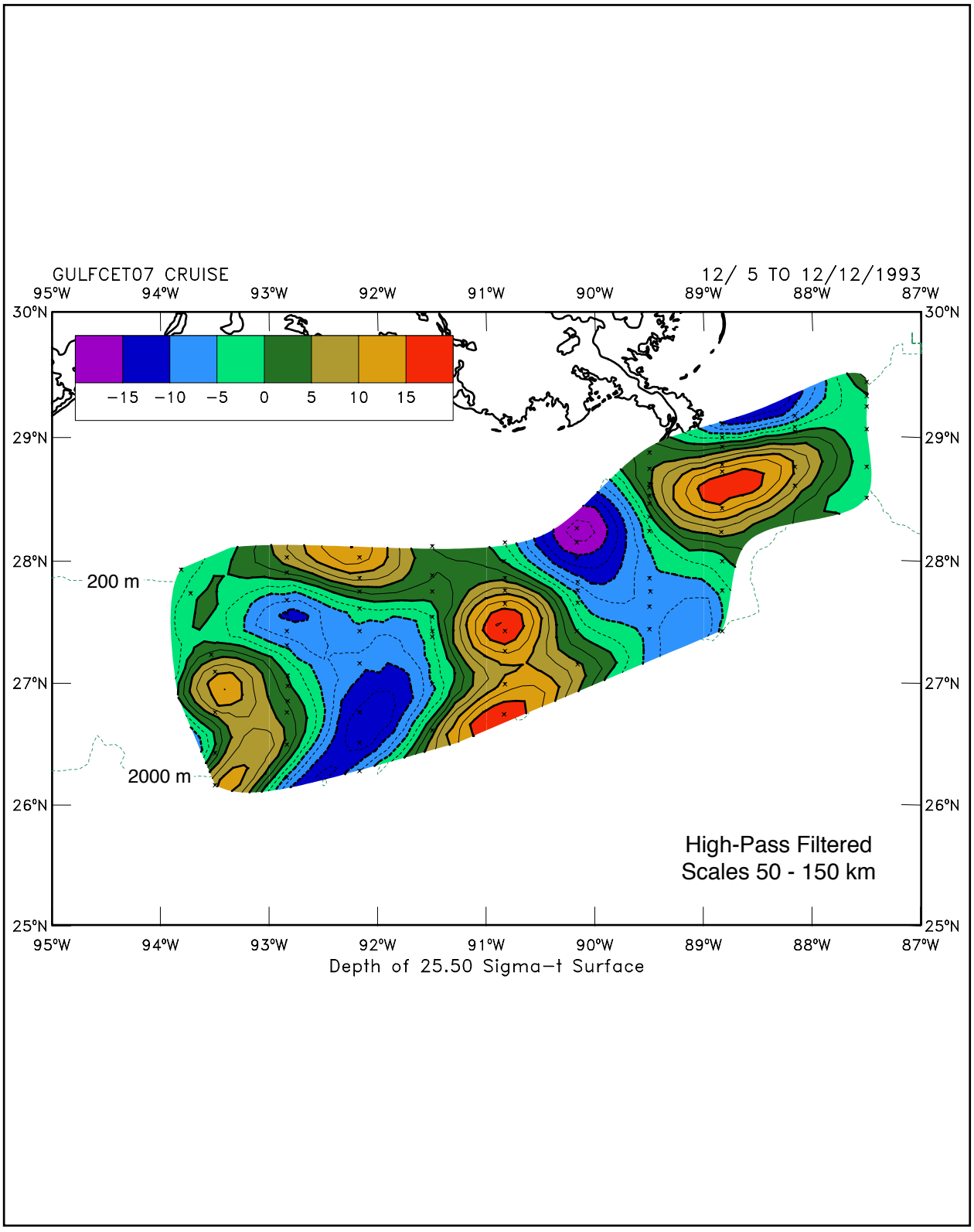

Figure 4.1-1. Depth of the 25.50 sigma-t surface (i.e. the main pycnocline) during the observation period December 5-12, 1993; high-pass filtered to remove scales larger than about 150 km.

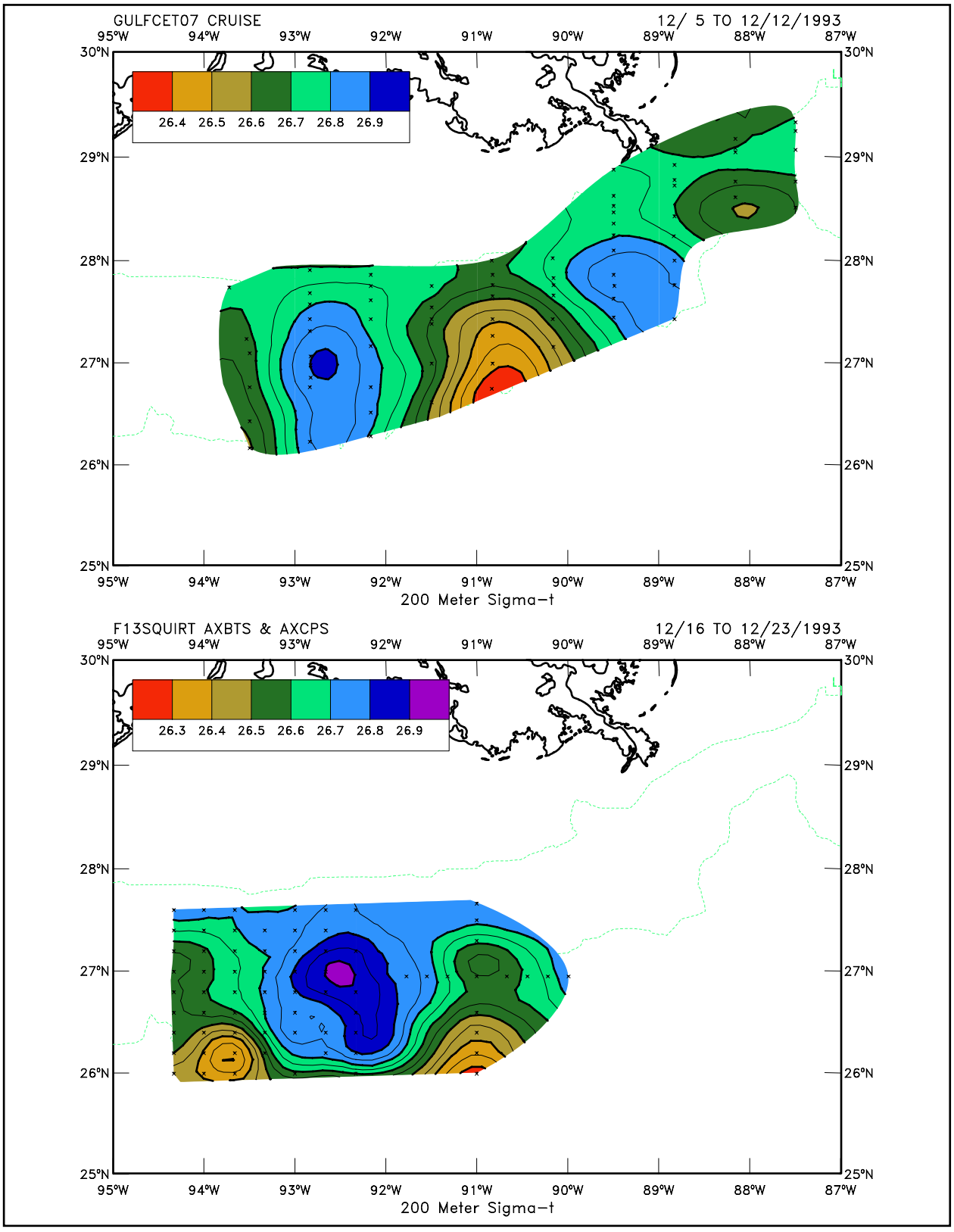

Figure 4.2-1. The 200-m sigma-t during the two observational periods (A) December 5-12, 1993 (upper panel) and (B) December 16-23, 1993 (lower panel).

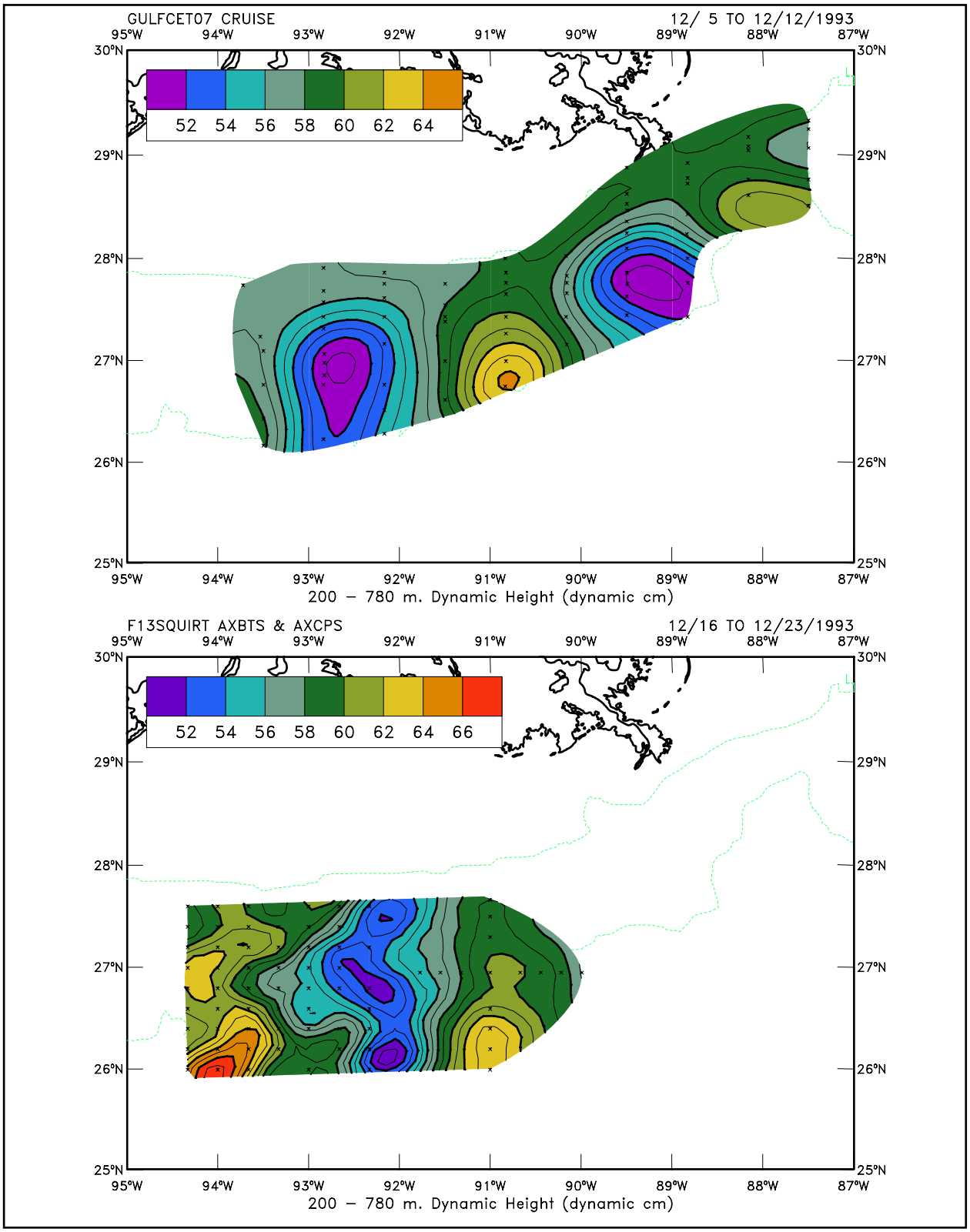

Figure 4.2-2. The 200 to 780-m dynamic height (dynamic cm) during the two observational periods (A) December 5-12, 1993 (upper panel) and (B) December16-23, 1993 (lower panel).

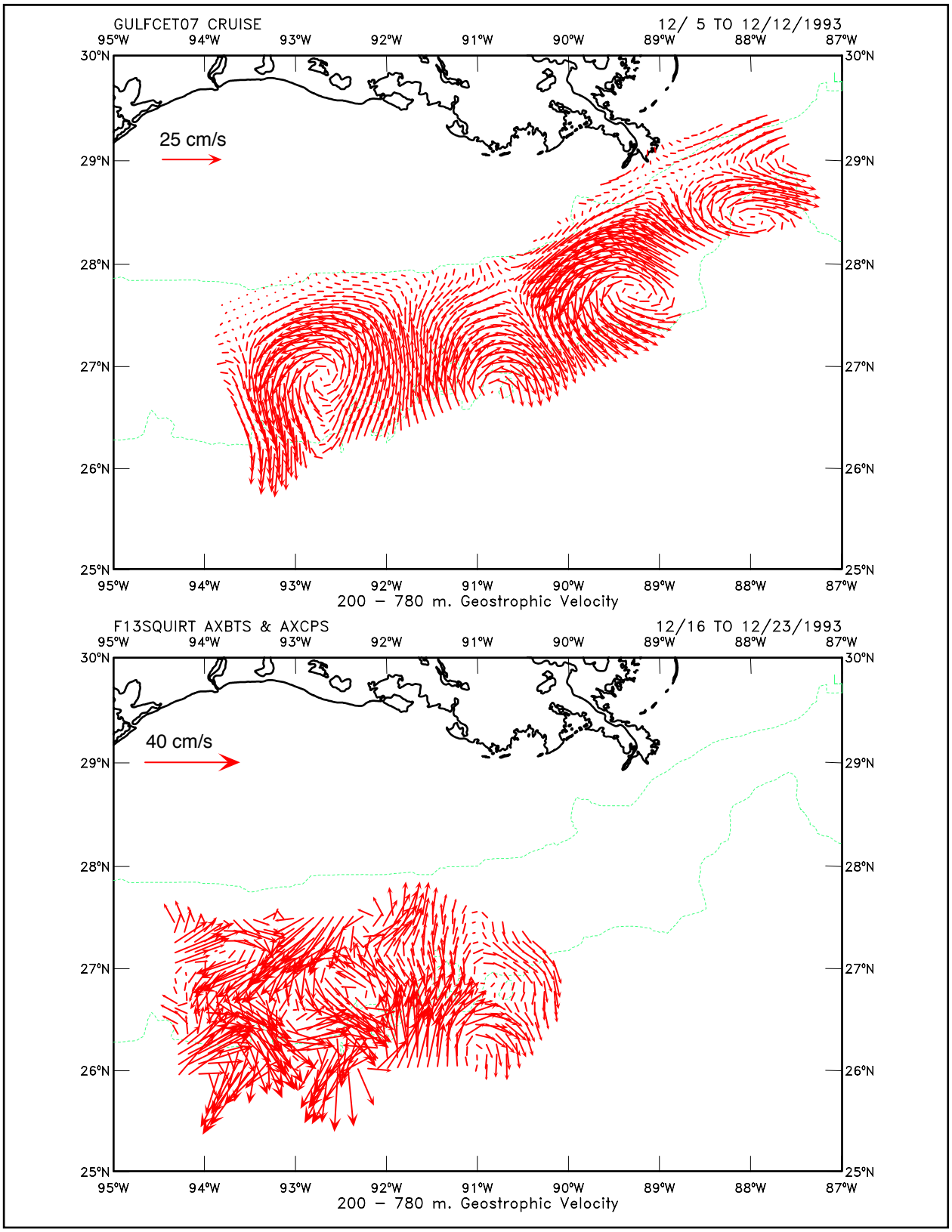

Figure 4.2-3. The 200 to 780-m geostrophic velocity during the two observational periods (A) December 5-12, 1993 (upper panel) and (B) December16-23/1993 (lower panel).

eddy field has evolved significantly during the intervening ~1 week period between Period A and B. The map of dynamic height (Figure 4.2-2) and the 200 m geostrophic velocity for Period B now show the appearance of smaller-scale features. The geostrophic velocities are some 70% more intense in Period B than Period A, and it is necessary to investigate how much of this change could arise from the differing resolutions of the two surveys.

The average influence radii of the statistical mapping method (Pedder, 1993) are 50 and 40 km for A and B, respectively. The cross-slope station spacing of the two surveys is very similar, so the main differences are in the along-slope spacing. The 200 m dynamic height field for the Period-B observations was re-calculated with an increased along-slope influence scale, so that the average influence scale was 50 km. The resulting geostrophic velocities were about 20% less in magnitude than those in Figure 4.2-3. Therefore, it is concluded that the increase in intensity of the eddy flows between periods A and B is real and not an artifact of the analysis method. Thus, one aspect of this study is the explanation of these changes through model-data analyses.

The hydrographic fields were prepared for assimilation by the model through use of the statistical, horizontal mapping scheme (Pedder, 1993) at 25 m depth intervals between the surface and 780 m. For each depth level, the station data were mapped to the model's curvilinear grid positions where they overlapped with the region of the survey. The horizontal area covered varies with depth because of the bottom slope. Hydrographic fields mapped to the model grid include temperature, salinity, sigma-t, and components of geostrophic velocity calculated relative to 780 dbars.

4.3 The Model

The model domain, topography and approximate grid distribution are shown in Figure 2.1-1a. Figure 2.1-1b also shows the nested Gulf of Mexico region where the grid resolution is doubled as described in Section 2.1. This section concentrates on the particular problem of initializing the model using observations from Period A, and on model evolution through Period B.

The model is initialized with climatological T/S and forced with six-hourly ECMWF wind beginning January 1, 1992. Satellite data-assimilation begins on October 22, 1992 and updated daily by interpolating between two 10-day base data. SST from the weekly AVHRR-MCSST dataset is also assimilated, but tests show that SST assimilation has little effects on the model solution (Wang et al., 2003). On December 3, 1993, hydrographic data (temperature) from observational Period A is 'injected' into the simulation. A simple nudging scheme is used for this purpose. Thus, the observed temperature T_o in the upper 780 m in the region shown in Figure 4.1-1 is used as a source term in the temperature equation:

$$DT/Dt = \partial(K_H \partial T/\partial z)/\partial z + F - \lambda(x,y,z,t)\,(T - T_o), \qquad (4.3\text{-}1)$$

where K_H is the vertical eddy diffusivity and F represents the horizontal mixing. λ is a nudging coefficient of the order of 1 day^{-1} that decays exponentially away from the (three-dimensional) observational region. λ also varies like a tanh function in time such that nudging is in full effect over a two-day transition, e.g. December 3 to 5, and returns to zero (i.e. is turned off) also in two days; December 12 to 14. In this way, the model is allowed to adjust to the observed

hydrography during the intervening interval (December 5 to 12) when the full nudging is in effect.

Nudging (or for that matter, any other more sophisticated assimilation scheme) amounts to introducing sources and sinks into model thermodynamics and dynamics. The situation is difficult in the present case since the data are neither continuous in time nor in space. The method works only if the initial model field (before nudging) approximates the observed conditions. Figure 4.3-1 shows the model sea-surface height (SSH) on December 3, 1993, and represents the model's best estimate of the observed conditions just prior to the hydrographic measurements. This can be compared with the observed dynamic height in Figure 4.2-2. Both figures show an anticyclone at 90~91°W and a cyclone to the west at 92~93°W. The model SSH shows another anticyclone further west around 94°W. Observations did not cover this western region but the eastern arm of the anticyclone can be seen. The upshot is that the model mimics quite well the observed conditions during Period A.

4.4 Model Prediction of Observational Conditions during Period B

After the above initialization of the T/S fields, the satellite data-assimilation was turned off and the model was allowed to evolve according to its own dynamics. This unassimilated, prognostic run continued from December 14, 1993 through January 1,1994.

Figure 4.4-1 shows the observed geostrophic velocities at 200 m during the two intervals (left panels) and compares them with the modeled velocities (right panels) on December 14 (at end of nudging), December 23 (at end of observation Period B during the unassimilated run) and January 1, 1994 (at end of unassimilated run). The observations show increased current intensity and meanders from Period A to Period B as was noted earlier in Figures 4.2-1-4.2-3. The model also shows a similar increase. Figure 4.4-2 indicates these increases more clearly with vertical sectional contours of the along-slope velocities and temperature at the cross-slope transect that cuts across the cyclone as shown in Figure 4.4-1. Observations show an increase of eastward velocity from 0.2 m s^{-1} during Period A to 0.8 m s^{-1} during Period B and westward velocity from –0.1 m s^{-1} to –0.3 m s^{-1}. Note that these geostrophic velocities are relative to an assumed level of no-motion of 780 m. The increases occur mostly in the upper layers but are also significant at depth. The model also shows increases, from 0.4 (–0.4) m s^{-1}, on December 14, to 0.8 (–0.8) m s^{-1} on December 23. A close examination of the density field (temperature in Figure 4.4-2, and others not shown) indicates more small-scale (~50 km; but resolvable by the model grid) structures during Period B. Because of the similarity of the model fields and their behaviors to the observations, the energetics of the model were investigated further.

4.5 Flow Energetics

Each flow variable is separated into its time mean and fluctuation (perturbation), $u = \bar{u} + u'$, $v = \bar{v} + v'$, $\rho = \bar{\rho} + \rho'$ etc., where the over bar denotes some appropriate time mean to be defined

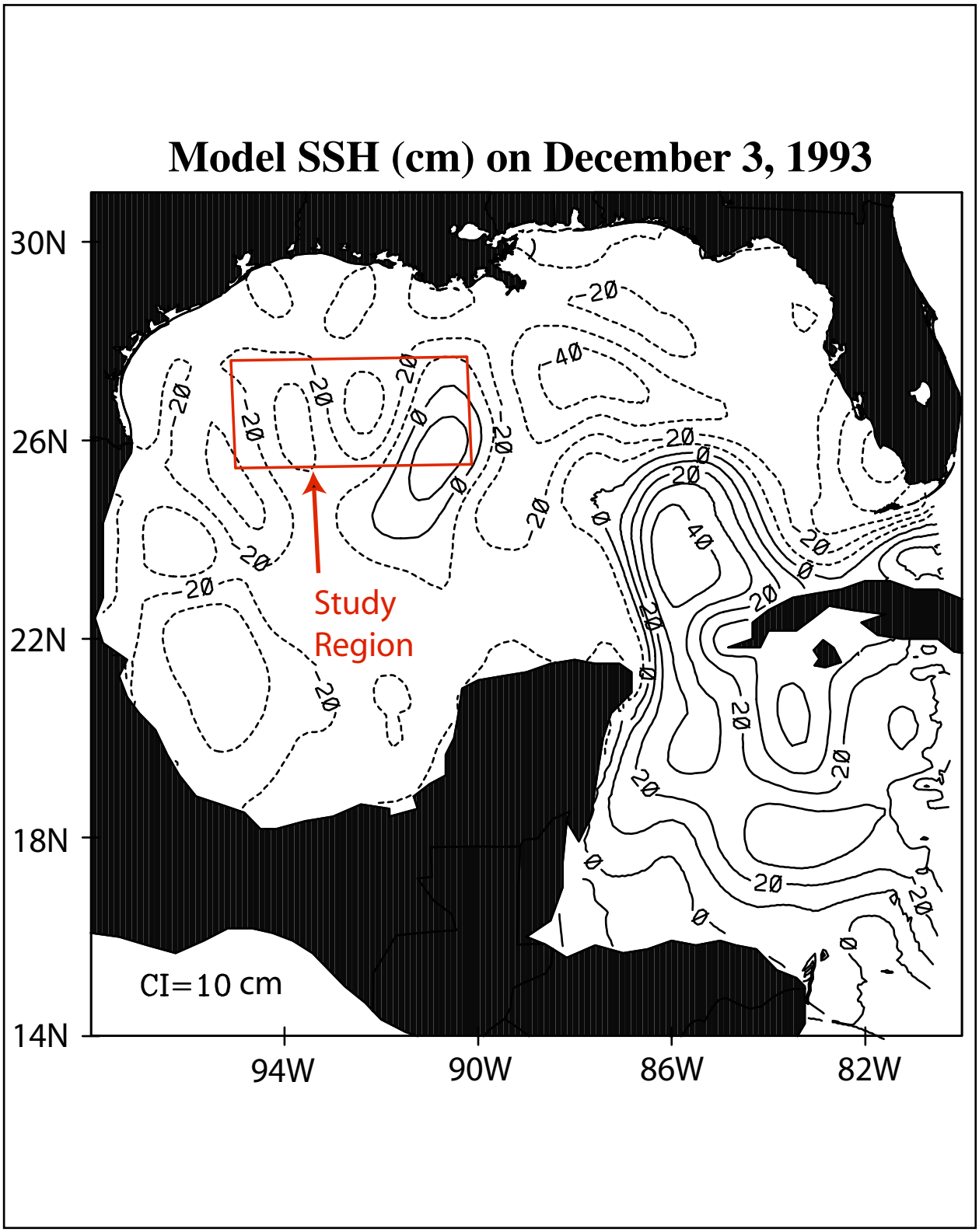

Figure 4.3-1. The model sea-surface height (SSH) just prior to nudging of hydrographic measurements from observational Period A. The study region is shown in the rectangle.

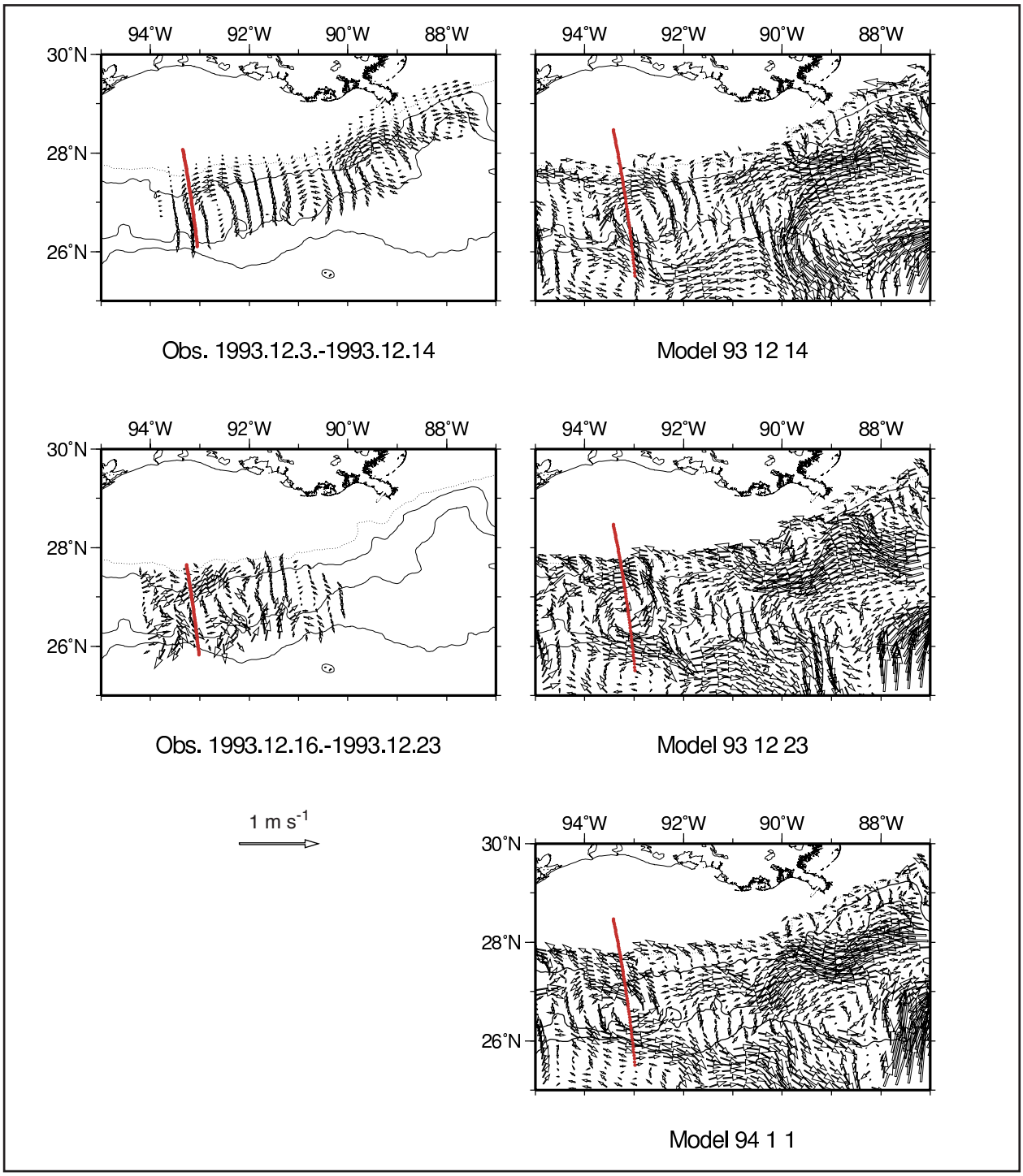

Figure 4.4-1. The observed geostrophic velocities at 200 m during the two periods (left panels), and the modeled velocities (right panels) on December 14 (at end of nudging), December 23 (at end of observation Period-B during the unassimilated run), and January 1, 1994 (at end of unassimilated run). The vector scale is 1 m s^{-1}. Contours are the 500 (dotted), 1,000, 2,00 and 3,000-m isobaths. The line across the cyclone near 93.5°W indicates the transect where variables are analyzed in more details (see Figure 4.4-2, also the text).

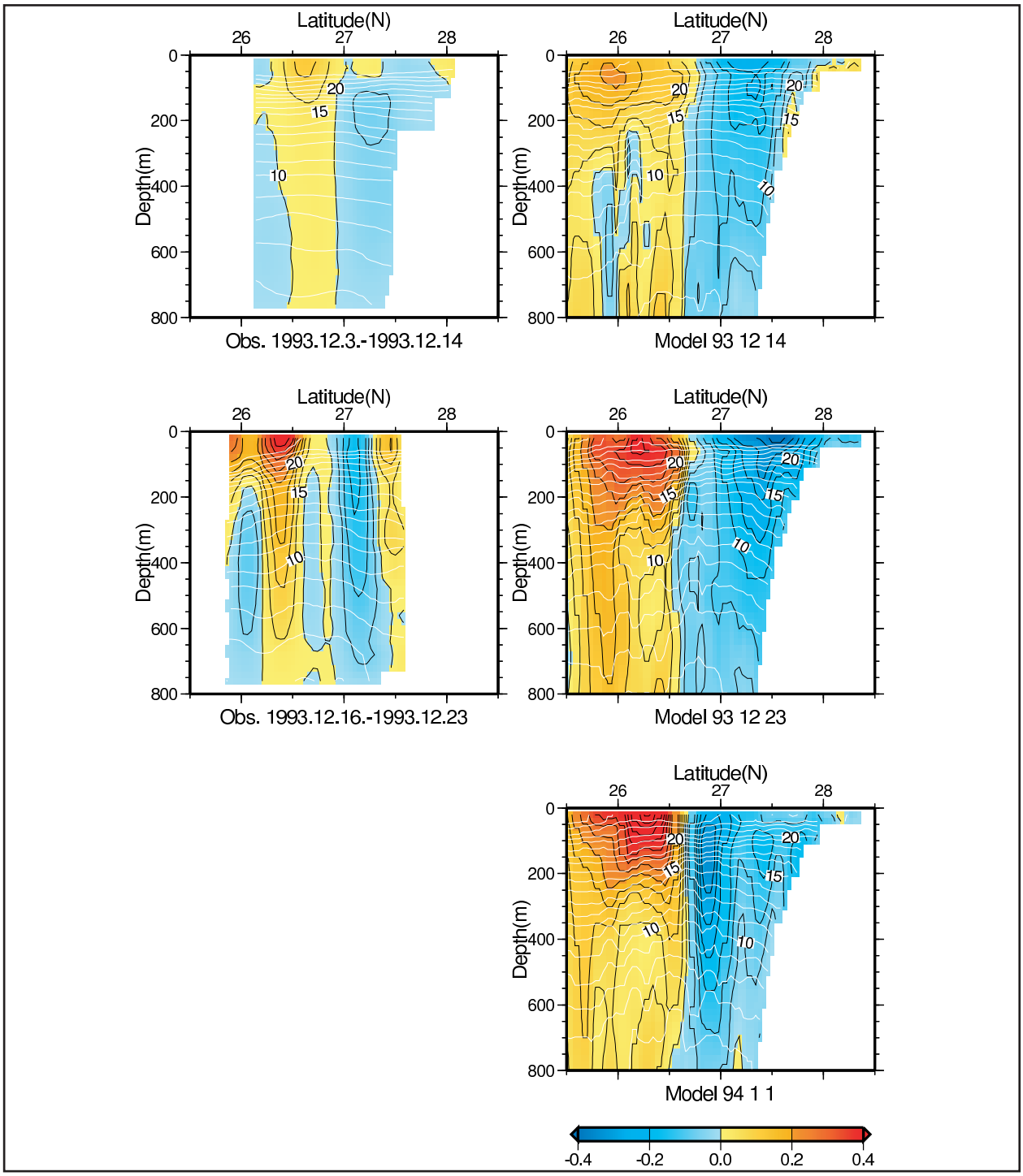

Figure 4.4-2. Left panels: the observed along-slope geostrophic velocities, U (colored, m s^{-1}) and temperature (light contours, °C) at the cross-slope vertical section shown in Figure 4.4-1, during the two indicated observational periods. The view is towards west so that positive U indicates eastward flow. Right panels: the corresponding modeled along-slope velocities on December 14 (at end of nudging), December 23 (at end of observation Period B during the unassimilated run) and January 1, 1994 (at end of unassimilated run).

shortly. The total (i.e. potential + kinetic) perturbation energy equation is then (Orlanski and Cox, 1972; Brooks and Niiler, 1977):

$$\frac{d}{dt}\{\frac{1}{2}(\overline{u'^2}+\overline{v'^2})+\frac{g^2}{2N^2}\frac{\overline{\rho'^2}}{\rho_0^2}\} = -\nabla\cdot(\overline{\vec{v}'p'}/\rho_0)-(\overline{u'^2}\frac{\partial\bar{u}}{\partial x}+\overline{v'^2}\frac{\partial\bar{v}}{\partial y}+\overline{u'v'}\frac{\partial\bar{u}}{\partial y}+\overline{u'v'}\frac{\partial\bar{v}}{\partial x})$$
$$-(\frac{g^2\overline{u'\rho'}}{\rho_0^2N^2}\frac{\partial\bar{\rho}}{\partial x}+\frac{g^2\overline{v'\rho'}}{\rho_0^2N^2}\frac{\partial\bar{\rho}}{\partial y})-(\overline{w'u'}\frac{\partial\bar{u}}{\partial z}+\overline{w'v'}\frac{\partial\bar{v}}{\partial z}). \qquad (4.5\text{-}1)$$

The various symbols are standard, i.e. g is acceleration due to gravity, N the Brunt-Väisälä frequency, etc. Equation (4.5-1) may be written symbolically as:

$$\frac{d}{dt}(EKE+PEP) = -\nabla\cdot(\overline{\vec{v}'p'}/\rho_0)+BT+BC+KH. \qquad (4.5\text{-}2)$$

Here, *EKE* is the kinetic energy of the perturbation (often referred to as the eddy kinetic energy) and *PEP* is the potential energy of the perturbation. The *BT* is the barotropic conversion term that, if positive, drains energy from the mean horizontal shears to the eddy field. The *BC* is the baroclinic conversion term that, if positive, drains energy from the mean available potential energy field (i.e. horizontal density gradients) to the eddy field. The *KH* is the Kelvin-Helmholtz instability term that depends on the mean vertical shears and Reynolds stresses in the vertical plane. Thus, both the *BT* and *KH* can release (if positive) the mean kinetic energy, while *BC* (if positive) can release the mean potential energy. The pressure work term on the right side of equation (4.5-2) (or 4.5-1) would vanish if integrated over a section with side-walls. In the present case this is not true (see below). There is also an exchange term, *PKC*, that appears with opposite sign on the right side of the separate equation for *EKE* and *PEP*:

$$PKC = -\frac{g}{\rho_o}(\overline{\rho'w'}). \qquad (4.5\text{-}3)$$

A positive *PKC* drains energy from *PEP* and into *EKE*, and vice versa for a negative *PKC*.

The individual terms in equation (4.5-1) were computed, using six-hourly averaged model fields from December 15 through December 30 at the cyclone section shown in Figure 4.4-1, as follows. Each of the terms is assumed to evolve with a fast time "t" when significant perturbation growth (or decay) occurs, and a slow time "εt" ($\varepsilon << 1$; i.e. long period) over which time averaging can be meaningfully defined. This long period is taken to be 5 days, i.e. the overbar $\overline{(.)}$ is for 5 days. Thus, each of the terms in equation (4.4-1) evolves slowly with a time scale of O(εt), and we can examine how they vary in the intervening 15 days after the observation Period A.

Figure 4.5-1 shows the sectional averaged (section length = L_y) *EKE* and *PEP*, $\int (EKE)dy / L_y$ and $\int (PEP)dy / L_y$, respectively, as functions of depth (z; m) and time (εt; days). For reasons that will become clear later, the section is taken as spanning the northern half of the cyclone (i.e. over the slope; Figure 4.4-1) only. Large eddy energies are mostly in the upper 300 m of the water column. A thin layer (~30 m) near the surface has particularly large energy, especially *EKE*, that is due to the eddy stirring by the wind. From December 15 through around December 20, there is a clear increase in both the *EKE* and *PEP*. This coincides with the observed increase in current intensity and 'meander' activity from Period A to Period B (Figures 4.2-1 to 4.2-3). Thereafter there is a general decline in *PEP,* but a second increase in *EKE* occurs around December 25.

Figure 4.5-2 shows the time-averaged (period P = 15 days from December 15 to 30) *EKE* and *PEP*, $\int (EKE)dt / P$ and $\int (PEP)dt / P$, respectively, as functions of depth (z; m) and latitude at the cross-slope section shown in Figure 4.4-1. Once again the concentration of eddy energy in the upper 300 m is clearly seen, however, the *EKE* appears to penetrate deeper than the *PEP*. Apart from the wind-induced eddy energy in the very near-surface layers, most of the subsurface eddy energy appears in more offshore regions (27°N~27.25°N), where the depth of water is approximately 1,000 m or greater.

The terms in equations (4.5-2) and (4.5-3) were averaged over *y* as well as *z*, e.g., <*EKE*> = $\int_{-H}^{-50m} \int (EKE)dydz /(250L_y)$, where <.> denotes the double-averaging, where the averaging over depth excludes the near-surface wind-forced layer. The conclusions below are not changed by this choice. Figure 4.5-3a shows plots for the individual terms as a function of time. In this figure, the <*EKE Source*> = <*BT*> + <*KH*> + <*PKC*>, while <*PEP Source*> = <*BC*> – <*PKC*>; i.e. they are the source terms (except for the pressure work term which also appears in the equation for *EKE*) in the *EKE* and *PEP* equations respectively. The Kelvin-Helmholtz term, <*KH*>, is weak (note change in its scale) throughout the whole period. It is clear that from December 15 through 20, there exists both barotropic and baroclinic instabilities, but the latter dominates. There is a transfer of energy from *PEP* to *EKE* during this period, i.e. <*PKC*> is positive. This suggests that the observed increases in the intensity of the geostrophic velocity and meanders from Period A to Period B may be a result of mixed barotropic and baroclinic instabilities. During the middle period, December 20 through 25, there are only weak energy exchanges, between <*EKE*> and <*PEP*>, or between the eddy and mean energies. At later times, December 25 through 28, the instability appears to be barotropic. The <*PKC*> is negative, and there is a transfer of <*EKE*> to <*PEP*>. However, the flow appears to be baroclinically stable (<*BC*> is negative) as the cyclone moves off-slope (Figure 4.4-1).

The northern half of the cyclone is situated over the sloping topography (Figures 4.4-2 and 4.5-2), which should be destabilizing because the slope and isopycnals are of opposite signs. It is expected that analysis of the southern half might yield different results, which are shown in Figure 4.5-3b. Here <*BC*> is predominantly negative (except for the small values near the beginning), and there is a drain of <*PEP*> to <*EKE*> (i.e. <*PKC*> is positive). However, despite <*BT*> that is also positive (albeit small), the <*EKE*> actually decreases. A more detailed analysis

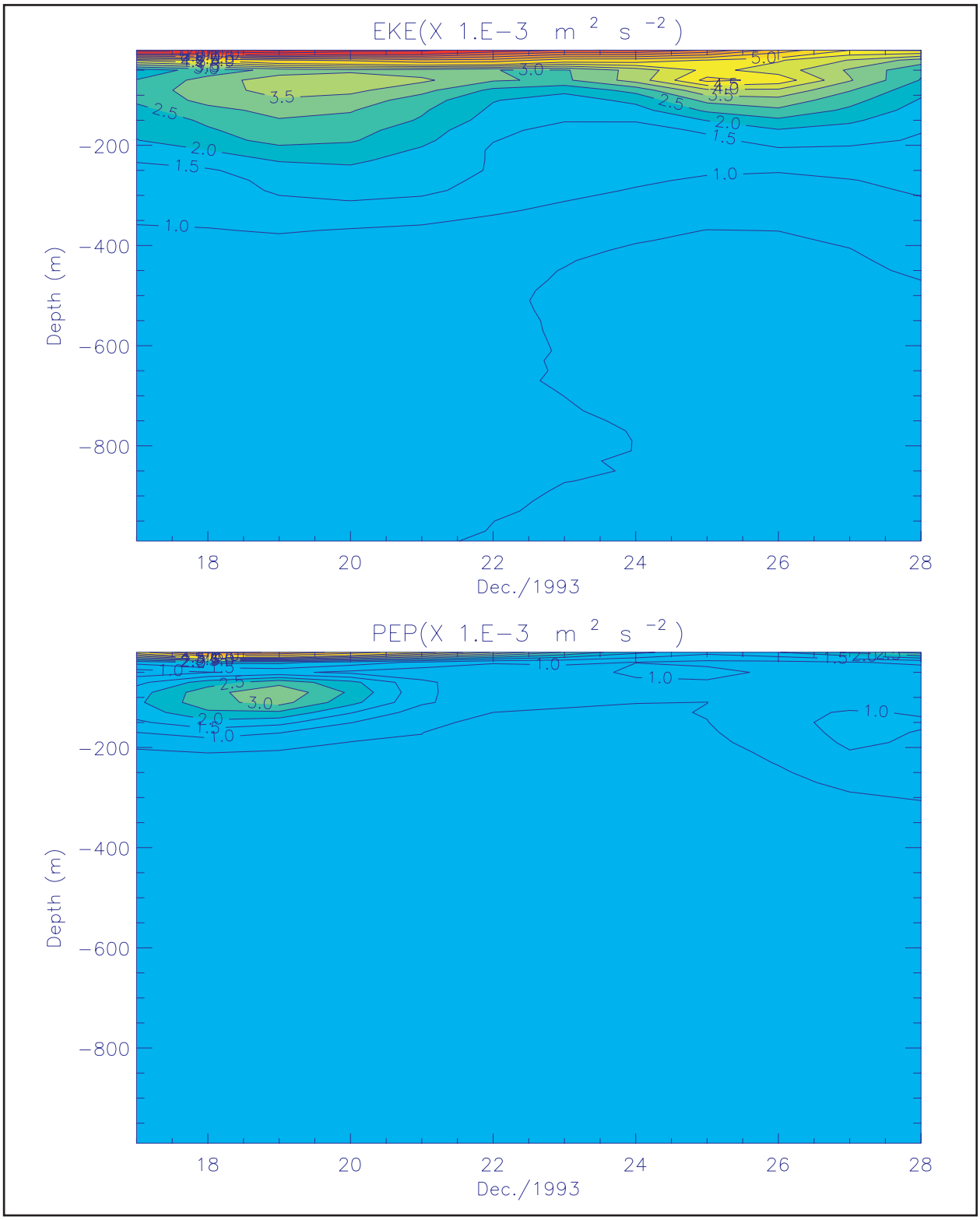

Figure 4.5-1. The sectional averaged (section length = L_y, where the section is the northern half of the cyclone shown in Figure 4.4-1) *EKE* and *PEP*, $\int (EKE)dy / L_y$ (upper panel), and $\int (PEP)dy / L_y$ (lower panel), respectively, as functions of depth (z; m) and time (εt; days).

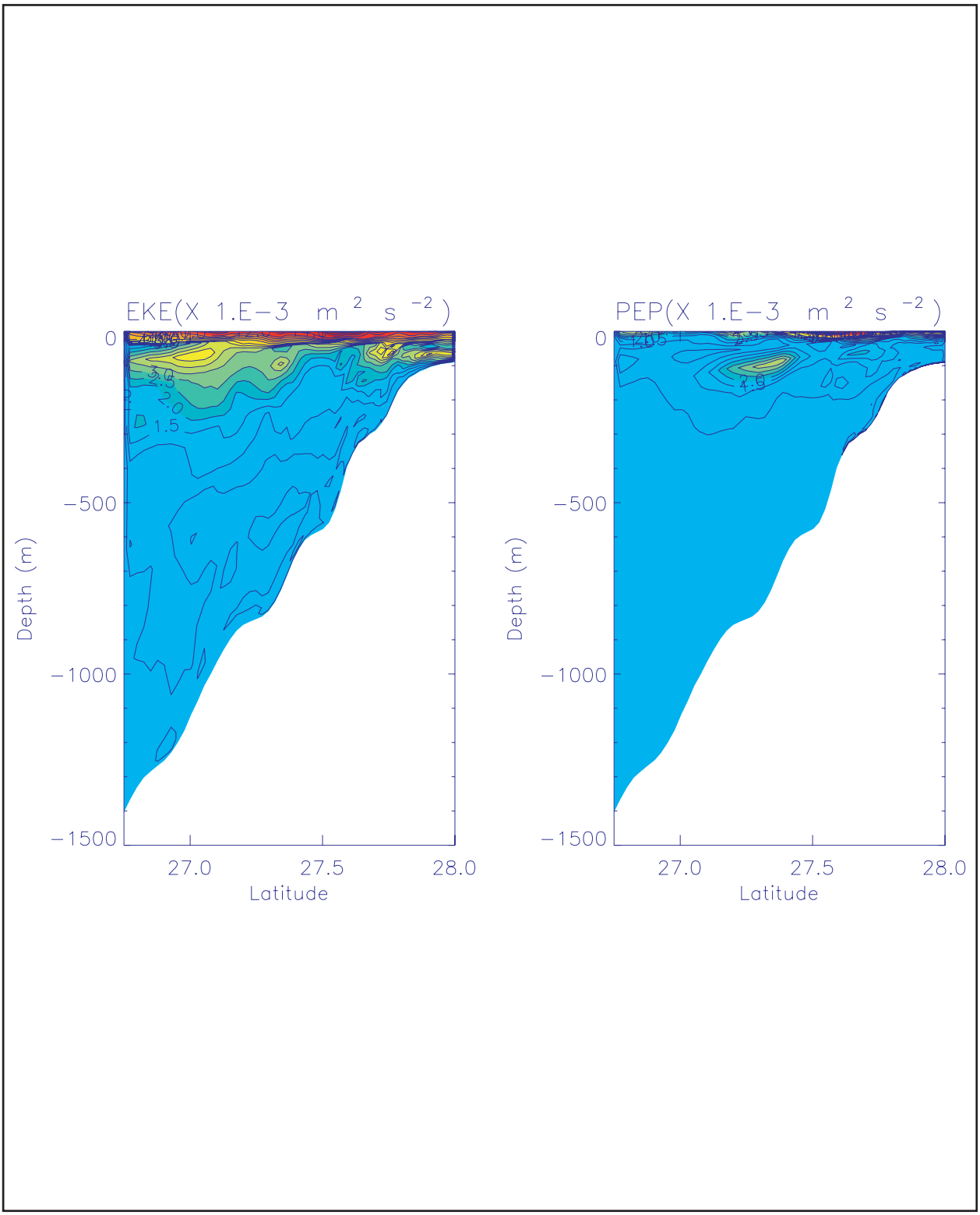

Figure 4.5-2. Time-averaged (period P = 5 days from Dec 15th-30th) *EKE* and *PEP*, $\int (EKE)dt / P$ (upper panel) and, $\int (PEP)dt / P$ (lower panel), respectively, as functions of depth (z; m) and latitude for the northern half of the section cutting across the cyclone shown in Figure 4.4-1.

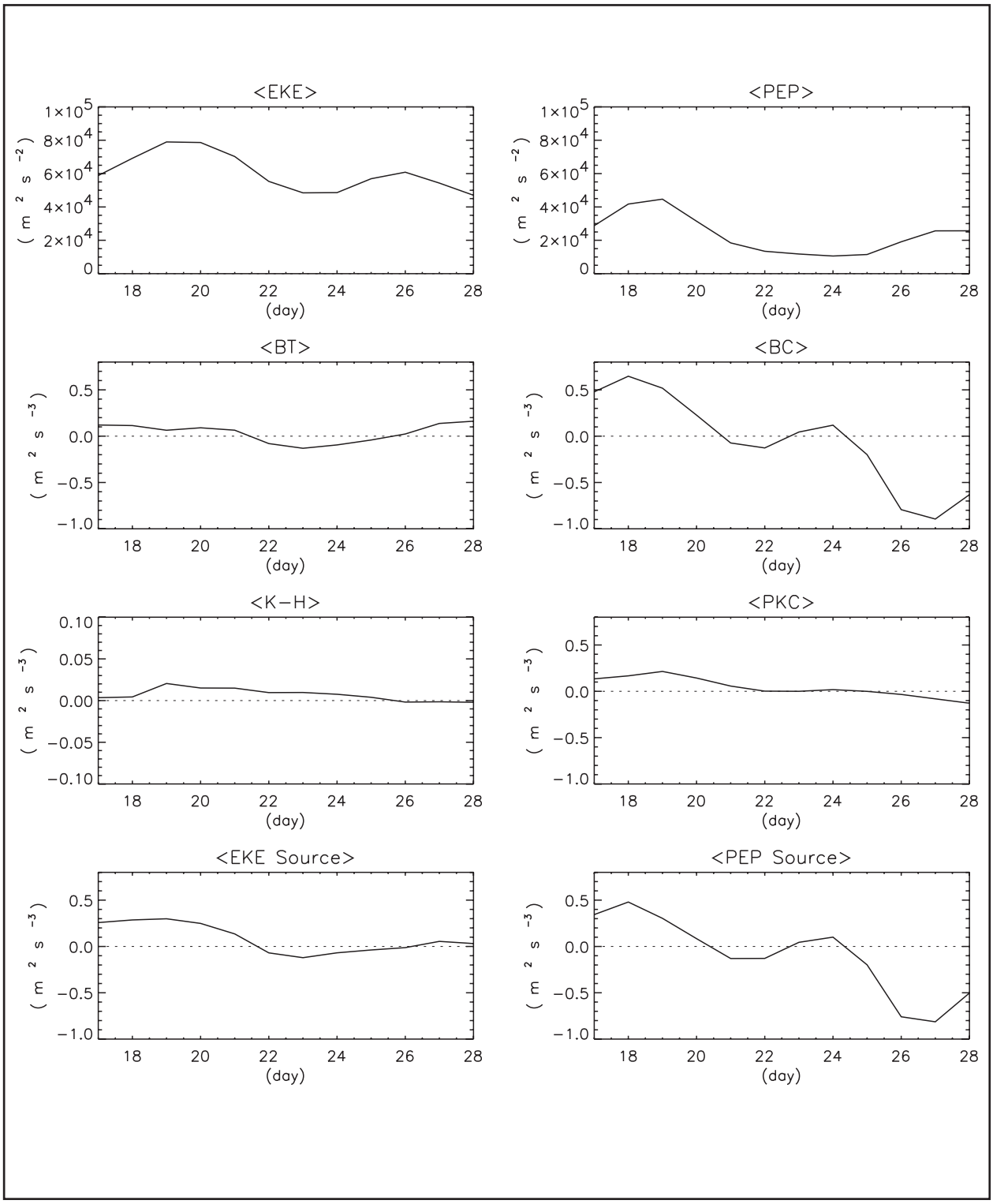

Figure 4.5-3a. Sectional (y) and depth (z = -H to -50 m) averaged values of the terms in equations (4.5-2) and (4.5-3). The section is over the northern half across the cyclone as shown in Figure 4.4-1. The *<EKE Source>* = *<BT>* + *<KH>* + *<PKC>*, while *<PEP Source>* = *<BC>* - *<PKC>*. Note that *<KH>* is small and its scale is magnified by almost a factor of ten. See text for details.

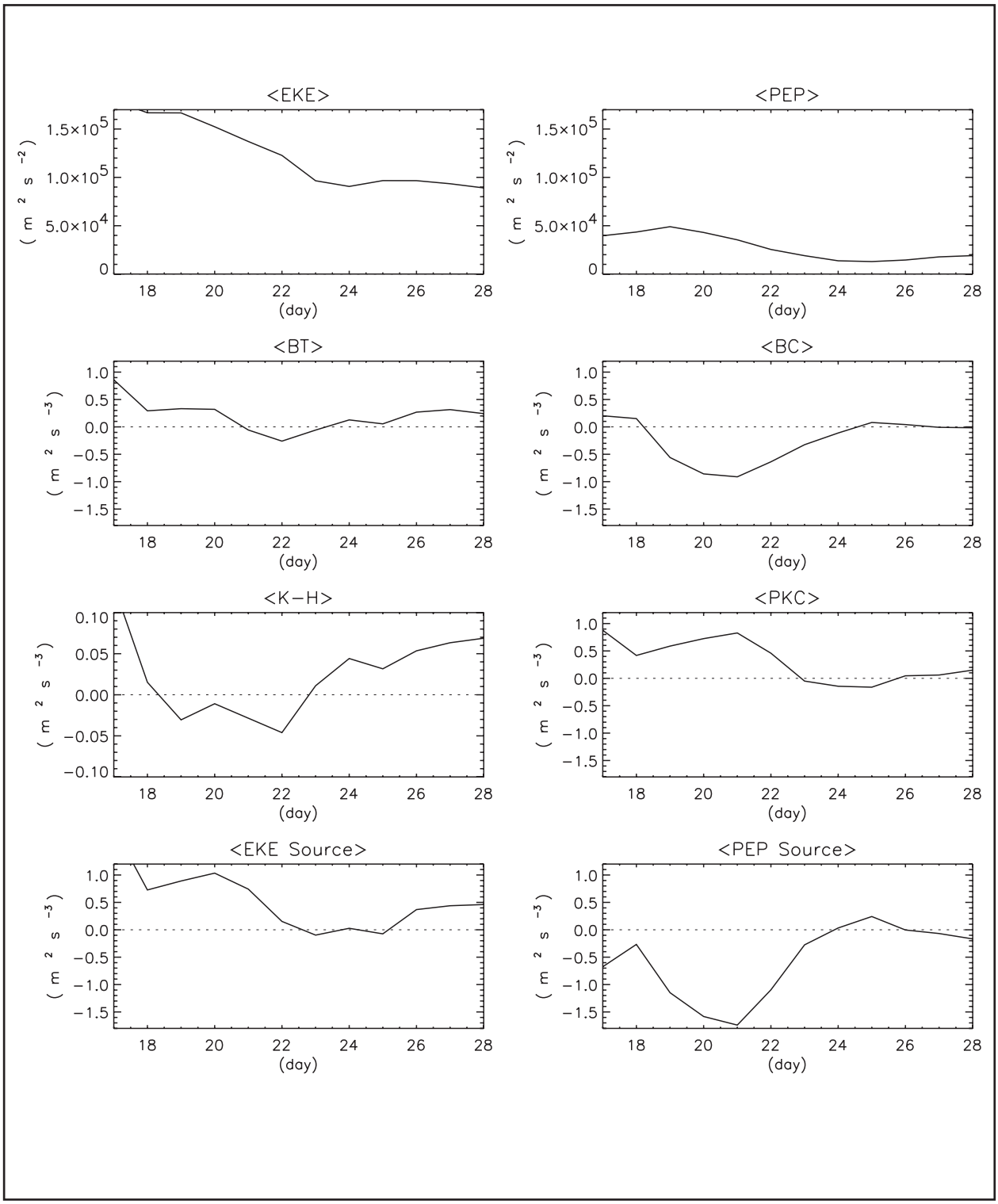

Figure 4.5-3b. Sectional (y) and depth (z = -H to -50m) averaged values of the terms in equations (4.5-2) and (4.5-3). The section is over the southern half across the cyclone as shown in Figure 4.4-1. The *<EKE Source>* = *<BT>* + *<KH>* + *<PKC>*, while *<PEP Source>* = *<BC>* - *<PKC>*. Note that *<KH>* is small and its scale is magnified by almost a factor of ten. See text for details.

reveals that the pressure work term: $-\int\int \nabla\cdot(\overline{\vec{v}'p'}/\rho_0)dydz$ is not insignificant and there is a 'leak' of eddy energy through the offshore end of the section.

The higher-order hydrographic analyses, given in Section 2.3.2, confirm the development of the instabilities between Periods A and B. For Period A, Figure 4.5-4 shows the Sverdrup and Ertel PV of the surface layer, which is essentially inversely proportional to the depth of the 26.5 sigma-t surface, overlaid with the geostrophic velocity field on the 25.5 sigma-t surface. The later is a marker for the center of the pycnocline. By comparing the PV fields, it is apparent that the relative vorticity is an important component of the PV and serves to homogenize the PV within eddies, and sharpen the gradients between them. This is not unexpected if the centers of eddies are almost in solid body rotation. The strongest geostrophic velocities approximately follow the contours of constant (Ertel) PV, though there are significant PV perturbations, with about a 50 km scale, along the paths of strongest velocities that indicate incipient meanders. For example, along ~ 92°W and ~ 93°W, or the boundaries traced out by the 0.8 and 0.1 x 10^{-9} s^{-1} contours in the lower panel of Figure 4.5-4. The same PV plots (Figure 4.5-5) for Period B shows that: (1) the relative vorticity has increased relative to the Sverdrup PV, (2) the geostrophic flow field is more chaotic, though the basic eddy structures are identifiable from Figure 4.5-4, and (3) the (Ertel) PV perturbations, along the paths of the largest geostrophic velocities, have increased in amplitude (e.g. east and west of the cyclone centered ~ 92.5°W). Even though the calculation of ζ in the Ertel PV (Equation 2.3-12) is inherently noisy for observational data, it is considered that the increases in activity between Periods A and B in the PV maps are significant even if all the details cannot be relied upon.

The Q-vector divergence was calculated for the 200 m depth level, which is at about the deepest descent of the 26.5 sigma-t surface, i.e., just below the pycnocline layer (Figure 4.5-6). Positive and negative Q-vector divergence roughly corresponds to upwelling and downwelling, respectively, and again is an inherently noisy calculation involving horizontal gradients of geostrophic velocity and sigma-t. The Period A map shows alternate patches of divergence and convergence around the peripheries of the eddies where the velocities are largest. If a streamline, corresponding to the position of the strong currents, is followed around the cyclone situated between 92 and 94°W, then as the flow enters a region of increasing PV (Figure 4.5-4), there is a tendency to encounter a region of positive divergence or upwelling. Similarly, if the flow along a streamline enters a region of decreasing PV, there is a tendency for convergence or downwelling. If the Q-vector divergence map is compared with the 50-150 km filtered pycnocline depth in Figure 4.1-1, then, where the up- and down-welling are significant on the periphery of the eddies, has a rough correspondence to up (< 0) and down (> 0) displacements, respectively, of the pycnocline. This implies that the smaller scales embedded in the eddy field are directly linked to (or generated by?) the perturbations around the peripheries of eddies which are in turn a result of the instability processes as discussed above. The same kind of patterns are found in the Period B maps, but are much harder to discern because of the complexity of the flow field. The increase in perturbation energy between Periods A and B and the coupling of eddy scales to PV perturbations in regions of strong flow imply that small-scale eddies can develop rapidly over the northern slope and may account for the complexity of the mapped eddy fields discussed in Hamilton et al. (2003).

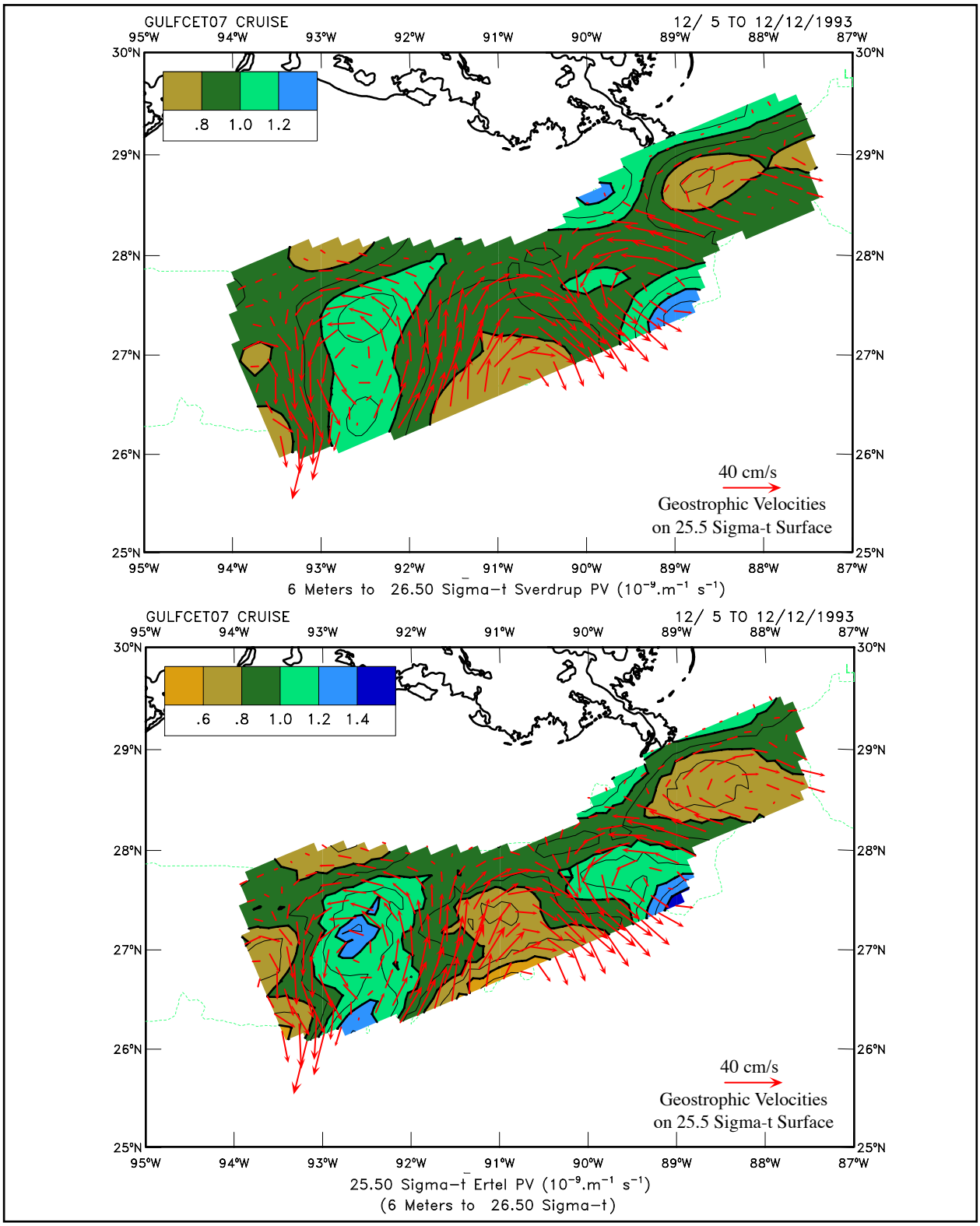

Figure 4.5-4. Sverdrup potential vorticity (PV) for layer between the near-surface and the depth of the 26.5 sigma-t surface (top panel) for Period A. The lower panel shows the Ertel PV for the same layer. Geostrophic velocities for the center 25.5 sigma-t surface are overlaid on both maps.

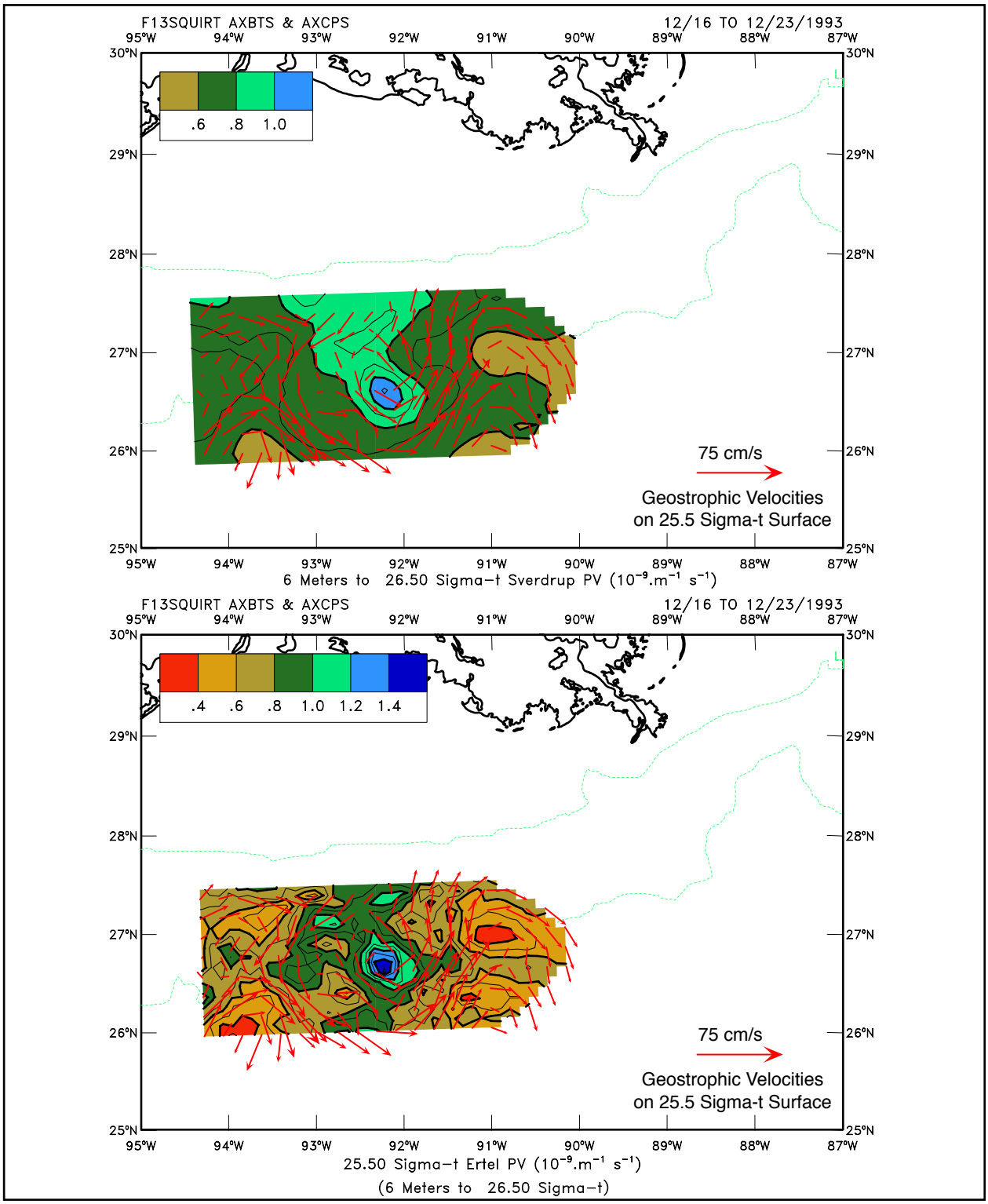

Figure 4.5-5. Sverdrup potential vorticity (PV) for layer between the near surface and the depth of the 26.5 sigma-t surface (top panel) for Period B. The lower panel shows the Ertel PV for the same layer. Geostrophic velocities for the center 25.5 sigma-t surface are overlaid on both maps. Note the change in velocity scale from Figure 4.5-4.

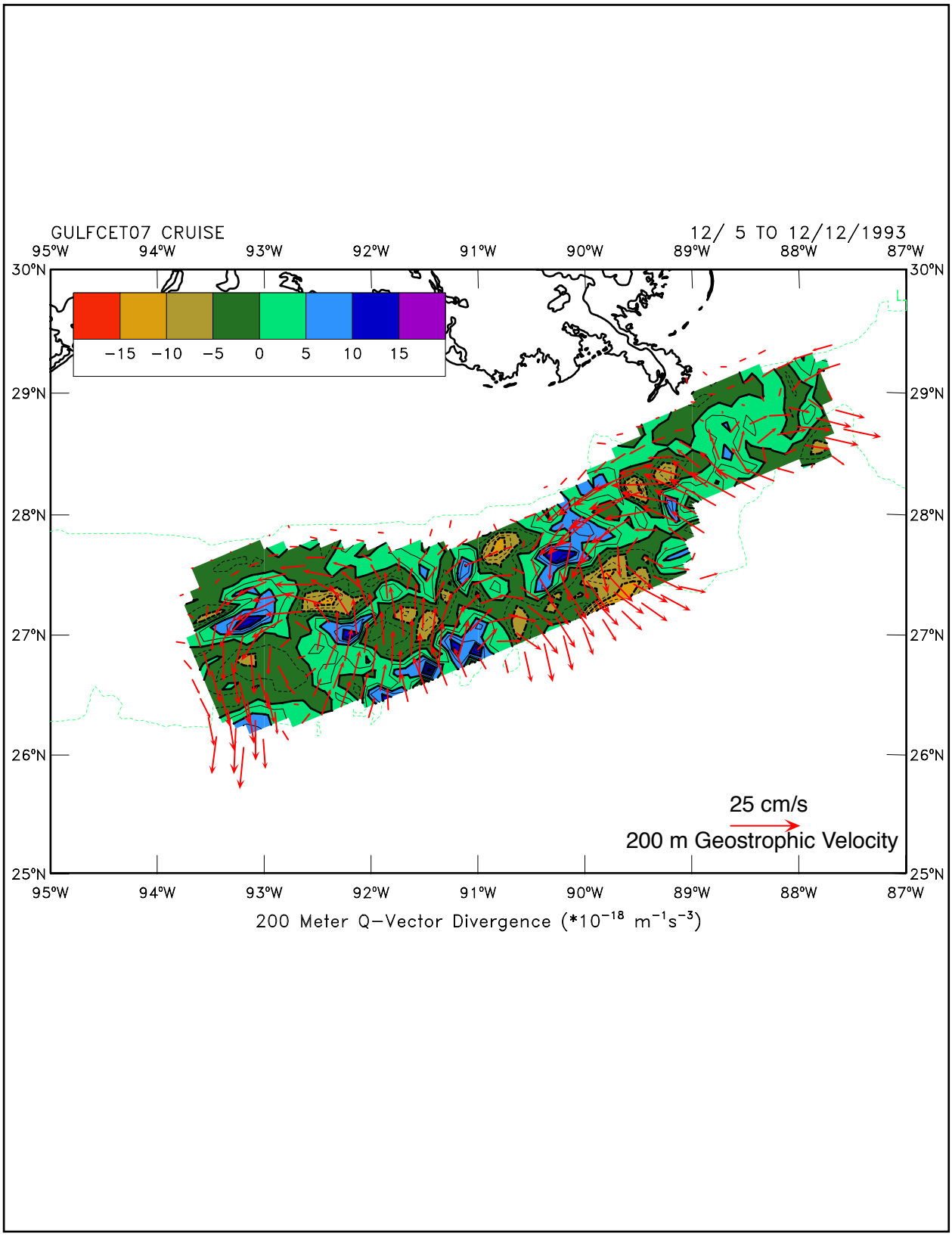

Figure 4.5-6. The Q-vector divergence at 200 m overlaid with the 200-m geostrophic velocity vectors for Period A.

In summary, it has been shown that high-resolution hydrographic measurements over the northwest central Gulf may be merged with a model field of currents and density assimilated with satellite SSH. Both observations and model show increased current intensity and 'eddy activity' (meanders) from Period A (December 5 to 12, 1993) to Period B (December 16 to 23, 1993). The latter period in particular shows a cyclone over the slope (Figure 4.2-1). The growth in current intensity from Period A to Period B was shown to be due to mixed barotropic and baroclinic instabilities, especially over the on-slope side of the cyclone where isopycnals and topography are of opposite signs. On the off-slope side the flow is stabilizing and there is a leakage of eddy energy through the fluctuating pressure work term.

5. Contributions to Other Studies

As part of the modeling and data investigations undertaken by this project, a number of contributions were made to other studies that were conducting research into model-data assimilation and physical circulation processes in the Gulf of Mexico. The purpose of this chapter is to provide summaries of this work as it has direct relationships with the assimilation studies reported above. The reader is referred to the appropriate journal papers for details of these ancillary studies, which include comparison of current data from the DeSoto Canyon Study with model simulations and satellite altimetry (Wang et al., 2003), the assimilation of surface lagrangian drifter data into the model (Fan et al., 2003), and an investigation into the mechanisms that contribute the irregular shedding of LCE's from the LC (Oey and Lee, 2002). These three topics are discussed below. Contributions were also made to a companion modeling study into the high-speed subsurface jet phenomena that was undertaken by S. DiMarco at Texas A&M University (TAMU). This work included providing POM output to TAMU, and analyzing output from the model runs, used by this project, for the occurrence of jets. This later contribution is discussed in TAMU's report (DiMarco et al., 2003), and so is not reported here.

5.1 DeSoto Canyon Comparison

This study evaluates a data-assimilated model simulation of near-surface circulation in DeSoto Canyon (DSC), Gulf of Mexico, with emphasis on analyzing moored current-meter observations and comparing them with satellite data and model results. The study period was for two years from April 1997 to April 1999 and a description of the data is given by (Hamilton et al., 2000). The model results are from a high-resolution Gulf of Mexico model forced by analyzed wind and surface heat flux that is described in Section 2.1. The assimilation of satellite observations of sea-level anomaly (SLA) and SST by the model used the techniques given in Section 2.1.1. Two types of data were used to deduce near-surface circulation: moored current meters at thirteen locations in the DSC (see Section 2.2), and satellite altimeter-derived, sea level anomaly. The moored currents were mapped through multivariate objective analysis to produce surface currents and surface geopotentials, against which satellite and model derived sea surface heights and geostrophic currents are compared. Coupled patterns between the observations, model results, and satellite data, were obtained using the Singular Value Decomposition (SVD) analysis that is outlined in Section 2.3.3. There were two dominant modes: a 'single-eddy' mode where currents were concentrated at the foot of the canyon and an 'eddy-pair' mode where one eddy was at the foot of the canyon and the other, a counter-rotating eddy, was over the head of canyon. Mode 1 appears to have been associated with the mesoscale eddy travelling around the Loop Current crest and trough, and mode 2 was associated with the intrusion of Loop Current crest and trough over the west Florida shelf. The observed and model currents are in good agreements about the means and variances. The model currents also appear to be well constrained by the steep topography. However, the model velocity field contains only the first mode. The satellite-derived velocity field, on the other hand, contains both the first and second modes; though, the satellite field does not adequately resolve the velocity structures over the slope.

The prediction of shelf edge currents in the DSC requires that the model must be able to represent realistically the LC and LCE's, and include the indirect stochastic effects of frontal

eddies. This study presents comparisons of the results from the high-resolution ocean prediction experiment, discussed in Chapters 3 and 4, with data from a comprehensive network of moored current meter observations. An ocean prediction system, in general, has three basic components: an observational network, a dynamical model, and a data assimilation scheme. In the Gulf of Mexico, satellite remote sensing of sea-level anomaly (SLA) and sea surface temperature (SST) provides the only basin-wide observational network. Results from a model experiment, which assimilates both satellite SST and SLA and is forced by ECMWF winds and surface heat fluxes, were used to compare the near-surface currents and sea surface heights derived from both the moored and satellite altimetry data. The study period was two years, covering several major eddy events. While the utility of satellite altimeter in mapping eddies in the open ocean has long been established, relatively little has been explored on assimilating altimeter data on the shelf edge. This study, with the DSC as an example, is a major step towards a better formulation of ocean prediction systems for shelf break and slope regions and complements the more recent studies with the slope hydrographic surveys that are given Chapter 4.

Model and observed mean currents and their corresponding variance (rms velocity) ellipses are shown in Figure 5.1-1. All observational data has been 15-day, low-passed filtered so as to be compatible with satellite SLA maps. Since the slope currents were dominated by eddies, such low-passed current observations contain 75 to 85% of the variance of the unfiltered daily data. Mean currents were eastward and their magnitudes were small (~5 cm/s) compared to the fluctuations (~15 cm/s). Both the means and variance ellipses tend to follow the bottom topography. The model mean currents are generally in good agreements with the observed currents, having the same general direction and comparable magnitude. However, the model means are much too strong (>10 cm/s) near the head of the canyon. The model variances also agree well with the observed, however, the model ellipses are narrower than the observations, suggesting that the model currents are more strongly constrained by the bottom topography.

SVD (Section 2.3.3) was used to extract patterns in the model currents that are coherent with observed currents (means removed). The conventions are that the left data field is assigned to observed currents and the right data field is assigned to model currents. The first mode alone explains 96% of the covariance between observed and model currents (that is, $SCF_1 = 0.96$), and the second mode explains 2%. The method captures almost the entire covariance structure in a single mode. Figure 5.1-2 shows the first and second spatial patterns of the observed and model currents. The mode 1 spatial patterns of observed and model currents are comparable in that both indicate a single-eddy structure located at the foot of the canyon. (The term "eddy" is used here to describe unidirectional flows over the shelf edge. Since the geostrophic flow was non-divergent, the unidirectional flow must somehow veer around the shelf edge, turning either cyclonic or anticyclonic.) Also, both the observed and model eddies appear to have been 'blocked' by the steep canyon wall. This shows that the model results contain a high degree of reality, as both the model and observed currents indicate similar spatial (and temporal; not shown) structures for the dominant fluctuations. The mode 2 spatial pattern consists of an isolated eddy at the head of the canyon, and the correlation (γ) between observed and model second modes is 0.51. The fractional variances explained by mode 2 are 10% and 12% respectively of the observed and model currents.

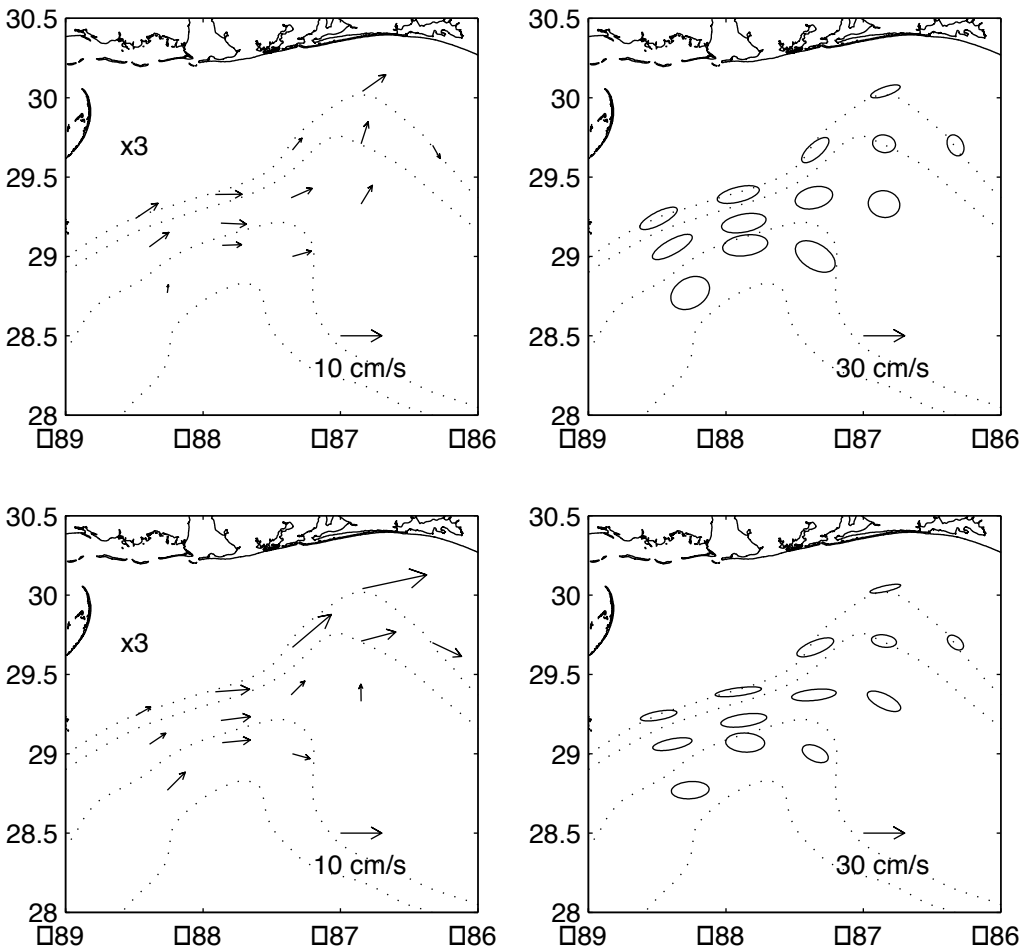

Figure 5.1-1. Mean currents (left) and variances (right) at mooring locations from observations (upper) and model (lower). Note that the velocity scale for means is 3 times larger. Dotted lines are isobaths at 2000, 1000, 200 and 100 m.

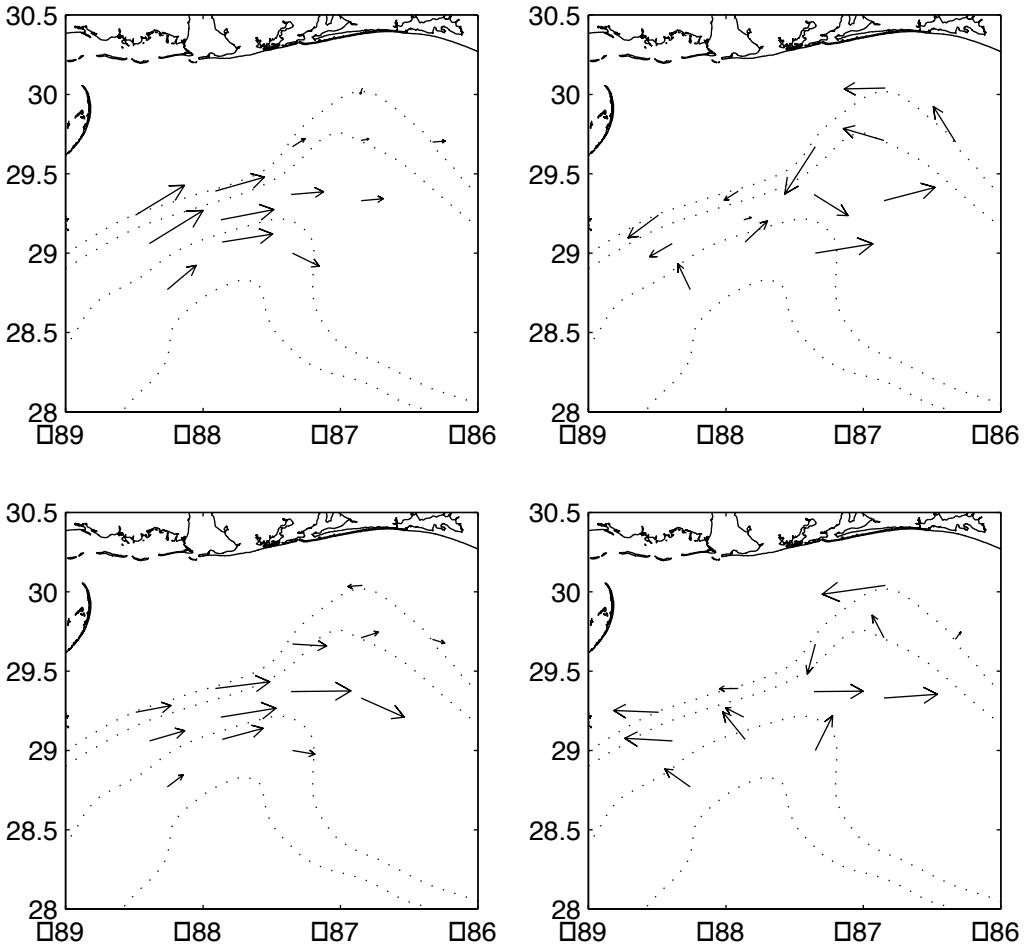

Figure 5.1-2. First (left) and second (right) spatial patterns of observed (upper) and model (lower) currents. The velocity scale is arbitrary. Dotted lines are isobaths at 2000, 1000, 200 and 100 m.

The observed currents were also compared with the geostrophic currents derived from satellite SLA. The 0.25^o x 0.25^o SLA data are first mapped onto the analysis grid, and SVD was used to find coupled patterns between observed and satellite-derived currents. The first modes of observed and satellite-derived currents are well correlated with $\gamma = 0.83$. The first spatial pattern (Figure 5.1-3) of observed currents is the same as in the earlier case, showing a single eddy confined to the deeper part of the canyon. The first spatial pattern of satellite-derived currents also indicates a single eddy; however, the eddy seems to penetrate well onto the head of the canyon. In other words, the satellite-derived currents were less constrained by the steep canyon wall. This is expected since satellite SLA was spatially smoothed with a length scale of 200 km. However, it is encouraging that the satellite-derived currents could resolve the eddy structure. The second spatial pattern of observed currents suggests two counter-rotating eddies splitting roughly at the center of the canyon, one at the head of the canyon and the other at the foot. The mode 2 velocity pattern of observed currents again seems to be guided by the topography. The second spatial pattern of satellite-derived currents also reveals an eddy pair, and again its velocity structure seems to show more cross-slope motion.

The first mode explains 87% of the covariance between observed and satellite-derived currents, and accounts for 48% and 40% respectively of the observed and satellite-derived variances. The second mode explains 10% of the covariance, and accounts for 16% and 18% respectively of the observed and satellite-derived velocity variances. The first mode is the dominant fluctuation. The second mode, whose temporal and spatial structures are quite different from the second mode derived between observed and model currents, also seems to be quite meaningful. This is supported by the fact that the first two EOF modes of observed currents are almost identical to the first two modes of observed currents of the SVD analysis.

The results of this SVD analysis to the two-year observed and satellite-derived near-surface currents in DSC revealed two dominant modes of low frequency ("eddy") fluctuations. Mode 1 consists of a single eddy trapped near the foot of the canyon, and mode 2 displays an eddy-pair with counter-rotating eddies at both ends of the canyon. Satellite SLA is consistent with the surface geopotential calculated from the observed currents, in the sense that it contains both modes. It is expected that satellite SLA is able to reproduce the first mode because satellite data is of good quality over the deep part of the Gulf. The presence of the second mode in satellite SLA is surprising, because despite the poor local correlations between satellite-derived and observed currents, satellite SLA retained the coherent spatial patterns. This suggests the possibility of assimilating altimetry measurements, which will have major impacts on coastal ocean prediction experiments in the shelf and slope region.

The dominant mode 1 fluctuations are associated with both cyclonic and anticyclonic eddies. The cold cyclonic eddy (LC frontal eddy) has been well documented. In contrast, the anticyclonic eddy remains rather obscure. Wiseman and Dinnel (1988) found frequent presence of warm water and associated strong eastward currents on the Mississippi-Alabama shelf, however, these events were not usually associated with the deep northward extension of LC or LCE. It is suggested that those warm intrusions were associated with the mode 1 anticyclonic eddy, which according to analysis of the larger scale distribution of SLA (see Wang et al. 2003), is often present in this region when the LC is at its normal southern position. The model runs include assimilation of both SLA and SST, with the model means and current ellipses agreeing

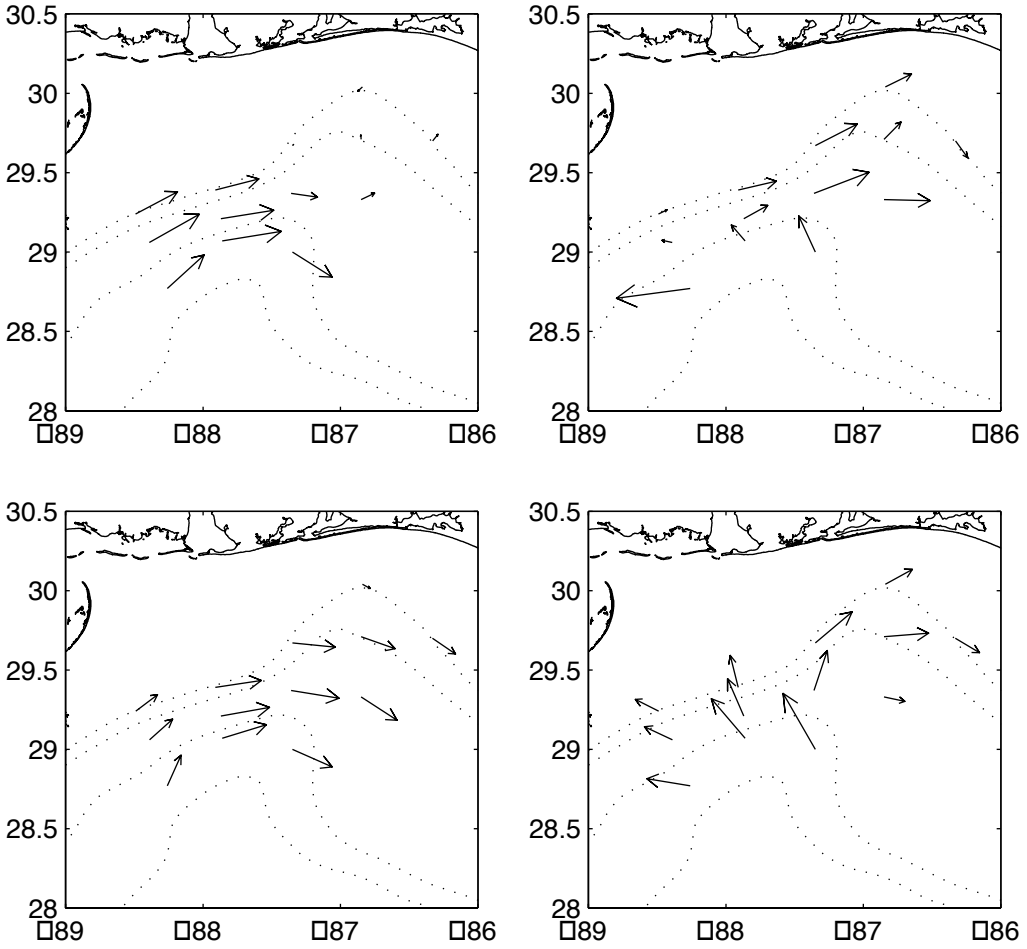

Figure 5.1-3. First (left) and second (right) spatial patterns of observed (upper) and satellite-derived (lower) currents. The velocity scale is arbitrary. Dotted lines are isobaths at 2000, 1000, 200 and 100 m.

fairly well with the observations. The model currents contain realistic single-eddy structure that accounts for about half of the total velocity variance. Moreover, the model currents, unlike the corresponding satellite-derived currents, are constrained by the steep slope topography. This is encouraging since a principal benefit of employing data assimilation is to supplement partial observations with model dynamics. The model currents, however, do not agree as well as the satellite-derived currents. This suggests that the data assimilation scheme has not taken full advantage of the satellite information (i.e. is not optimal). One solution may be to relax the (arbitrary) constraint that was imposed on assimilating the satellite SSH only in regions where the water depths > 500 m. A more serious shortcoming is that the degree of data nudging (see equation 2.1-1) was determined by pre-computed correlations between model sea-level anomaly and subsurface temperatures. Unfortunately, the correlations are low over the northern Gulf slope and rise, and the data assimilation has little direct impact in the DSC. To improve the pre-computed correlations, the model will need to generate more realistic LC frontal eddies in the eastern Gulf. Alternatively, it may be advantageous to use correlations between SSH and subsurface temperatures derived from observations such as the DSC study and other large-scale deep basin studies (see Chapter 6). Such experimentally derived correlations, supplemented by some empiricism, may be more widely applicable than for the immediate region (and time period) of the observational study.

5.2 Assimilation of Drifter Data

Accurate predictions or hindcasts of surface currents is an important goal for models of the Gulf of Mexico. Improvements in simulated surface currents will allow more accurate prediction of the positions and flows of eddies and other flow phenomena that will improve the prediction of surface dispersion of pollutants and assist in search and rescue operations. One source of surface current measurements is drifter trajectories, which can be tracked in near real-time using satellites. This source of data would be expected to complement schemes for the assimilation of SLA, SST, and hydrography that were discussed above. The interest is in the extent to which observed trajectories and circulation may be more accurately modeled when satellite and drifter information are used. In the study reported by Fan et al. (2003), a simple nudging scheme was used to assimilate observed drifters into a circulation model of the Northeastern Gulf of Mexico. The scheme was used in conjunction with the OI methods that assimilate satellite SSH and SST data, which were discussed above. The results were then compared with a model experiment that had no assimilation and other experiments with various permutations of SSH, SST and drifter assimilations. The study also demonstrated that data assimilation could effect the correct placement of Loop Current at the shelf edge, which in turn (remotely) forces the shelf currents.

Eight surface drifter trajectories were obtained for the period May to June 1998. They were all deployed in the Northeast Gulf as part of the MMS Northeastern Gulf of Mexico Shelf Physical Oceanography Program (NEGOM, DiMarco et al., 2001). Drifter trajectories were smoothed using a Gaussian-filter scale of 24 hours to eliminate tidal and inertial currents, and were sub-sampled at 3-hour intervals (Hamilton et al., 1999). Velocity components were then estimated from centered finite differences. The assimilation scheme used nudging of the momentum equations to the velocities of the drifters with an equation similar to (2.1-8). In one experiment the drifter velocity nearest the grid point was used to nudge, and in another all the drifters were used to make a weighted estimate of the nudging factor for each grid point. The 60-day drifter

trajectories were divided into 10-day segments to increase sample size and estimate the forecast errors over 10-day periods.

The model experiments were with no assimilation (A), with satellite SSH and SST assimilations (B), and other various permutations of SSH, SST and drifter assimilations (C, D and E). Experiment E has the satellite SSH, SST and weighted drifter assimilation, which gave the best results. Numerical trajectories that start and end at the times coincident with the beginnings and endings of the 10-day drifter trajectories were calculated using model surface velocities. The model prediction errors were then calculated as differences between the observed and modeled trajectories. Comparison of prediction errors shows that assimilation with satellite SSH, SST and drifters yielded the least error. Drifter position errors range from 30 ~ 80 km with a mean of about 60 km in 10 days, comparable to the errors obtained by Castellari et al. (2001). In particular, drifter assimilation can yield small-scale (diameter ~ 100 km) eddies that are generally not resolved by satellite data. An example is given in Figure 5.2-1 for two drifters in the DeSoto Canyon. Solid lines indicate the observed trajectories, and thin, medium and heavy dotted lines are modeled trajectories for experiments A, B and E, respectively. The observed trajectories indicate a small cyclone in the canyon, and the drifter assimilation (e.g. experiment E) could simulate this small current feature while it was missed in the experiments without drifter assimilation. This study also investigated the effect of data assimilation over the deep ocean region and showed that improving the remote forcing leads to a better simulation of observed shelf currents (Fan et al., 2003).

5.3 Causes of Loop Current Variability

One aspect of the Gulf's circulation which has thus far remained a mystery is why the Loop Current sheds eddies at such irregular, wide-ranging intervals, 3~17 months according to Sturges and Leben (2000). By systematically examining the model's response to forcing of varying complexities using the ECMWF wind and satellite data (Table 5.3-1), it was shown that wind-induced transport fluctuations through the Greater Antilles passages (see Figure 2.1-3) cause shedding at shorter intervals (≈ 3~7 months). On the other hand, Caribbean eddies (anticyclones) cause shedding at longer periods (≈ 14~16 months). This result is summarized in Figure 5.3-1. Other significant results from this study are: (1) LCE's sometimes detach and reattach from the LC (Figure 5.3-2), as have also been observed, and (2) there is evidence from satellite and model results that southwest of Hispaniola in the Caribbean Sea, anticyclones are fairly regularly spun up with periods of about 100 days (Figure 5.3-3). In Figure 5.3-2, the first three panels show a LC on the verge of shedding. The LCE is shed or detaches on 1999/8/18. A Caribbean eddy (CARE) can be seen to arrive at the channel from 1999/8/18-28, carrying with it the white-colored trajectories that indicate strong anticyclonic vorticity ($\varsigma/f < -0.4$), causing the LC to make a tight right-hand turn into the Straits of Florida. As the CARE completes its passage through the channel, part of its mass 'leaks' along the Cuban northern coast (1999/9/2-7), however, the remaining (main) portion interacts with the shed eddy (1999/9/7-12), and the two eddies eventually merge (1999/9/12-27). These results are described in more detail in Oey et al. (2003a).

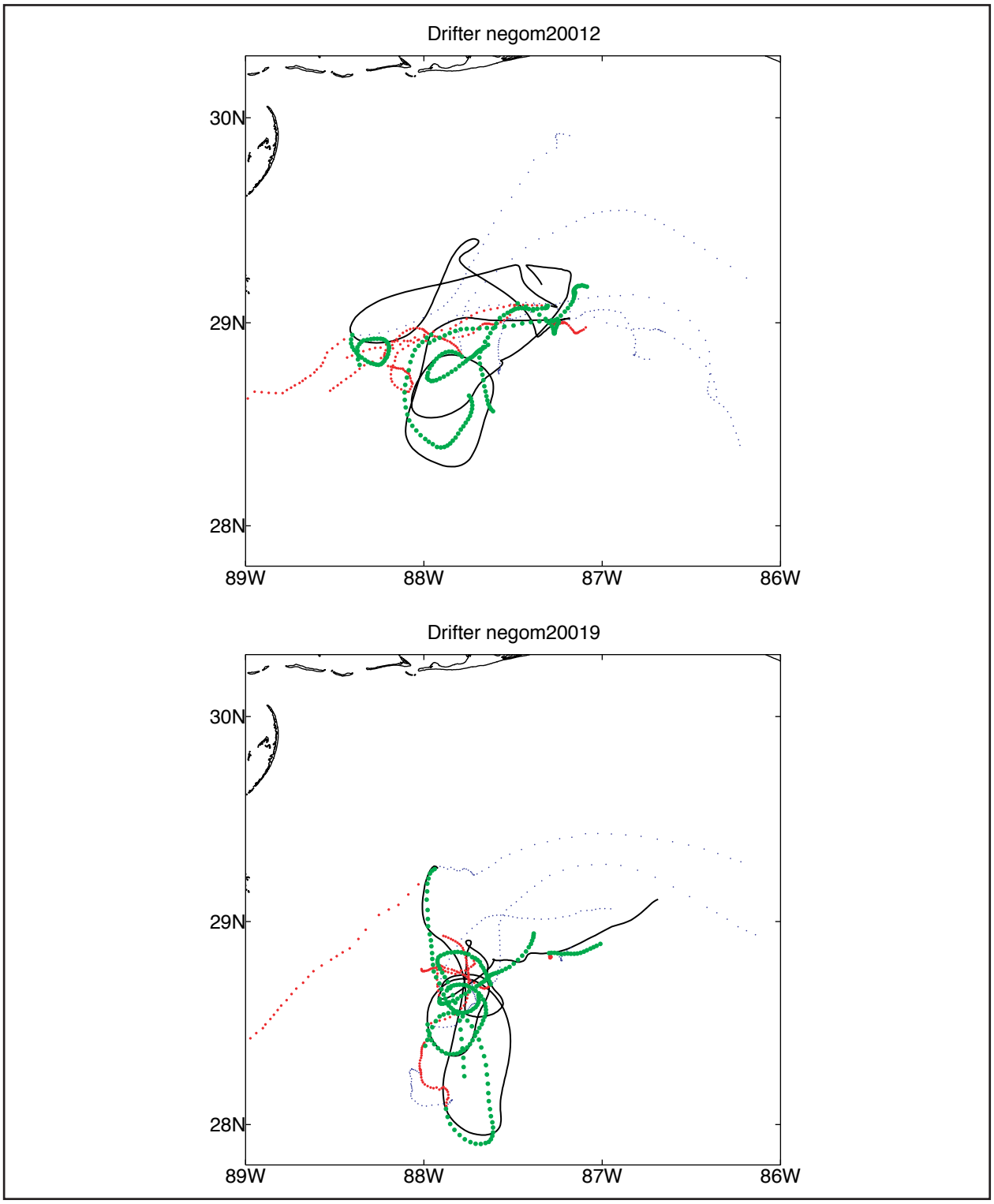

Figure 5.2-1. Observed and simulated trajectories for drifter #0012 (upper panel) and #0019 (lower panel) in the DeSoto Canyon group. Solid lines indicate the observed trajectories. Thin (blue), medium (red) and heavy (green) dotted lines are 10-day re-sample modeled trajectories of experiments A (no assimilation), B (SST & SSH assimilation) and E (SST, SSH & drifters), respectively.

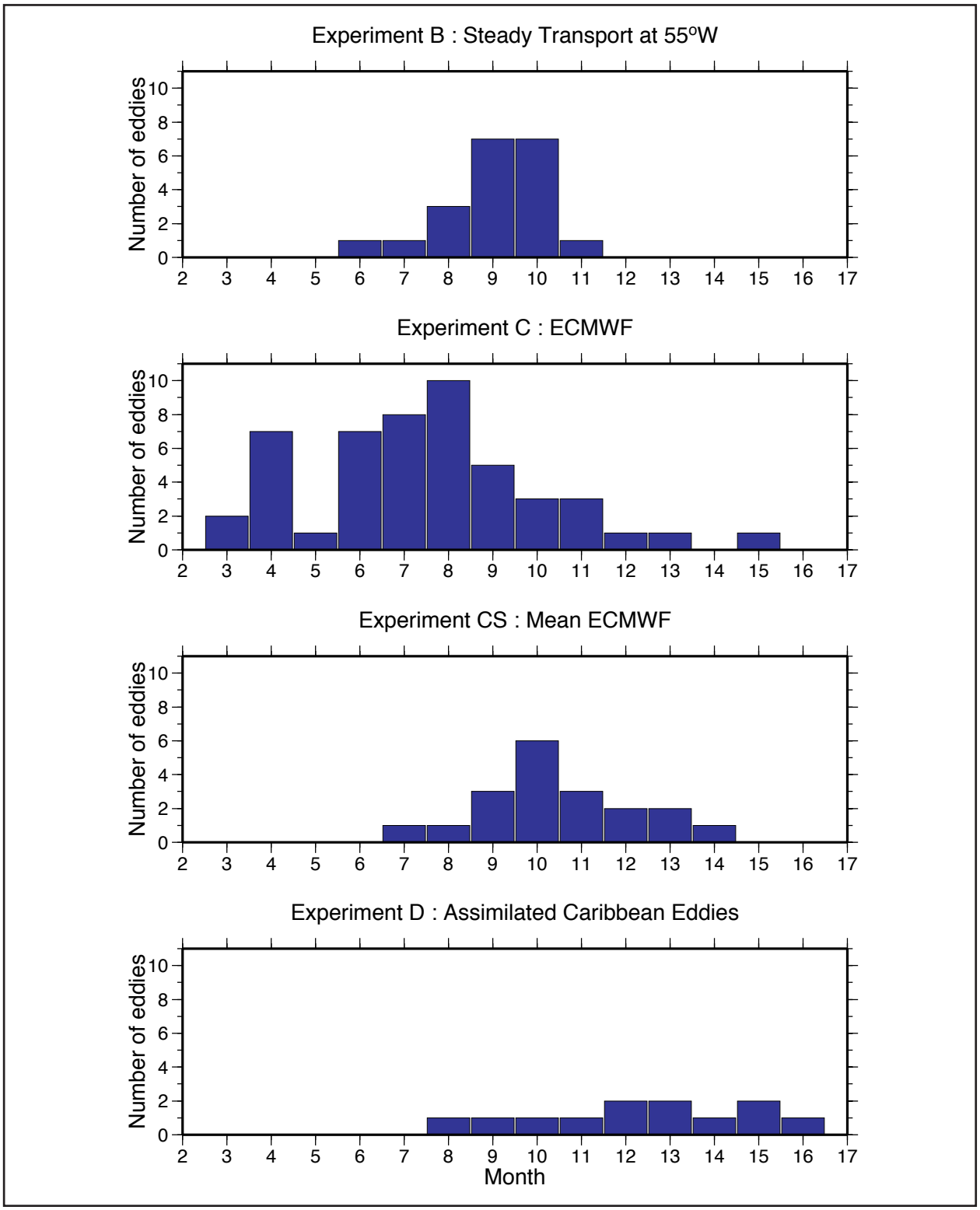

Figure 5.3-1. Histograms of Loop Current eddy shedding periods for Experiments B, C, CS and D (see Table 5.3-1). The abscissa is time in months between shedding and the ordinate is the number of shed eddies. The result for Experiment C is from a 32-year time series, while others are from 16-year time series.

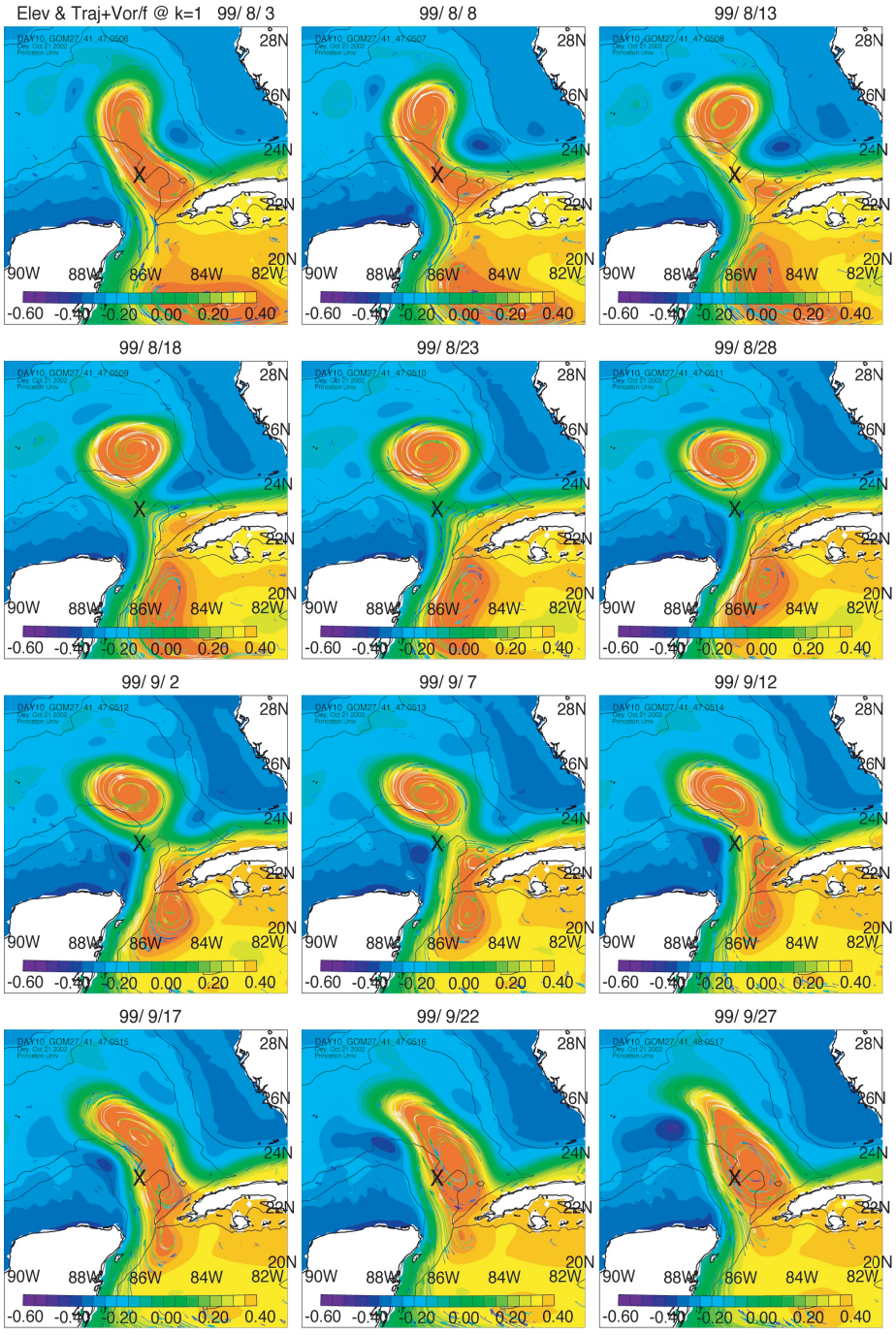

Figure 5.3-2. Loop Current eddy detachment and reattachment, experiment CS: Eulerian trajectories launched for 5 days centered around the indicated date in each panel, and from every 10th grid point at the first sigma level (i.e. surface), superimposed on color image of surface elevation (red for values ≥ 0.4 m, blue < -0.6 m). Colors on trajectories indicate ζ/f such that black/dark-blue through yellow indicate ζ/f from 0 through -0.4, and white for ζ/f < -0.4. Cyclonic trajectories are omitted for clarity. Dark contours are the 200-m and 2000-m isobaths. Time interval between panels is 5 days.

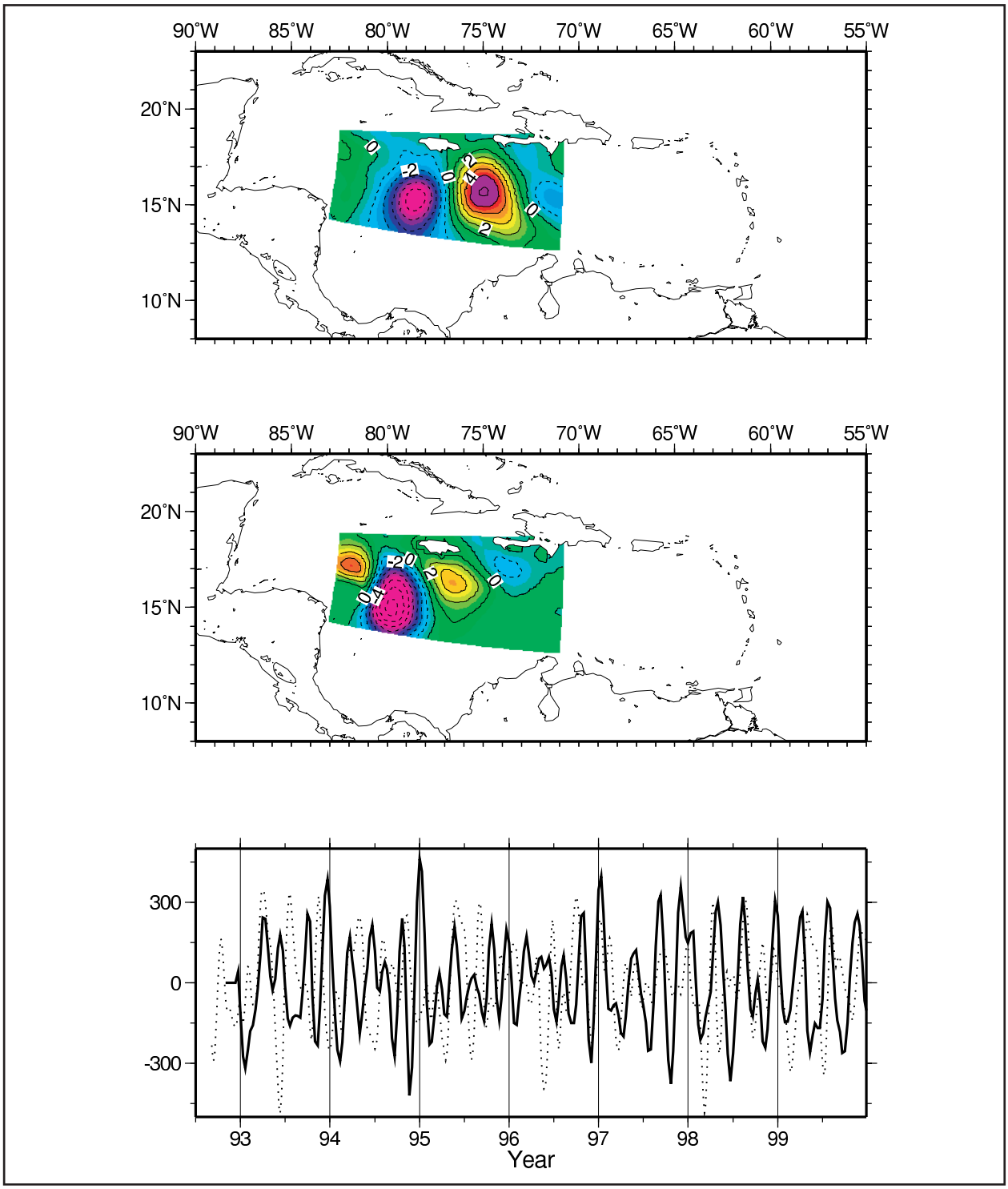

Figure 5.3-3. The second EOF mode (20%) from satellite SSH anomaly (1992-1999; top panel), and first EOF mode (26%) from experiment CS (middle panel), and the corresponding time series (lower panel; solid: satellite, dotted: model). The region is southwest of Hispaniola, as shown. The model time series has been phase-shifted by □ in order to show the similarity in periods of fluctuations between the model and satellite. Both show periods □ 100 days.

Table 5.3-1. Model Experiments

All experiments had steady transport specified at 55°W, taken from Schmitz (1996). Experiments A, B, CS and D were for 16 years, while experiment C was for 32 years. Experiments A and B were initialized from the 10-year run of Oey and Lee (2002), while the other experiments were initialized from the eighth year of Experiment B. Note that the experiments were designed so that only one forcing at one time was changed. The "–" means that the particular forcing was not imposed, i.e. is zero.

Forcing Experiments	Boundary T/S @ 55°W	Wind	Satellite Assimilation
A	Steady*	-	-
B	Monthly#	-	-
C	Monthly	6-hourly ECMWF	-
CS	Monthly	Mean ECMWF	-
D	Monthly	-	SSH Anomaly

* Annual Climatology
# Monthly Climatology

6. Summary and Recommendations

6.1 Summary

This study has investigated two main issues concerning modeling circulation processes in the Gulf of Mexico. They are the characterization of TRW's in the lower –layer, and the evolution of the upper-layer northern-slope eddy field. The former involves the genesis, propagation and refraction of TRW's and how well model TRW's compare with observed lower-layer currents. The latter involves assimilating limited area, but high resolution, hydrographic fields into a model and investigating the physical processes of the eddy interactions as the model evolves. A theme of this study has been the use of observations to improve the performance of models through assimilation and comparison with physical processes described by data.

One aim of this study was to attempt to understand the mechanism(s) by which bottom-trapped topographic Rossby waves (TRW's) over the continental slope and rise of the Gulf of Mexico are generated by Loop Current (LC) and Loop Current Eddy (LCE) variability. In Chapter 3 and Oey and Lee (2002), evidence for finding TRW's from a primitive-equation (PE), circulation model of the Gulf of Mexico, and in locating their possible energy sources was given. A ten-year model simulation forced only by constant transport from the Atlantic was conducted so that regular LCE sheddings occured. Deep-layer analyses were then performed to band-pass motions with 20 to 100-day periods, a range that corresponds to that found for the observed deep EKE at the few available current-meter locations in the Gulf. It was found that in certain well-defined regions, over the 3,000-m isobath across the central Gulf in particular, spectral peaks occur within these periods; the band-passed EKE is significant (i.e. exceeds a Gulf-wide standard deviation of 10^{-3} m^2s^{-2}), exhibits bottom intensification, and accounts for over 60% of the deep energy (Figure 3.1-4). These deep motions, moreover, occur in regions where TRW's can be supported, and the phase and correlation analysis suggests offshore and down-slope phase propagation consistent with the TRW dispersion relation (Figure 3.1-6). The wavenumber vectors computed from the PE model results are consistent with the dispersion relation (Figure 3.1-8), and yield wavelengths 63-210 km. These model-derived wavelengths are shorter than Hamilton's (1990) estimates of 110-300 km based on the observations, but more in-line with later estimates from more closely spaced arrays (Hamilton et al., 2003). A possible source of discrepancy is due to the uncertainty in the Brunt-Väisälä frequency. By utilizing the TRW dispersion relation to track energy pathways (ray-tracing), it is found that the rays coincide with the above region of significant EKE over the 3,000-m isobath (Figure 3.1-7a). East of 91°W, the source of EKE comes from the LC and LCE-shedding region, while over the western Gulf additional source is from the southwestward propagating LCE's. Since, in a topographically dominated region, ray directions depend primarily on the angles between wavenumber components, the computed ray-paths are relatively insensitive to wavelengths, so that the (PE) modeled region of significant EKE survives despite the possible discrepancy between modeled and observed wavelengths. The vertical trapping scales (of the 20 to 100-day bottom motions) are estimated to decrease (from ≈ 600 m to 300 m) with distance to the west. While exact values differ, the trend agrees with the ray solution (Figure 3.1-7b). These rays indicate that refractions by topographic gradients and by deep currents with cyclonic shearing play an important role in confining the possible energy paths just inshore of the 3,000-m isobath in the central Gulf. In regions where rays are focused, the *simulated* EKE's increase (Figure 3.1-7a at 91°W, 94°W and

95°W). Refraction causes wave shortening, which suggests dissipation as TRWs propagate westward (Hamilton, 1990). The presence of deep (westward) currents increases the TRW group speeds, by 2-3 km day^{-1}. This and the constraints on allowable ray-path imposed by current shear may be used to infer deep currents in the Gulf. The ray calculations also suggest that energy sources for the TRW's, found in the PE model, are from short-scale propagating meanders (~ 100 to 200 km wavelengths and <100 day periods) around the LC and LCE's.

Direct comparison of modeled deep currents with observations shows that energy levels were generally underestimated though they improved when assimilation and higher resolution grids were used. Comparison of KE spectra shows that the model generates a similar spectral character to the observations with 20 to 100-day KE being prominent. Bottom intensification, characteristic of TRW's, is also found in the model where bottom currents are energetic. A slightly suprising finding is that model currents in the lower water column are less coherent through the vertical than were the observations.

In Chapter 4, the report on a first attempt to assimilate directly hydrographic data into a model that was already using assimilation of Gulf-wide SSH and SST at coarser resolution was given. The hydrographic data only covered a limited area of the northern slope region and thus, had to be injected into evolving model fields. This was successfully accomplished for a survey of the northern Gulf slope during December 5 to 12, 1993. The evolution of the slope eddy field was followed for a few weeks and compared with a partial survey of the same region during December 16 to 23, 1993. Both the model and observations showed an increase in energy associated with increased meandering of the shear regions between cylones and anticyclones. An analysis of the model energetics showed that mixed barotropic-baroclinic instabilities were feeding the eddy flows. These instabilities were more effective on the northern side of a slope cyclone, where the topographic and isopycnal slopes were of opposite sign. On the southern side of the cyclone, the analysis showed that the flow is stabilizing and the eddy energy was being transferred to deeper water. Hydrographic analysis of PV and Q-vector divergence showed that the meandering of PV fronts was related to up- and down-welling on the periphery of the eddies, and thus, up and down displacements of the pycnocline. This is an indication of how the instabilities may develop over the course of a few days to a week time period.

6.2 Recommendations for Future Model Development

While progress has been made in the modeling and data analyses of various circulation processes in the Gulf, some issues have come out, both in the ability to model and also in new hypotheses that may be raised. This subsection describes improvements that can be made to the model and also future modeling studies that should be useful to the overall objective of obtaining more realistic hindcast currents in the Gulf. The next subsection discusses various plausible mechanisms and hypotheses that may be explored.

Although the model can reproduce quite well the near-surface and mid-level energy (as seen previously in DeSoto Canyon comparison study by Wang et al. (2003), and also in our simulation of the slope eddies over the central Gulf, in Chapter 4), it tends to underestimate the near-bottom energy. This was discussed previously in conjunction with data from the DeSoto Canyon extension study. It is believed that the deficiency in this case is related to the rather poor

vertical resolution that we have used, $\Delta z \approx 350$ m outside the bottom boundary layer (BBL). With a vertical decay scale of TRW's of about 1,000 ~ 1,500 m, the energy is bound to be underestimated. It may be thought that some of the BBL grid points may be relaxed (i.e. less grid points in BBL) and be better used to resolve the TRW's. The situation is not as straight forward, however, and it possible that the BBL plays a prominent role in subsurface dynamics over a slope (see below). A better course of action would be to transit fully to the newly-implemented MPI version of the PROFS code, which has 40 vertical levels and an averaged horizontal resolution of about 7 km in the Gulf of Mexico.

In Chapter 4, a procedure was described through which satellite-SSH assimilation can be combined with nudging of the density field from hydrographic surveys to obtain fairly realistic features of the slope eddies including the 'prediction' of their evolution. The algorithm in this case is simple and may be expanded. The hydrographic fields can be included as part of the overall MVOI (Multi-Variate Optimum Interpolation) scheme already used for the satellite SSH (and SST) assimilations (Section 2.1.2). The MVOI should ideally be tested using the MMS Exploratory Physical Oceanography Study presently being conducted over the central Gulf (Figure 6.2-1). This Exploratory Study will map eddies and deep currents over a substantial region of the north central Gulf using a combination of PIES (Inverted Echo Sounders with Pressure that effectively measure the density profile through the water column (Hamilton et al., 2003)), current meter moorings and deep RAFOS lagrangian floats. Thus, the study will examine rather thoroughly currents and density throughout the water column in a region where the study of Oey and Lee (2002) has indicated potentially large energy as a result of LC pulsations and LCE passages. Here, it would be possible to explore thoroughly the feasibility of using the various types of data at time intervals of the order of one day. For example, one can check the accuracy of the simulation results if only floats are included as part of the MVOI assimilation, if only the moorings data are used, or if only satellite data (SSH) are used, etc. The skill and benefits of assimilating more observations, velocity, drifters, hydrography, in addition to satellite information, can be assessed. It would also be useful to explore how models with and without assimilation 'predict' energetic deep currents, and how well they compare with observations. This type of assimilative parametric studies can yield useful information especially with regard to optimal use of observations in hindcasting the currents. It can also suggest the type of data that are most useful for accurate hindcasts. Therefore, the capability can now be built in which future MMS observational studies could first be 'simulated' so as to determine the optimal placement of data points. The potential benefits of such an intelligent system, both in terms of its scientific reward and cost saving, are obvious.

6.3 Recommendations for Future Process Studies

In addition to the improvements in assimilative modeling that are discussed above, it is important that model-data analyses are performed to investigate specific processes that must be accurately reproduced by the model if predictions are to be reliable. As more deep-basin observations become available from comprehensive experimental studies, such as the ongoing Exploratory study, noted above, and other large scale experiments that have been proposed by MMS and other agencies, model predictions can be tested. For example, if TRW's are produced as

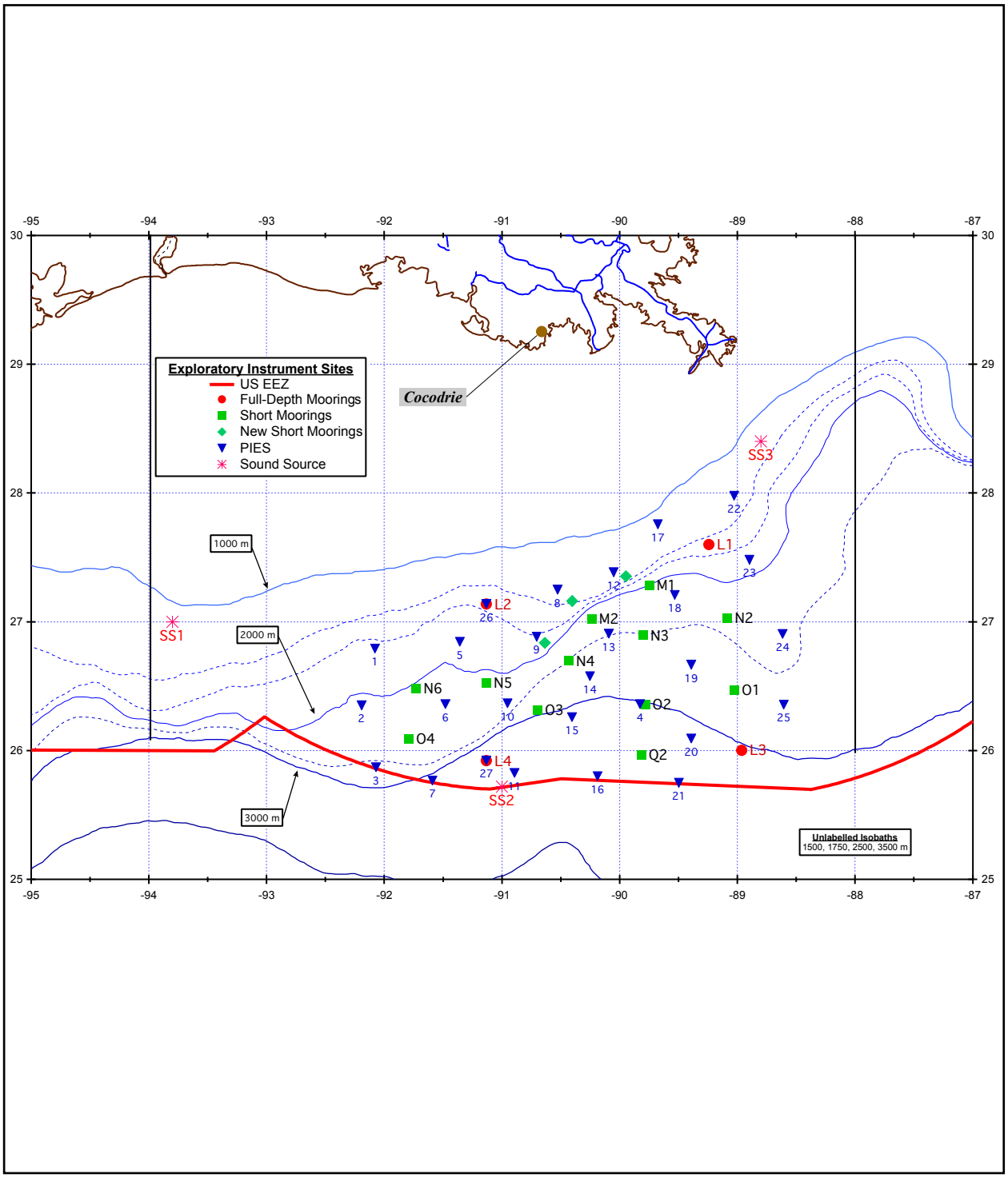

Figure 6.2-1. Positions of the moored instrument array in the MMS Exploratory Program (April 2003 to April 2004). Full-depth moorings are instrumented with current and temeperature sensors through the water column, short moorings have instruments 100 and 500 m from the bottom, and PIES are inverted echo sounders with pressure that can be used to generate 3-D temperature and salinity maps, and bottom pressure maps. The sound sources are used to locate deep RAFOS floats.

suggested by the model analyses, i.e. through excitation by peripheral frontal eddies (Oey and Lee, 2002), then can these processes be verified (or refuted) by detailed analyses of new data. Such a finding is clearly potentially significant, as it basically defines the way one must conduct future modeling studies, i.e. not only must the LCE's, be resolved, but also eddies at smaller scales O(50 km). Other processes that are suggested by the analyses in Chapters 3 and 4, and other model studies, are discussed below.

The observed erratic motions of the LCE's suggest that eddy-eddy interaction must play a role (Hamilton et al., 1999). Moreover, some of the eddies do not have much surface expression and therefore, can not be detected by satellite. It has been shown that these subsurface eddies are smaller than the LCE's but are potentially intense. Observationally well-known examples of such deeply intensified features are the cyclones that develop east of the LC, and that sometimes appear to 'cut across' the LC, leading to shedding. The physical mechanisms that produce these subsurface, smaller eddies are not well understood and there is little direct observational data. Genesis of peripheral eddies through dynamical instability may be one mechanism, but that alone may not be sufficient. The 'violent' interaction of LCE's with continental slope may be another, potentially important mechanism, as Oey and Zhang (2003, submitted, CSR) have found in a process study. In this study, the warm ring initially 'sits' over a slope with an adjoining shelf in a periodic channel, and its subsequent evolution is examined. The 'inviscid' response is cyclonic 'peeling-off' of the on-slope portion of the warm ring. The cyclone propagates away (to the left looking on-slope) from the warm ring, and is bottom-intensified as well as slope-trapped (cross-slope scale ≈ Rossby radius). The near-surface flow 'leaks' further onto the shelf while subsurface currents are blocked by the slope. The 'viscous' response consists of the formation of a bottom boundary layer (BBL) with a temporally and spatially dependent displacement thickness. The BBL 'lifts' the strong along-slope (leftward) current or jet ($> 0.5\ m\ s^{-1}$) away from the bottom. The jet, coupled with weak stratification within the BBL and convergence due to downwelling across the slope, becomes supercritical. Super-inertial disturbance in the form of a hydraulic jump or front, with strong upwelling and downwelling cell, and the jet, propagate along the slope as well as off-slope and upward into the water column. The upward propagation is halted at $z \approx z_{trap}$ when mixing smoothes out the 'jump' to an along-slope scale λ_{trap} that allows the ambient jet to bend the propagation path horizontal. At this 'matured' stage, $z_{trap} \approx -250\ m$, $\lambda_{trap} \approx 50\ km$, and the jet's cross-slope and vertical scales are $\approx 30\ km$ and $50\ m$ respectively. A sketch of the interactions of such flows with the slope is given in Figure 6.3-1. Oey and Zhang (2003) also gives an example that illustrates the process under a more realistic setting in the Gulf of Mexico when the Loop Current impinges upon the west Florida slope is given. The phenomenon may be relevant to recent oil industry's measurements in the Gulf, which at times indicate jets at $z \approx -150\ m$ through $-400\ m$ over the slope. Such intense development of cyclone and subsurface jet (together with the potentially important offshore and upward leakage of the otherwise slope-bound energy) should be more thoroughly studied in the future.

Finally, there is an considerable interest in understanding why the LC sheds eddies at such irregular intervals, and perhaps more importantly from a practical standpoint, if it can be predicted. The study by Oey et al. (2003a) provides a tentative answer. They point out the important roles played by velocity and vorticity distributions at the Yucatan Channel. An expanded study can be conducted with the recently acquired Yucatan Channel dataset (DeepStar). One can combine these data with a series of assimilative model experiments and

attempts to understand the response of the modeled LC. One fundamental question is the role of Caribbean eddies that squeeze through the channel in affecting the timing of shedding. Another relates to the intense cyclonic vorticity that develops at the western portion of the LC in the channel, for which models often show downstream amplification. Do these cyclonic perturbations account for the development of peripheral eddies around the LC, and do the cyclonic eddies amplify when the LC impacts upon the west Florida continental slope. These issues are both of scientific and practical interests.

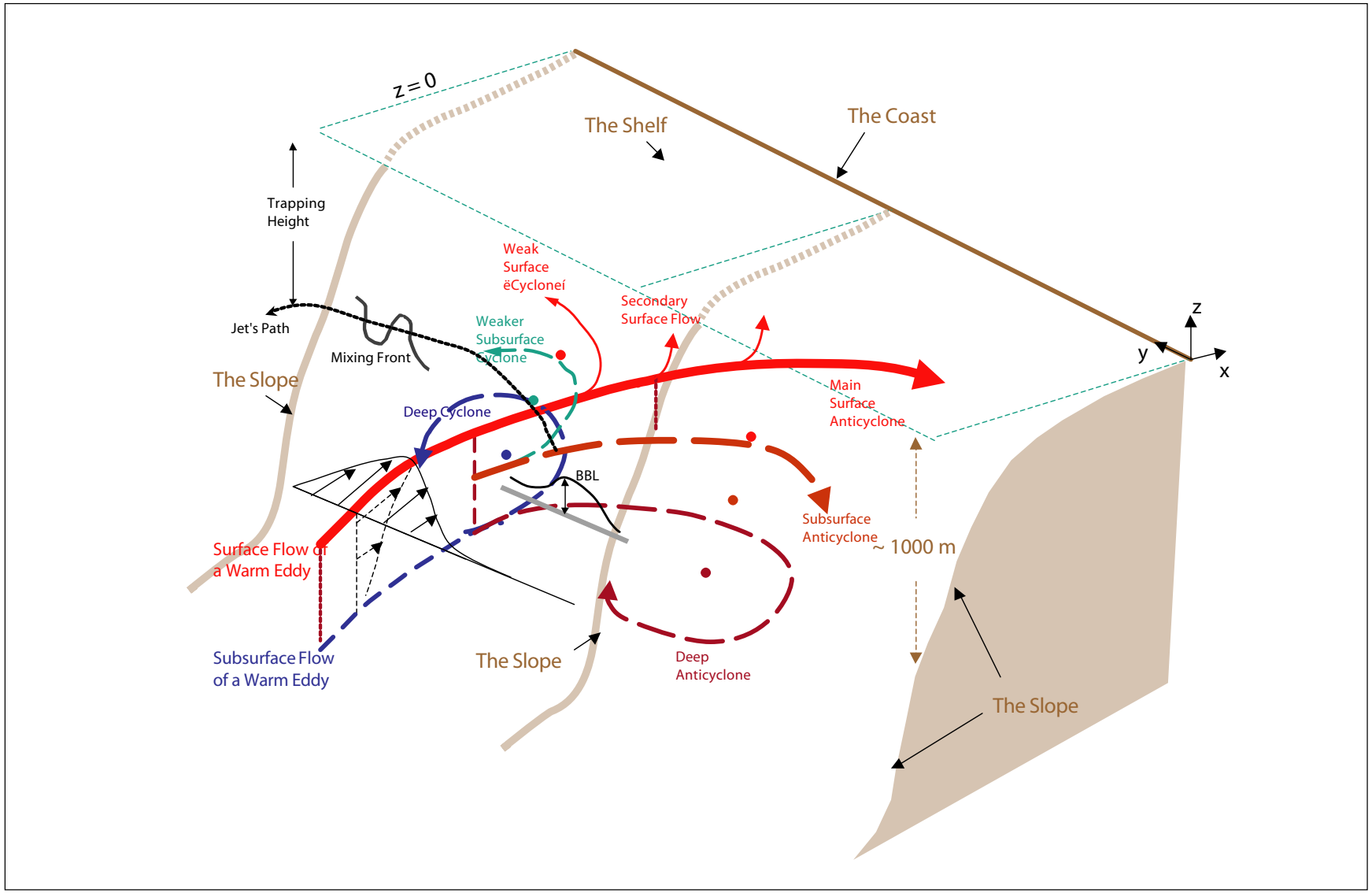

Figure 6.3-1. A schematic depiction of the 'violent' interaction of a warm eddy with a continental slope (from Oey et al., unpublished). See text for descriptions.

7. References

Allen, J.T., and D.A. Smeed, 1996. Potential vorticity and vertical velocity at the Iceland-Faroes front. *J. Phys. Oceanogr.,* 26: 2611-2634.

Barnes, S. 1964. A technique for maximizing details in numerical map analysis, *J. Appl. Meteor.* 3: 395-409.

Berger, T.J., P. Hamilton, J.J. Singer, R.R. Leben, G.H. Born, and C.A. Fox, 1996. Louisiana/Texas Shelf Physical Oceanography Program: Eddy Circulation Study, Final Synthesis Report. Volume 1: Technical Report. . U.S. Department of the Interior, Minerals Management Service, Gulf of Mexico OCS Region, New Orleans, LA. OCS Study MMS 96-0051. 324 pp.

Bretherton, C.S., C. Smith, and J.M. Wallace, 1992.: An intercomparison of methods for finding coupled patterns in climate data. *J. Climate, 5*, 541-560.

Brooks, I.H., and P.P. Niiler, 1977. Energetics of the Florida Current. *J. Mar. Res.,*35:163-191.

Castellari, S., Griffa, A., Ozgokmen, T.M., Poulain, P.M., 2001. Prediction of particle trajectories in the Adriatic Sea using Lagrangian data assimilation, *J. Mar. Syst.* 29, 33- 50.

Csanady, G.T. 1979. The pressure field along the western margin of the North Atlantic. *J. Geophys. Res.,* 84:4905-4913.

Daley, R., 1991: *Atmospheric Data Analysis.* Cambridge University Press, New York, 457 pp.

DiMarco, S.F., Howard, M.K., Jochens, A.E., 2001. Deepwater Gulf of Mexico historical Physical Oceanography and data inventory. Department of Oceanography, Texas A&M University, Technical Report 01-01-D. 196 pp.

Dong, C. and L.-Y. Oey, 2003: Data assimilation experiments in a coastal zone with significant wind and wind curl. *(Submitted to J. Atmos. Oceanic Tec.)*

Ducet, N., P.Y. Le Tron, and G. Reverdin, 2000: Global high-resolution mapping of ocean circulation from TOPEX/Poseidon and ERS-1 and –2. *J. Geophys. Res.*, 105, 19,477-19,498.

Ertel, H. 1942. Ein Neuer hydrodynamischer Wirbelsatz. *Meteor. Z.,* 59: 271-281.

Ezer, T., L-Y Oey, W. Sturges and H.-C. Lee, 2003. The variability of currents in the Yucatan Channel: analysis of results from a numerical ocean model, *J. Geophys. Res.*, 108: 12-1, 12-13 (doi: 10.129/JC001509).

Fan, S.J., L.-Y. Oey, and P. Hamilton, 2003: Assimilation of drifters and satellite data in a circulation model of the northeastern Gulf of Mexico. Submitted to *Cont. Shelf Res.* (Available through http://www.aos.princeton.edu/WWWPUBLIC/PROFS/ under "Publications.")

Forristall, G.Z., K.J. Schaudt, and C.K. Cooper, 1992: Evolution and kinematics of a Loop Current eddy in the Gulf of Mexico during 1985. *J. Geophys. Res*., 97: 2173-2184.

Fratantoni, D.M., 2001. North Atlantic surface circulation during the 1990's observed with satellite-tracked drifters. *J. Phys. Oceanogr.* 106: 22,067-22,093.

Hamilton, P. 1990. Deep currents in the Gulf of Mexico. *J. Phys. Oceanogr*., 20: 1087-1104.

Hamilton, P. 1992. Lower Continental Slope Cyclonic Eddies in the Central Gulf of Mexico. *J. Geophys. Res.*, 97: 2185-2200.

Hamilton, P., G.S. Fargion and D.C. Biggs. 1999. Loop Current eddy paths in the western Gulf of Mexico. *J. Phys. Oceanogr.*, 29, 1180-1207.

Hamilton, P., T.J. Berger, J.J. Singer, E. Waddell, J.H. Churchill, R.R. Leben, T.N. Lee, and W. Sturges, 2000. Desoto Canyon Eddy Intrusion Study, Final Report, Volume II: Technical Report. OCS Study MMS 2000-080. U. S. Dept. of the Interior, Minerals Management Service, Gulf of Mexico OCS Region, New Orleans, LA. 275 pp.

Hamilton, P., and A. Lugo-Fernandez, 2001. Observations of high speed deep currents in the northern Gulf of Mexico. *Geophys. Res. Lett.,* 28, 2867-2870.

Hamilton, P., T.J. Berger, and W. Johnson, 2002: On the structure and motions of cyclones in the northern Gulf of Mexico. *J. Geophys. Res.,* 107,3208 Department of Interior: 10.1029, 1-18.

Hamilton, P., J.J Singer, E. Waddell, and K. Donohue, 2003: Deepwater observations in the northern Gulf of Mexico from in-situ current meters and PIES. Volume II: Technical Report. U.S. Dept. of Interior, Minerals Management Service, Gulf of Mexio OCS Region, New Orleans, LA. OCS Study MMS-2003-049. 97 pp.

Haney, R.L., 1991: On the pressure gradient force over steep topography in sigma coordinate ocean models. *J. Phys. Oceanogr.,* 21, 610-619.

Hurlburt, H.E., and J.D. Thompson, 1980: A numerical study of Loop Current intrusions and eddy shedding. *J. Phys. Oceanogr.,* 10, 1611-1651.

Hogg, N.G., 1981: Topographic waves along 70^{o}W on the continental rise. *J.Mar.Res.*, 39, 627-649.

Jochens, Ann E., Steven F. DiMarco, Worth D. Nowlin, Jr., Robert O. Reid, and Mahlon C. Kennicutt II, 2002. Northeastern Gulf of Mexico Chemical Oceanography and Hydrography Study: Synthesis Report. OCS Study MMS 2002-055. U.S. Department of the Interior, Minerals Management Service, Gulf of Mexico OCS Region, New Orleans, LA. 538 pp.

Kirwan, A.D., Jr., J.K.Lewis, A.W. Indest, P. Reinersman, and I. Quintero, 1988. Observed and Simulated Kinematic Properties of Loop Current Rings. *J. Geophys. Res.*, 93: 1189-1198.

Lau, K.M. and H.Y. Weng, 2001: Coherent modes of global SST and summer rainfall over China: An assessment of the regional impacts of the 1997-98 El Nino. *J. Climate, 14*, 1294-1308.

Leben, R.R. G.H. Born, and B.R. Engebreth, 2002: Operational altimeter data processing for mesoscale monitoring. *Marine Geodesy,* 25, 3-18.

LeBlond, P.H., and L.A. Mysak, 1978. *Waves in the Ocean,* Elsevier, Amsterdam, 602pp.

Lighthill, M.J. 1978: *Waves in Fluids*. Cambridge University Press, London and New York.

Louis, J.P., B.D. Petrie, and P.C. Smith, 1982: Observations of topographic Rossby waves on the continental margin off Nova Scotia. *J. Phys. Oceanogr.,* 12: 47-55.

Mellor, G.L. and T. Ezer, 1990: A Gulf Stream model and an altimetry assimilation scheme. *J. Geophys. Res. 96:* 8779-8795.

Mellor, G.L., L.-Y. Oey, and T. Ezer, 1998. Sigma coordinate pressure gradient errors and the seamount problem. *J. Atmos. Oceanic Tec.,* 15: 1122-1131.

Meinen, C., E. Fields, R.S. Pickart, and D.R. Watts, 1993. Ray tracing on topographic Rossby waves. Graduate School of Oceanography, Technical Report 93-1, University of Rhode Island, 43 pp.

Oey, L.-Y. and P. Chen. 1992: A model simulation of circulation in the northeast Atlantic shelves and seas. *J. Geophys. Res.,* 97: 20,087-20,115.

Oey, L-Y., 1996. Simulation of mesoscale variability in the Gulf of Mexico, *J. Phys. Oceanogr.*, 26: 145-175.

Oey, L-Y. 1998. Eddy energetics in the Faroe-Shetland Channel, *Cont. Shelf Res*., 17: 1929-1944.

Oey, L.-Y., D.-P. Wang, T. Hayward, C. Winant and M. Hendershott, 2001: Upwelling and cyclonic regimes of the near-surface circulation in the Santa Barbara Channel. *JGR-Oceans*, 106: 9,213-9,222.

Oey, L-Y. and H.C. Lee, 2002: Deep eddy energy and topographic Rossby waves in the Gulf of Mexico. *J.Phys.Oceanogr.*, 32: 3499-3527.

Oey, L.-Y., H.-C. Lee, T. Ezer and Wei, 2002: An Embedded Circulation Model of the Gulf of Mexico, Part I: Descriptions and Experiments Using ECMWF Winds and Satellite Data. *(In preparation.)*

Oey, L.-Y., H.-C. Lee, and W.J. Schmitz, Jr., 2003a: Effects of winds and Caribbean eddies on the frequency of Loop Current eddy shedding. *J. Geophys. Res.*, *in press*. (Available through *http://www.aos.princeton.edu/WWWPUBLIC/PROFS/* under "Publications.")

Oey, L.-Y., C. Winant, E. Dever, W. Johnson, and D.-P. Wang, 2003b: A data-assimilated model of the near-surface circulation of the Santa Barbara Channel. *J. Phys. Oceanogr.,* in press. (Available through http://www.aos.princeton.edu/WWWPUBLIC/PROFS/ under "Publications.")

Oey, L.-Y., and H.C. Zhang, 2003: A mechanism for the generation of subsurface cyclones and jets. (S*ubmitted, Cont. Shelf Res.)*

Orlanski, I., and M.D. Cox, 1972. Baroclinic instability in ocean currents. *Geophys. Fluid Dynamics.* 4:297-332.

Paluszkiewicz, T., L.P. Atkinson, E.S. Posmentier and C.R. McClain, 1983: Observation of a Loop Current frontal eddy intrusion onto the west Florida shelf. *J. Geophys. Res.,* 9639-9651.

Pedder, M.A., 1989: Limited area kinematic analysis by a multivariate statistical interpolation method, *Mon. Wea. Rev.,* 117: 1695-1708.

Pedder, M.A., 1993. Interpolation and filtering of spatial observations using successive corrections and Gaussian filters. *Mon. Weath. Rev.* 121: 2889-2902.

Pedlosky, J., 1977: On the radiation of meso-scale energy in the mid-ocean. *Deep Sea Res.,* 24: 591-600.

Pickart, R.S., 1995. Gulf Stream-generated topographic Rossby waves. *J. Phys. Oceanogr.* 25: 74-584.

Pollard, R.T., and L. Regier, 1992. Vorticity and vertical circulation at an ocean front. *J. Phys. Oceanogr.,* 22: 609-625.

Press, W.H., S.A. Teukolsky, W.T. Vetterling and B.P. Flannery, 1992: *Numerical Recipes*. 2nd Edition, Cambridge University Press, New York, 963 pp.

Rhines, P.B., 1970. Edge-, bottom-, and Rossby waves in a rotating stratified fluid. *Geophys.Fluid Dyn.*, 1: 273-302.

Robertson, A.W., C.R. Mechoso and Y.J. Kim, 2000: The influence of Atlantic sea surface temperature anomalies on the north Atlantic oscillation. *J. Climate,* 13: 122-138.

Sanford, T.B., P.G. Black, J.R. Haustein, J.W. Feeney, G.Z. Forristall, and J.F. Price. 1987. Ocean response to a hurricane, I Observations. *J. Phys. Oceanogr.* 17: 2065-2083.

Schmitz, W.J., Jr., 1996: On the World Ocean Circulation: Volume I – Some Global Features/North Atlantic Circulation. WHOI Technical Report WHOI-96-03: 141 pp.

Science Applications International Corporation, 1987. Gulf of Mexico Physical Oceanography Program, Final Report, Year 4, Volume II: Technical Report. A final report by Science Applications International Corporation submitted to the Minerals Management Service, New Orleans, LA. Contract No. 14-12-0001-29158.

Science Applications International Corporation, 1988. Gulf of Mexico Physical Oceanography Program, Final Report: Year 3, Volume II: Technical Report, OCS Report/MMS 88-0046, U.S. Department of the Interior, Minerals Management Service, Gulf of Mexico OCS Regional Office, New Orleans, LA. 241 pp.

Science Applications International Corporation, 1989. Gulf of Mexico Physical Oceanography Program, Final Report: Year 5, Volume II: Technical Report. OCS Report/MMS - 89-0068, U.S. Department of the Interior, Minerals Management Service, Gulf of Mexico OCS Regional Office, New Orleans, LA. 333 pp.

Singer, J.J. 1990. On the error observed in electronically digitized T-7 XBT data. *J. Atmos. Oceanic Technol.,* 7(4): 603-611.

Smagorinsky, J., 1963: General circulation experiments with the primitive equations. Part I: the basic experiment. *Mon. Wea. Rev.,* 91: 99-164.

Sturges, W., J.C. Evans, S. Welsh, and W. Holland, 1993: Separation of warm core rings in the Gulf of Mexico. *J. Phys. Oceanogr.,* 23: 250-268.

Sturges, W., and R. Leben 2000. Frequency of ring separations from the Loop Current in the Gulf of Mexico: A revised estimate. *J. Phys. Oceanogr.,* 30: 1814-1819.

Teague, W. J., Carron, M.J., Hogan, P.J., 1990. A comparison between the Generalized Digital Environmental Model and Levitus climatologies, *J. Geophy. Res.,* 95: 7167-7183.

Thompson, R.O.R.Y., 1977: Observations of Rossby waves near site, *D. Prog. Oceanogr.,* 7: 135-162

Vukovich, F.M., B.W. Crissman, M. Bushnell and W.J. King, 1979: Some aspects of the oceanography of the Gulf of Mexico using satellite and in-situ data. *J. Geophys. Res.* 84: 7749-7768.

Wallace, J.M., C. Smith and C.S. Bretherton, 1992: Singular value decomposition of wintertime sea surface temperature and 500-mb height anomalies. *J. Climate,* 5: 561-576.

Wang, J. and M. Ikeda, 1997. Diagnosing ocean unstable baroclinic waves and meanders using the Quasigeostrophic Equations and Q-Vector Method. *J. Phys. Oceanogr.,* 27: 1158-1172.

Wang, D.-P., L.-Y. Oey, T. Ezer and P. Hamilton, 2003: Nearsurface currents in DeSoto Canyon. *J. Phys. Oceanogr.*, 33: 313-326.

Wiseman W.J, Jr., and S.P. Dinnel, 1988. Shelf currents near the mouth of the Mississippi River. *J. Phys. Oceanogr.,* 18: 1287-1291.

The Department of the Interior Mission

As the Nation's principal conservation agency, the Department of the Interior has responsibility for most of our nationally owned public lands and natural resources. This includes fostering sound use of our land and water resources; protecting our fish, wildlife, and biological diversity; preserving the environmental and cultural values of our national parks and historical places; and providing for the enjoyment of life through outdoor recreation. The Department assesses our energy and mineral resources and works to ensure that their development is in the best interests of all our people by encouraging stewardship and citizen participation in their care. The Department also has a major responsibility for American Indian reservation communities and for people who live in island territories under U.S. administration.

The Minerals Management Service Mission

As a bureau of the Department of the Interior, the Minerals Management Service's (MMS) primary responsibilities are to manage the mineral resources located on the Nation's Outer Continental Shelf (OCS), collect revenue from the Federal OCS and onshore Federal and Indian lands, and distribute those revenues.

Moreover, in working to meet its responsibilities, the **Offshore Minerals Management Program** administers the OCS competitive leasing program and oversees the safe and environmentally sound exploration and production of our Nation's offshore natural gas, oil and other mineral resources. The MMS **Minerals Revenue Management** meets its responsibilities by ensuring the efficient, timely and accurate collection and disbursement of revenue from mineral leasing and production due to Indian tribes and allottees, States and the U.S. Treasury.

The MMS strives to fulfill its responsibilities through the general guiding principles of: (1) being responsive to the public's concerns and interests by maintaining a dialogue with all potentially affected parties and (2) carrying out its programs with an emphasis on working to enhance the quality of life for all Americans by lending MMS assistance and expertise to economic development and environmental protection.